

AD-A267 806



2

MECHANISTIC MODELS OF SOOT FORMATION

Annual Report

for

June, 1992 to May, 1993

DTIC
ELECTE
AUG 12 1993
S C D

AFOSR-TR. 02 0502

Prepared by

M. B. Colket, III

R. J. Hall

and

M. D. Smooke

United Technologies Research Center

East Hartford, CT 06108

UTRC Report No. UTRC93-28

For

Air Force Office of Scientific Research
Bolling Air Force Base
Washington, D. C. 20332

Contract No. F49620-91-C-0056

J. M. Tishkoff

Program Manager

July 14, 1993

93-18858



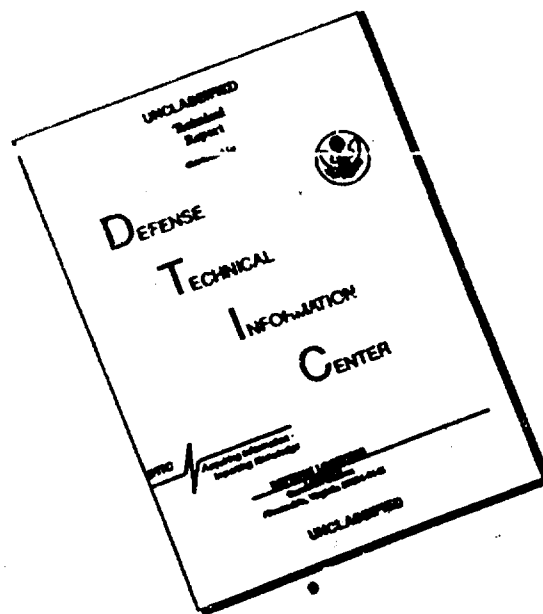
7412

DISTRIBUTION STATEMENT A

Approved for public release
Distribution Unlimited

93 8 11 016

DISCLAIMER NOTICE



**THIS DOCUMENT IS BEST
QUALITY AVAILABLE. THE COPY
FURNISHED TO DTIC CONTAINED
A SIGNIFICANT NUMBER OF
PAGES WHICH DO NOT
REPRODUCE LEGIBLY.**

UTRC 93-28

MECHANISTIC MODELS FOR SOOT FORMATION

Annual Report

Table of Contents

Accession For		
NTIS	CRA&I	<input checked="" type="checkbox"/>
DTIC	TAB	<input type="checkbox"/>
Unannounced		<input type="checkbox"/>
Justification		
By		
Distribution /		
Availability Codes		
Dist	Avail and/or Special	
A-1		

	<u>Page</u>
LIST OF FIGURES	ii
SUMMARY	1
I. INTRODUCTION	1
II. RESULTS	1
A. Pyrolysis of Phenylacetylene	1
B. Formation Mechanisms of Polyaromatic Hydrocarbons	2
C. Thermodynamics of Heavy Polyaromatic Hydrocarbons	2
D. Benzene Predictions in Methane/Air Diffusion Flames	5
E. Radiative Transfer in Sooting Opposed Jet Flames	10
F. Comparison of Soot Growth Models	10
G. Coupled Soot Growth/Opposed Jet Code	13
III. LIST OF PUBLICATIONS	16
IV. MEETING INTERACTIONS AND PRESENTATIONS	16
V. RECORD OF INVENTIONS	16
REFERENCES	17
Appendix A - The Formation of Benzene From Methane	A-1
Appendix B - Influence of Radiative Loss on Nitric Oxide Formation in Counterflow Diffusion Flames at High Pressure	B-1
Appendix C - Radiative Transfer in Sooting Counterflow Flames	C-1
Appendix D - The Radiative Source Term for Plane-Parallel Layers of Reacting Combustion Gases	D-1
Appendix E - Radiative Dissipation in Planar Gas-Soot Mixtures	E-1
Appendix F - Predictions of Soot Particle Growth Based on Aerosol Dynamics Modeling	F-1

DTIC QUALITY INSPECTED 3

List of Figures

<u>Figure Number</u>	<u>Title</u>	<u>Page</u>
Fig. 1	Phenanthrene/Anthracene Ratio	3
Fig. 2	Routes for PAH Formation	4
Fig. 3	ΔH_f /Carbon Atoms vs. Carbon Atoms	6
Fig. 4	Entropy/Carbon Atoms vs. Carbon Atoms	6
Fig. 5	Heat Capacity/Carbon Atoms vs. Carbon Atoms	7
Fig. 6	H/C Molar Ratio vs. Carbon Atoms	7
Fig. 7	Dependency of Equilibrium Temperature on PAH Thermodynamics	8
Fig. 8	Dependency of Equilibrium Hydrogen on PAH Thermodynamics	8
Fig. 9	Peak Benzene as Function of Strain	9
Fig. 10	Temperature vs. Strain Rate	9
Fig. 11	Comparison of Model and Experiment (Zhang, et. al)	11
Fig. 12	Radiative Loss vs. Soot Loading	12
Fig. 13	Soot Predictions for Premixed Ethylene Flame (c/o = 0.8)	14
Fig. 14	Soot Predictions of Premixed Ethylene Flame (c/o = 0.96)	14
Fig. 15	Soot Predictions for Premixed Propane Flame	15
Fig. 16	Soot Predictions for Premixed Acetylene Flame	15

MECHANISTIC MODELS FOR SOOT FORMATION

Annual Report

SUMMARY

The overall objectives of this work are to (1) refine and update an existing soot formation model and (2) incorporate this soot model into a code describing a laminar, opposed jet diffusion flame. To help advance the understanding of chemical limitations of PAH formation in the soot model, phenylacetylene has been pyrolyzed in a single-pulse shock tube. The formation of PAH's from aromatic-aromatic reactions has been observed and evidence has been obtained for isomerization (equilibration) among polyaromatic species. Thermodynamics of high molecular weight PAH's have been calculated. Benzene production and radiation phenomena have been modeled in an opposed jet diffusion flame and where possible these calculations have been compared to experimental results. A sectional aerosol model has been added to the diffusion flame code as well as related subroutines on soot formation, growth, and oxidation and the debugging of the code is nearly complete. Comparisons of the sectional model and a global soot formation model have been made for premixed flames.

I. INTRODUCTION

The overall goal of this three year effort is to incorporate a soot model into a code for a laminar, opposed jet, diffusion flame and make comparisons with experimental data. Specific objectives in order to reach this goal are: (1) identify reduced kinetic mechanisms which adequately describe ring formation and growth processes, (2) obtain and interpret new data on polyaromatic hydrocarbons (PAH) formed during hydrocarbon pyrolysis, (3) refine and update an existing soot formation model, (4) incorporate a radiation model into a code describing a laminar, opposed jet diffusion flame, and (5) incorporate the soot model into the flame code. In this second annual report, progress related to these items is briefly described.

II. RESULTS

II. A. Pyrolysis of Phenylacetylene

Phenylacetylene (0.25% in a bath of argon) has been pyrolyzed in a single-pulse shock tube as part of an effort to understand growth reactions, i.e., PAH formation, during the pyrolysis of hydrocarbons. Products have been analyzed using a gas chromatograph coupled to a mass selective detector. Light hydrocarbons are principally acetylene, diacetylene, and benzene.

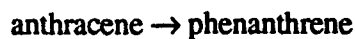
Several principal product species have a mass 178 amu and the most dominant of these has not yet been identified. The less dominant species with this mass are isomers of ethynylbiphenyl, phenanthrene, and methylenefluorene. Small concentrations of naphthalene, diethenylbenzene, naphthylacetylene, and acenaphthylene are also observed. Surprisingly, very low levels of anthracene (a three ringed aromatic of mass 178 amu) are observed at low temperatures. This result supports arguments for a facile route to formation of phenanthrene (a slightly more stable, three ringed aromatic) in the presence of phenylacetylene. The lack of substantial concentrations of pyrene and larger species

suggests very rapid reactions between these species and phenylacetylene, causing additional growth.

II. B. Formation Mechanisms of Polyaromatic Hydrocarbons

The preferential formation of phenanthrene during the pyrolysis of phenylacetylene was unusual. Alternatively, during the pyrolysis of toluene, anthracene production appears to be favored at low temperatures, yet fairly constant ratios of phenanthrene to anthracene were observed at elevated temperatures. In Fig. 1, the phenanthrene/anthracene ratio is plotted as a function of initial post-shock temperature for both the toluene and the phenylacetylene systems. For reference, ratios of the equilibrium concentrations of these species is also provided. This curve clearly shows the difference in the ability of the two single-ringed aromatic species to form three-ringed polyaromatics. Mechanisms for the facile formation of the polyaromatics are suggested in Fig. 2. In the case of phenylacetylene as a parent, it is assumed that the phenyl radical is formed from H-atom addition to the alkyl group, followed by acetylene elimination. Alternatively, phenanthrene could be formed by a Diels-Alder addition of phenylacetylene to benzene, followed by direct elimination of molecular hydrogen.

The relaxation of the phenanthrene to anthracene ratio to near equilibrium conditions at elevated temperatures strongly suggests the existence of rapid isomerization reactions. Included in Fig. 1 are calculations for the toluene case, where anthracene is assumed to be initially formed at a rate which is 42% faster than the phenanthrene production. The isomerization



is assumed to occur with a rate constant of $2 \times 10^{13} \exp(-75000 \text{ cal/mole/RT}) \text{ sec}^{-1}$. Using the reverse of this rate, the relaxation of phenanthrene to anthracene was also calculated for the phenylacetylene system. These results are also provided in the figure.

These different mechanisms (formation and isomerization steps) support a new hypothesis for PAH formation under pyrolytic conditions and in diffusion flames. It is already recognized that there is a difference between PAH/soot forming processes in a diffusion flame and in the post-flame zone of a premixed flame. Specifically, mechanisms are believed to be fuel-type independent in a premixed flame, but are fuel-dependent in diffusion flames. These new proposed mechanisms shed further light on this understanding. For diffusion flames, fuel type can have a major influence on ring formation mechanisms at early times and at temperatures below about 1600K. But for longer times and particularly at elevated temperatures, pyrolytic reactions, perhaps enhanced by oxidative pyrolysis, quickly convert the parent fuel into the more stable aromatic species, isomerizations occur and further ring growth is governed by similar mechanisms, independent of fuel type.

II. C. Thermodynamics of Heavy Polyaromatic Hydrocarbons

As part of the effort of incorporating a soot formation model into a flame code, the effects of changes in the thermodynamics of the average PAH moiety as PAH's increase in size is being evaluated. In addition, requirements for accurate estimates of the thermodynamics of these species is being determined. As an example of the types of calculations performed to date, heats of formation, entropies, and heat capacities per carbon atom are plotted as a

Fig. 1 Phenanthrene/Anthracene Ratio
Pyrolysis Data and Equilibrium

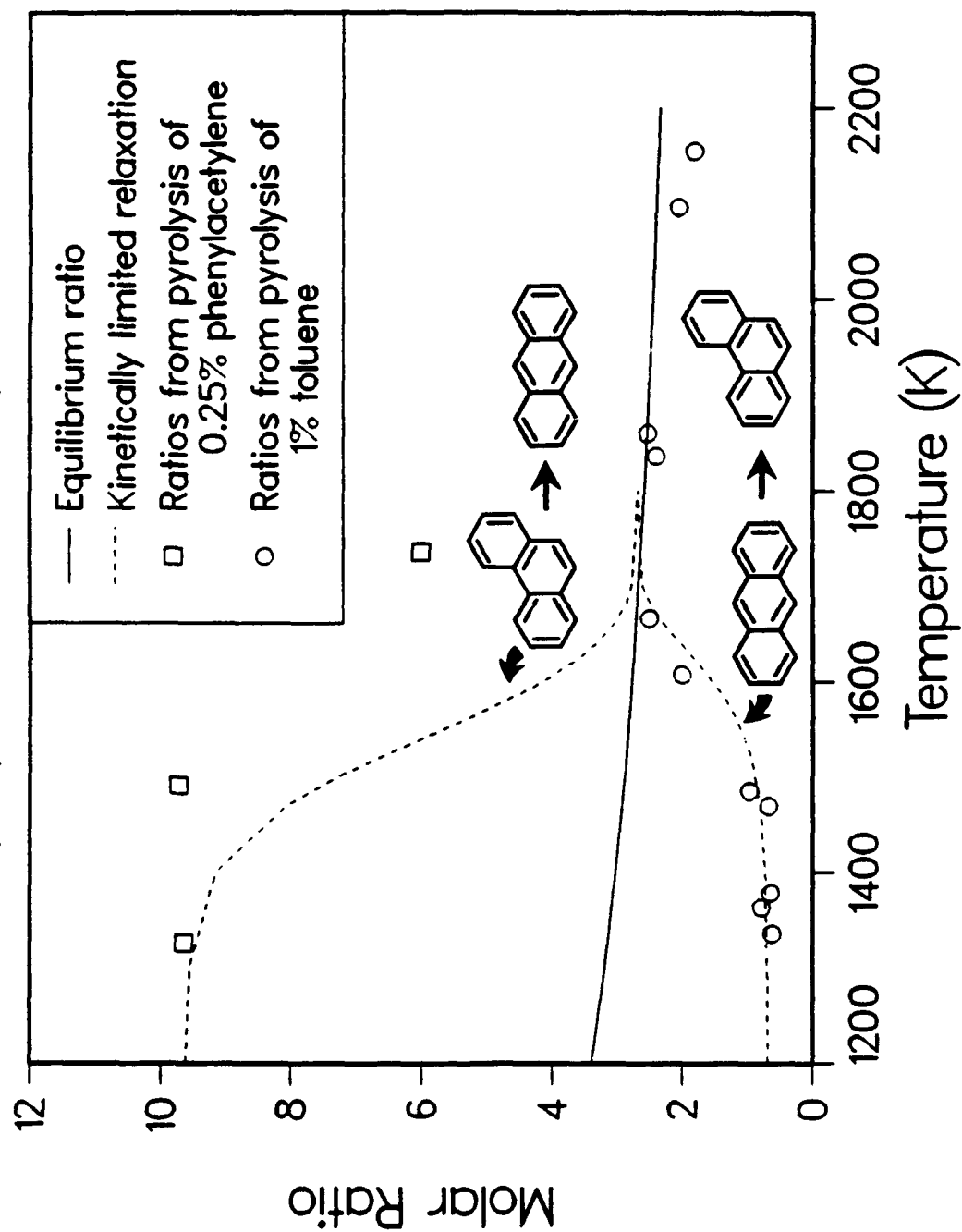
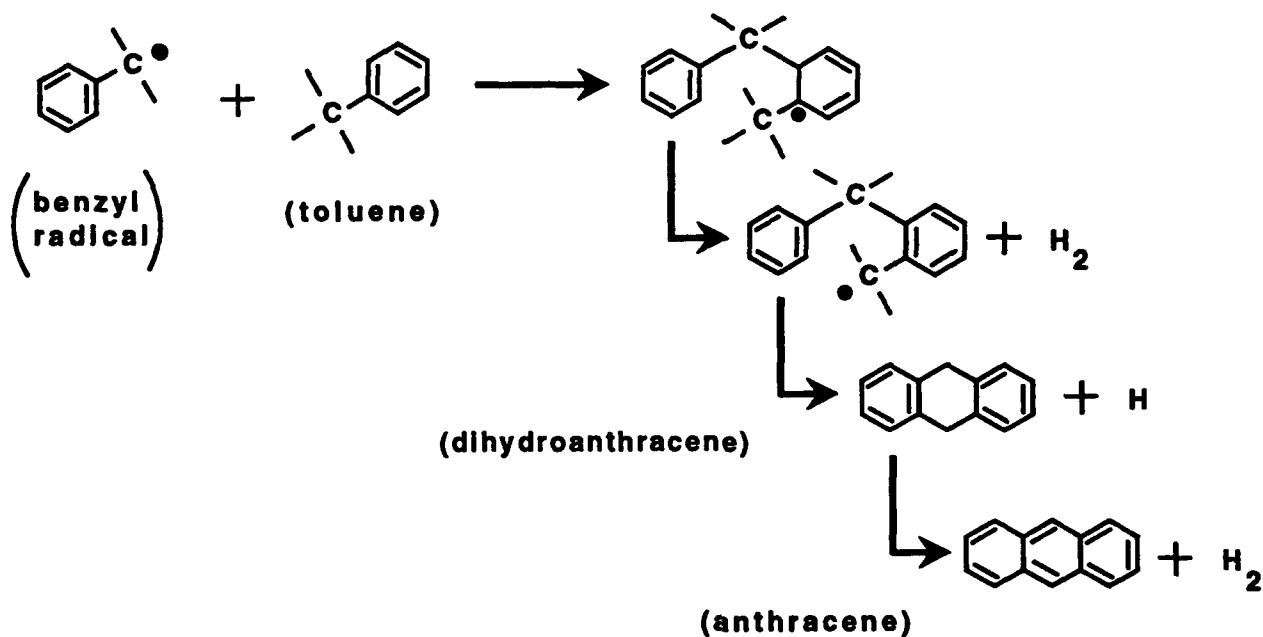
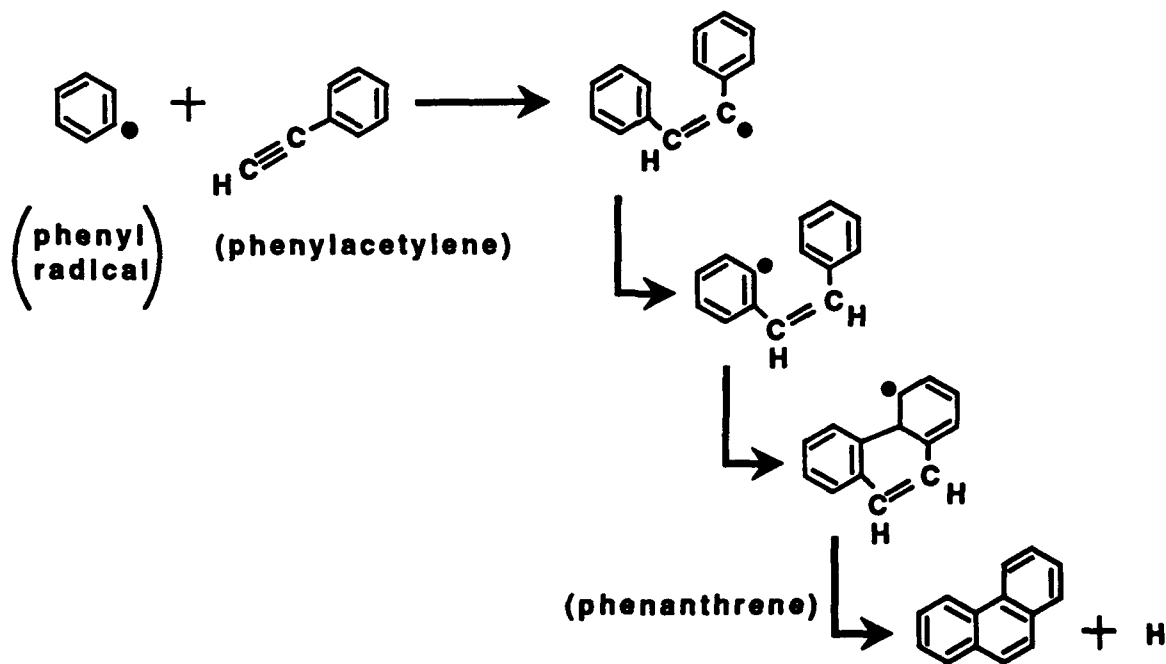


Fig. 2 Routes for PAH Formation

2a. Formation of anthracene from toluene



2b. Formation of phenanthrene from phenylacetylene



function of numbers of carbon atoms (C.A.) in Figs. 3-5. Species selected are composed of six ring aromatic structures, and the heaviest species are fully symmetric, six-sided polyaromatics. Calculations were performed for these planar species for PAH's containing as many as 864 carbon atoms and 72 hydrogen atoms. This species is composed of 397 aromatic rings and has a mass of 10,440 amu. The asymptotic values at 300K obtained from Figs. 3-5 can be compared with known values for graphitic carbon. The heats of formation of the PAH's appear to asymptote near a value of 1.7 kcal/mole per carbon atom, which is slightly greater than the heat of sublimation of a carbon atom, 1.45 kcal/mole/K. The limiting entropy is about 2 entropy units (e.u.), which is higher than the entropy of solid carbon, i.e., 1.4 e.u. Similarly, the limiting heat capacity is about 2.2 cal/mole/K per carbon atom, slightly higher than 2.05, the heat capacity of pure carbon. The differences between the calculated values and the values of graphitic carbon are presently being evaluated.

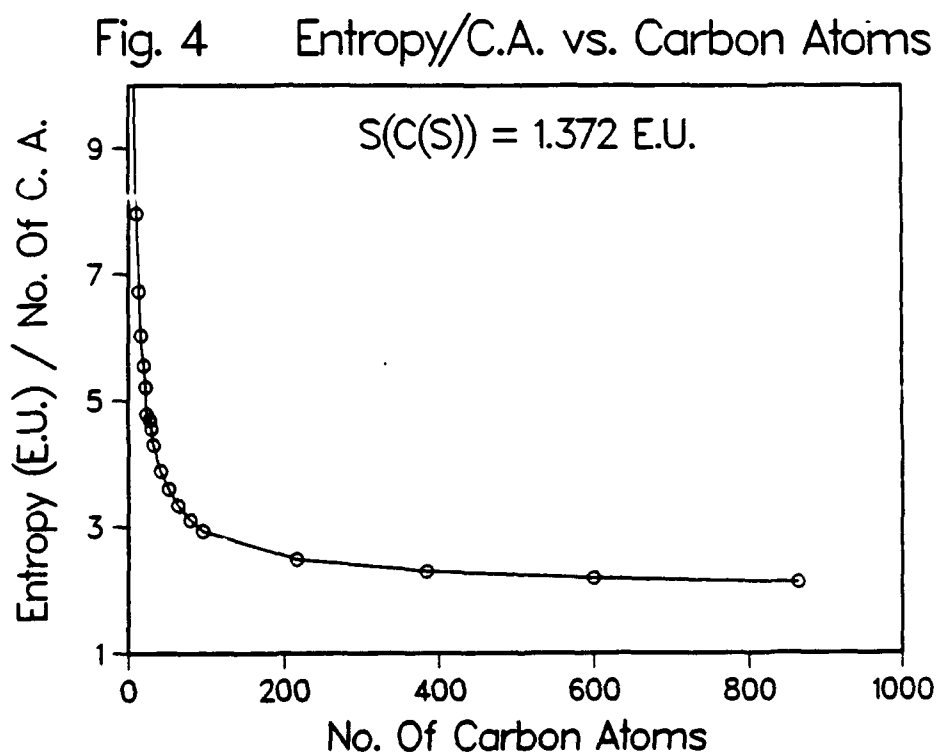
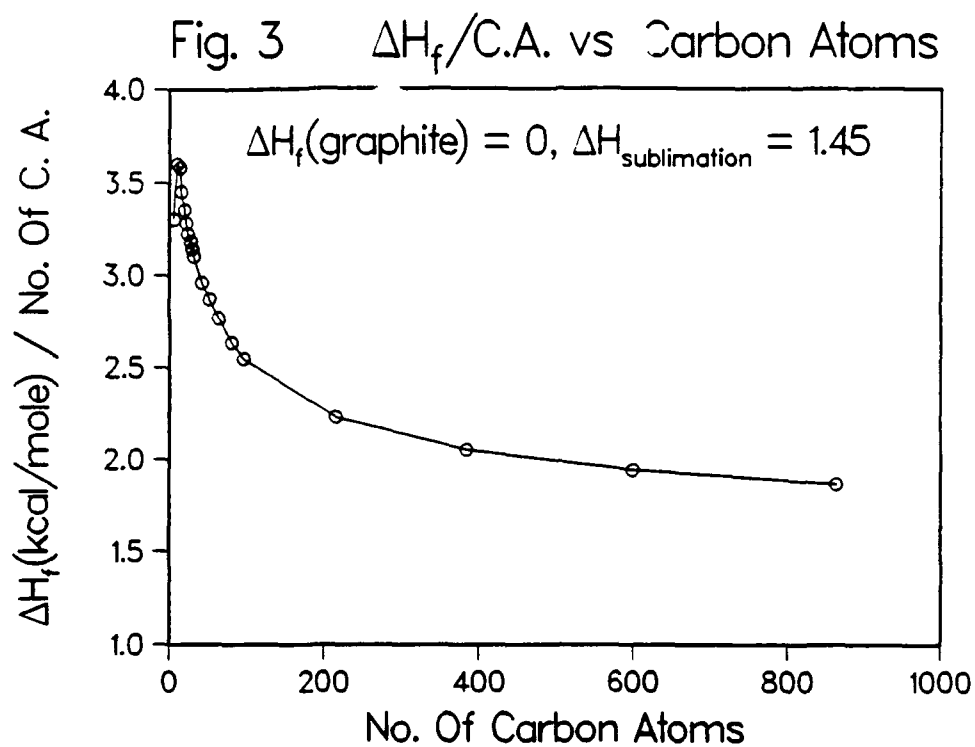
Typical soot particles have H/C molar ratios of about 1/8. In Fig. 6 are plotted H/C ratios of the polyaromatics examined above. Consequently, one might speculate that soot thermodynamics could be adequately represented by the thermodynamics of a species with the appropriate H/C ratio, i.e., $C_{384}H_{48}$.

Differing thermodynamics can have a substantial effect on the equilibrium situation between a fuel, molecular hydrogen and the polyaromatic product. For example, consider a 30% methane mixture in 70% nitrogen, initially at 1500K and 1 atmosphere. Equilibrium temperatures and hydrogen concentrations are plotted in Figs. 7 and 8 as a function of the polyaromatic assumed to be in equilibrium with the methane and hydrogen. As can be seen from these figures, temperatures can vary more than 150K and hydrogen concentrations can differ by nearly a factor of two for different assumed polyaromatics.

II. D. Benzene Predictions in Methane/Air Diffusion Flames

Last year it was shown that benzene formation during the oxidative pyrolysis of methane was due to reactions between C_3H_x species. Using this result a simplified benzene production model was constructed¹ together with several steps describing benzene pyrolysis and oxidation. This mechanism was added to a methane kinetics set (including C_2 -hydrocarbon chemistry) which has been used previously for modeling methane opposed jet flames. As described in Appendix A, benzene profiles were then predicted in an opposed jet diffusion flame. Peak benzene profiles are shown in Fig. 9 for flames with very low stretch through extinction. These profiles are plotted as a function of J , which is a parameter nearly proportional to strain rate. As shown in Fig. 9, as flame stretch increases, benzene production initially drops rapidly and then decreases more slowly with increasing stretch. Du, Axelbaum and Law² found that the sooting limit occurs in the region of rapid benzene decrease with flame stretch, and these results are therefore qualitatively consistent with linkage between benzene production and soot limits. The sooting limits as reported by Du, et. al, are reproduced in Fig. 9.

Temperatures at the location of peak benzene concentrations are plotted along with peak flame temperatures in Fig. 10 for flames of varying stretch. This figure indicates that benzene production in diffusion flames occurs at temperatures near 1400K, much lower than 1800K at which benzene was formed in the shock tube experiments on rich methane oxidation. Since dominant kinetic pathways can be altered by a substantial shift in temperature, the full kinetics set (all known mechanisms of benzene formation included) were used to recalculate selected diffusion flames. Under all conditions only trivial changes were observed in the benzene profile, confirming the earlier result of the importance of propargyl species to benzene production in methane systems.



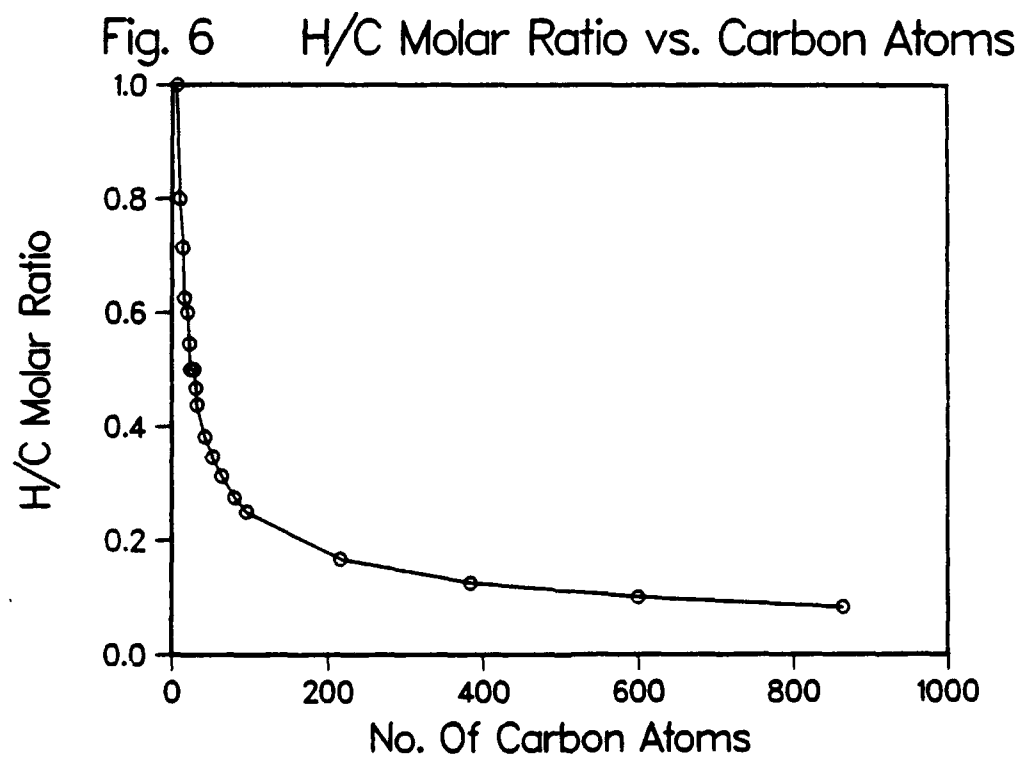
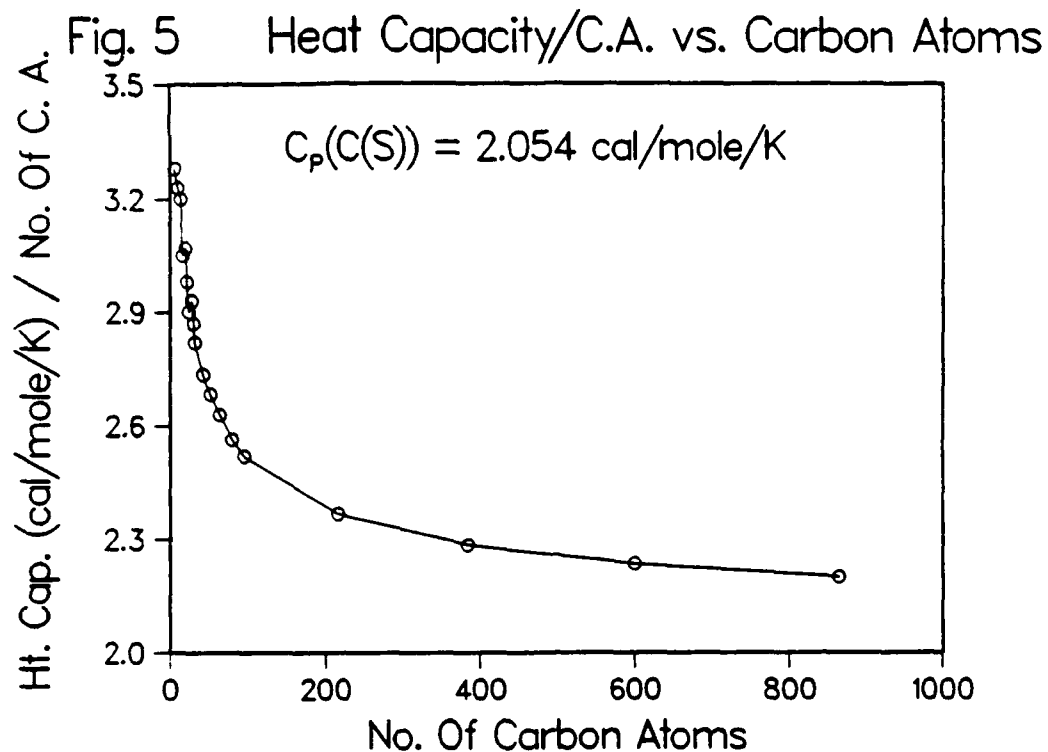


Fig. 7 Dependency Of Equilibrium Temperatures
On PAH Thermodynamics

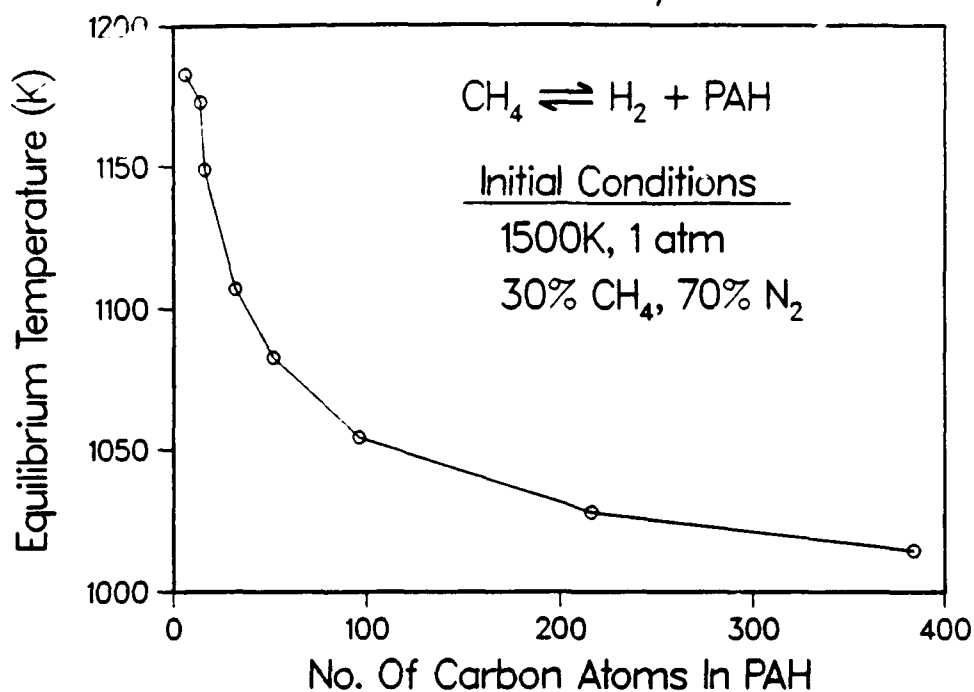


Fig. 8 Dependency of Equilibrium Hydrogen
On PAH Thermodynamics

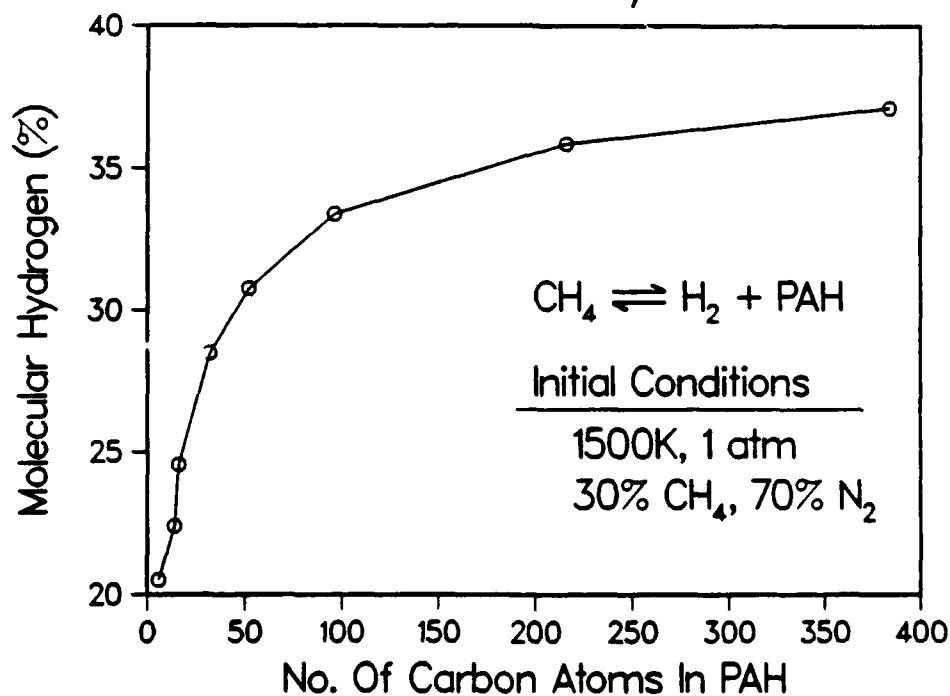


Fig. 9 Peak Benzene As Function Of Strain
Laminar Opposed Jet Diffusion Flame

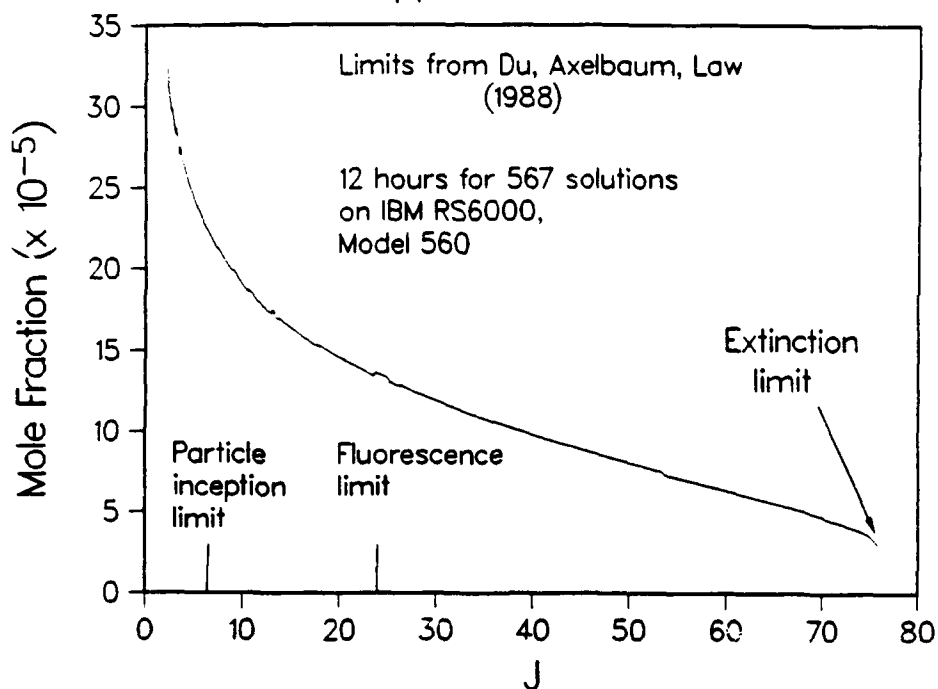
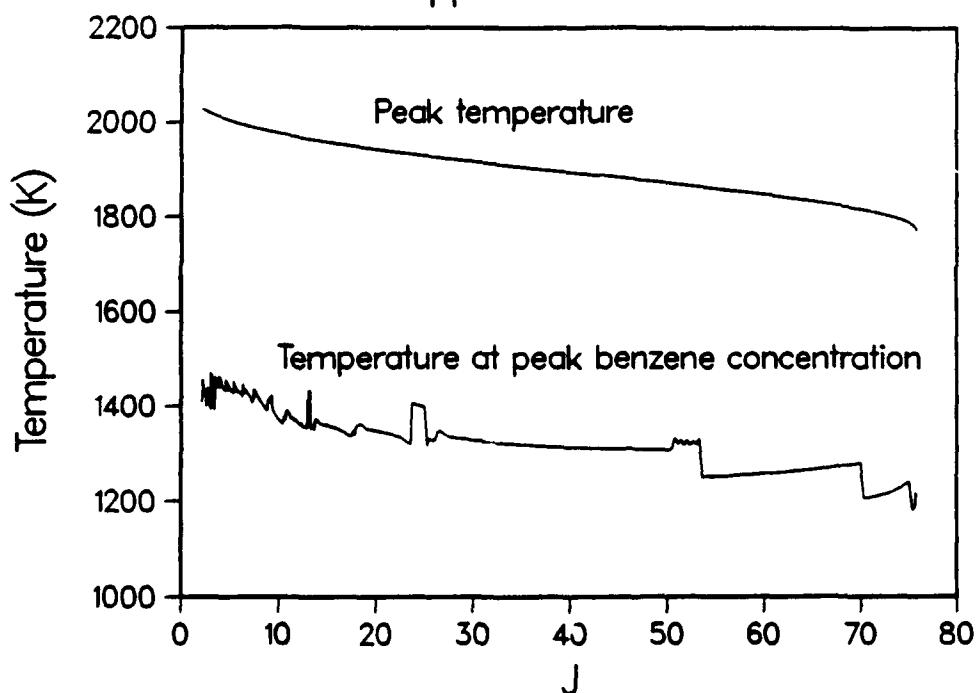


Fig. 10 Temperature vs. Strain Rate
Laminar Opposed Jet Diffusion Flame



In addition, an attempt was made to model a nitrogen diluted methane studied by Zhang, Atreya and Lee³. All major species were predicted well. As shown in Fig. 11, shapes of C₂-species were described well, but typically peak concentrations were modeled only within a factor of two to three, perhaps due to the use of only a skeleton C₂-hydrocarbon mechanism. Benzene profiles were predicted very well (shape and peak concentration) although this result may be somewhat fortuitous due to the inadequacy in the comparison of the C₂-species.

In general, these kinetic results are very encouraging for the soot modeling effort in that opposed jet diffusion flames can be modeled fairly inexpensively with chemistry describing species as large as benzene. For example, in order to determine benzene concentrations, etc., as a function of strain rate, 567 flames were calculated in 12 hours using an IBM RS6000 workstation.

II. E. Radiative Transfer in Sooting Opposed Jet Flames

Our previous investigations of radiative transfer in non-sooting opposed jet flames showed that, for realistic values of strain rate, up to 5% of the flame enthalpy release could be converted to thermal radiation. The accompanying reduction in peak flame temperatures gave rise to substantial reductions of about 33% in the peak NO concentrations⁴. At very low strain rates and high pressures, where the pressure-flame width product can be one atm-cm or more, it was shown that optical thickness effects can become important and an expression was derived for self-absorption⁵. Radiative loss effects can be particularly large in sooting flames. To assess the effect in sooting opposed jet flames, the gas band expressions for the net cooling rate have been extended to include soot. The problem has traditionally been a difficult one because of the overlaps between the broadband soot absorption profile and the molecular resonances. Net gas cooling results from radiative emission minus self-absorption. The self-absorption term has been derived from a solution for the radiative intensity by taking hemispherical and wavelength averages. The result is a semi-analytical expression for the net cooling rate in which the emission is offset by soot and gas self-absorption, and by soot-gas radiative interchange⁶. Figure 12 shows the calculated radiative loss in a model sooting diffusion flame in which a band of soot has been synthetically inserted between the flame and the stagnation plane, and the peak soot volume fraction varied parametrically. The flame is at 10.5 atmospheres and the strain rate is 20 sec⁻¹; the fuel and oxidizer temperatures have been chosen to give a peak flame temperature approximating that of jet fuel⁴. The assumed location of the sooting region is such as to produce an effective radiation temperature for the soot of about 1500K, about 900K cooler than the peak flame temperature. Gas band self-absorption is important at this combination of pressure and strain rate. For peak soot volume fractions in excess of roughly 10⁻⁵, soot radiative transfer begins to dominate, and predicted radiative loss fractions rise to the level of 20%. At the highest volume fractions, the reduction in temperature in the sooting region is large enough to raise the possibility of strong interactions between soot growth and soot radiation. These effects are, however, strongly sensitive to the presumed location and radiative temperature of the soot. A self-consistent analysis will be provided by the coupled soot growth-opposed jet flow code whose development is described in Section II.G.

II. F. Comparison of Soot Growth Models

The soot growth model developed under this program combines a simplified picture of particle inception linked to local benzene production rates and an aerosol dynamics-based treatment of particle growth using the algorithms of the well-known MAEROS code⁷.

Fig. 11 Comparison of Model and Experiment
(Zhang, et al, 1993)

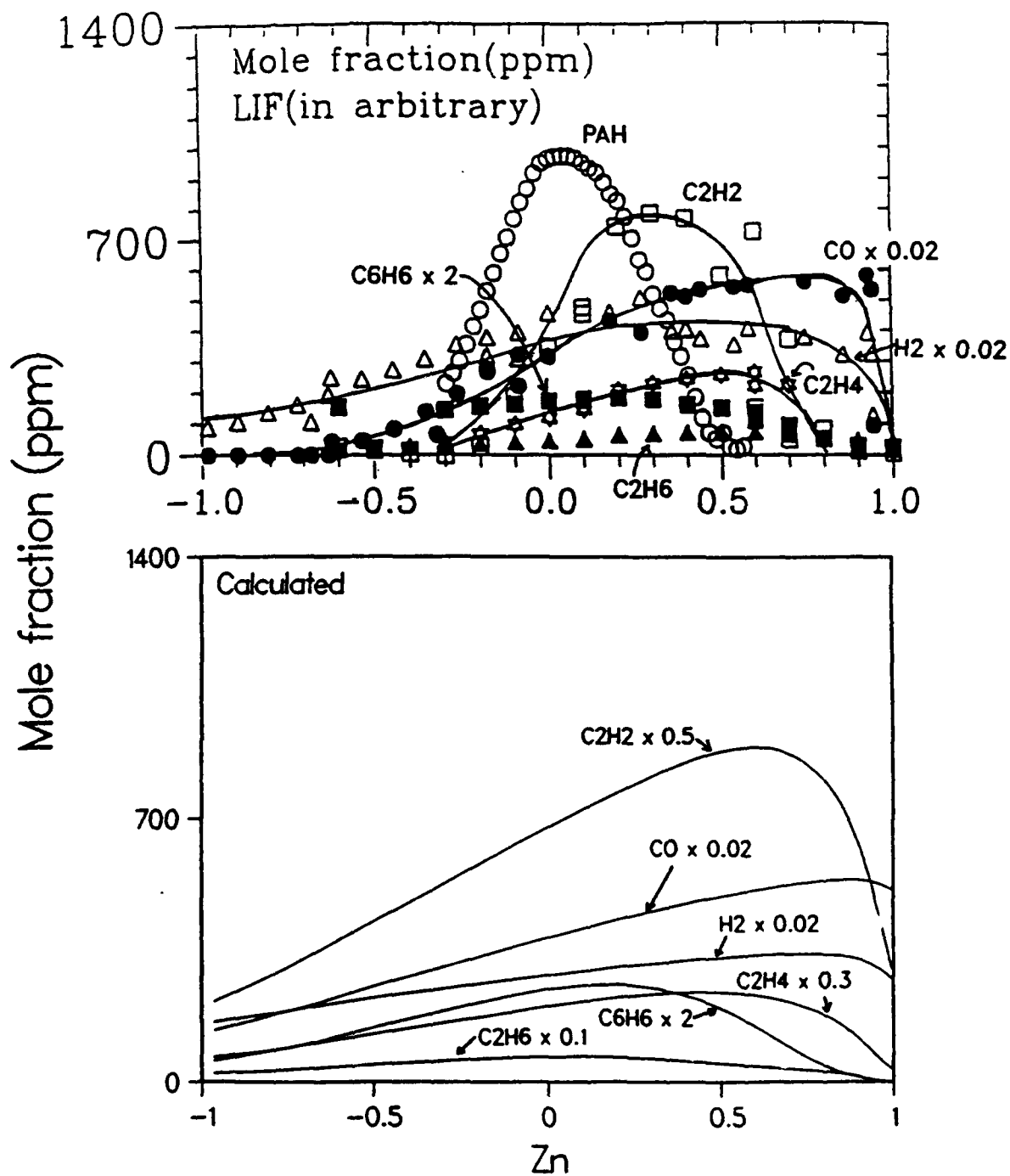
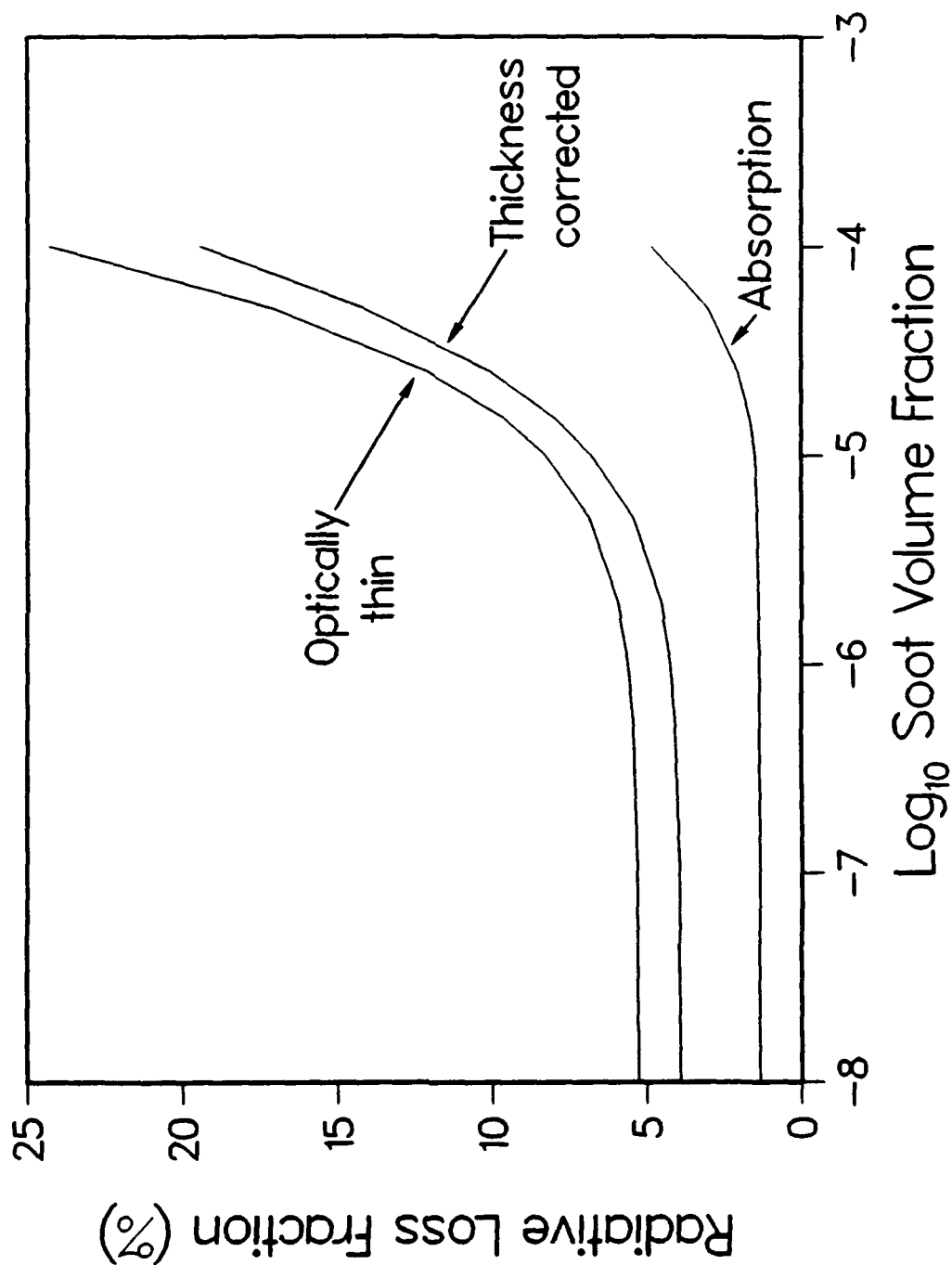


Fig. 12 Radiative Loss vs. Soot Loading
 10.5 atm; $T_{\text{rad}}(\text{soot}) = 1500 \text{ K}$; $a = 20.5 \text{ sec}^{-1}$



This approach necessitates solving a dynamical equation for each particle size class or section. Other investigators have proposed simpler, global models based on assuming a monodisperse size distribution with two dynamical equations, one for the particle number density, and the other for the volume fraction. One such model is that due to Lindstedt⁸, which features an inception rate proportional to the acetylene concentration, and a surface growth rate proportional to the square root of surface area. It has given good agreement with sooting opposed jet data, and has been incorporated into laminar flamelet/p.d.f. models for turbulent jets⁸. Test comparisons of this model and the sectional model have been made for the premixed flame data⁹⁻¹⁰. The first comparison, shown in Fig. 13, is for the atmospheric pressure, ethylene flame⁹, where the peak temperature is about 1650K and the C/O ratio is 0.8. The analogous comparison for C/O = 0.96 is shown in Fig. 14. While the overall agreement of the sectional model is slightly better, the agreement of the Lindstedt model is satisfactory considering its simplicity. For the higher temperature propane and acetylene flames¹⁰, however, where peak temperatures are about 1850K and 2050K, respectively, the simplified model fails, as shown in Figs. 15 and 16. All the sectional model calculations were made with the "modified Frenklach-Wang" surface growth mechanism¹¹; it incorporates high temperature active site decay and acetylene desorption mechanisms that make possible the better agreement shown. There is no reason to expect better performance from other global models in the literature, and it is probably the case that their usefulness is limited to restricted parameter ranges where they have been fitted to opposed jet data, for example. In these premixed flames, the global model has considerable sensitivity to inception rate, as has been found for the sectional model¹¹.

II. G. Coupling of Soot Growth Model and Opposed Jet Flow Code

The soot growth equations have been programmed in a seamless fashion into an opposed jet flow solver, and the combined program is being debugged. The dynamical equations for the particulate concentrations include nucleation coupled to the benzene production rate, particle coalescence, surface growth, and oxidation. This work marks the first time that the particle sectional growth equations widely used in aerosol science have been coupled to the conservation equations for a diffusion flame. Particle diffusion and thermophoresis velocities in the free molecule regime have been included. The first set of calculations has been based on a perturbation approximation in which particle thermochemistry and depletion of gas phase species like acetylene by surface growth are assumed to be small. The next stage will include these effects, as well as radiative loss. Preliminary indications are that the addition of the particle sectional equations does not complicate the convergence behavior of the Newton-Raphson solution scheme. When debugging is completed, comparisons with opposed jet data will be made.

Fig. 13 Soot Predictions for Premixed Ethylene Flame ($C/O = 0.8$)

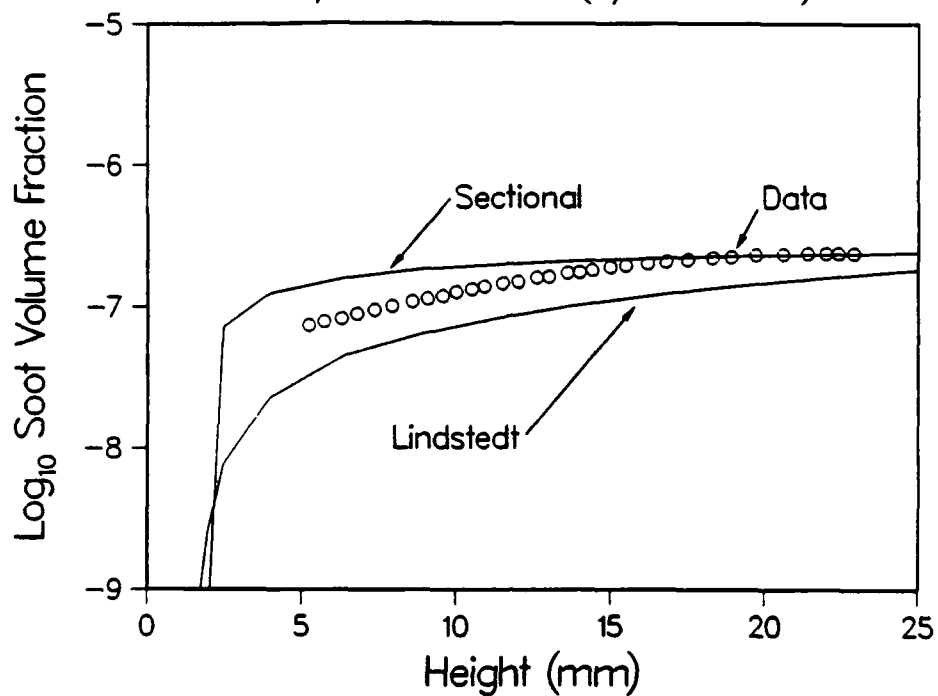


Fig. 14 Soot Predictions for Premixed Ethylene Flame ($C/O = 0.96$)

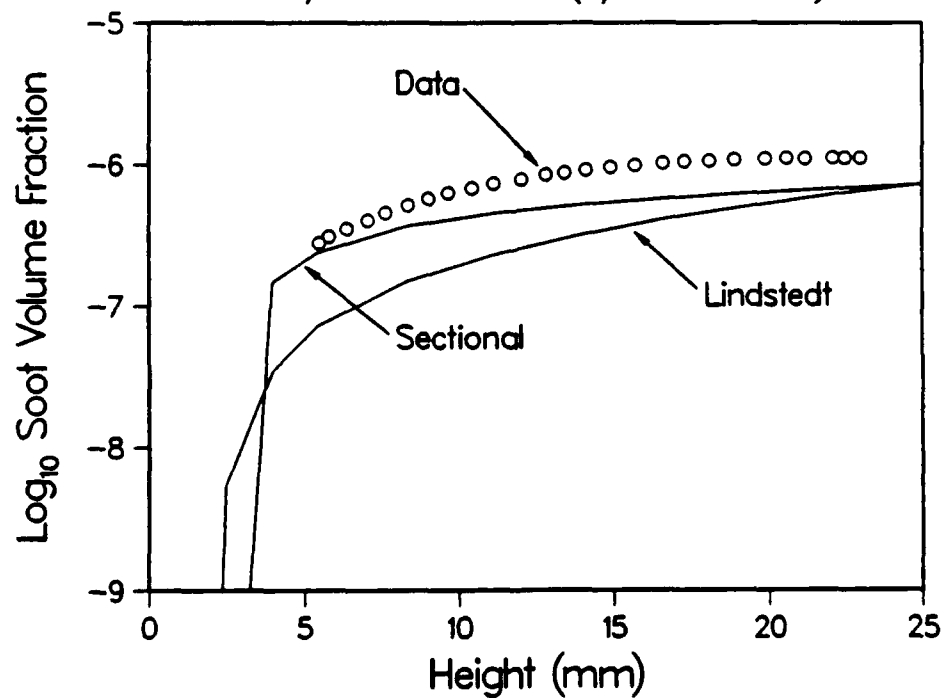


Fig. 15 Soot Predictions for Premixed Propane Flame

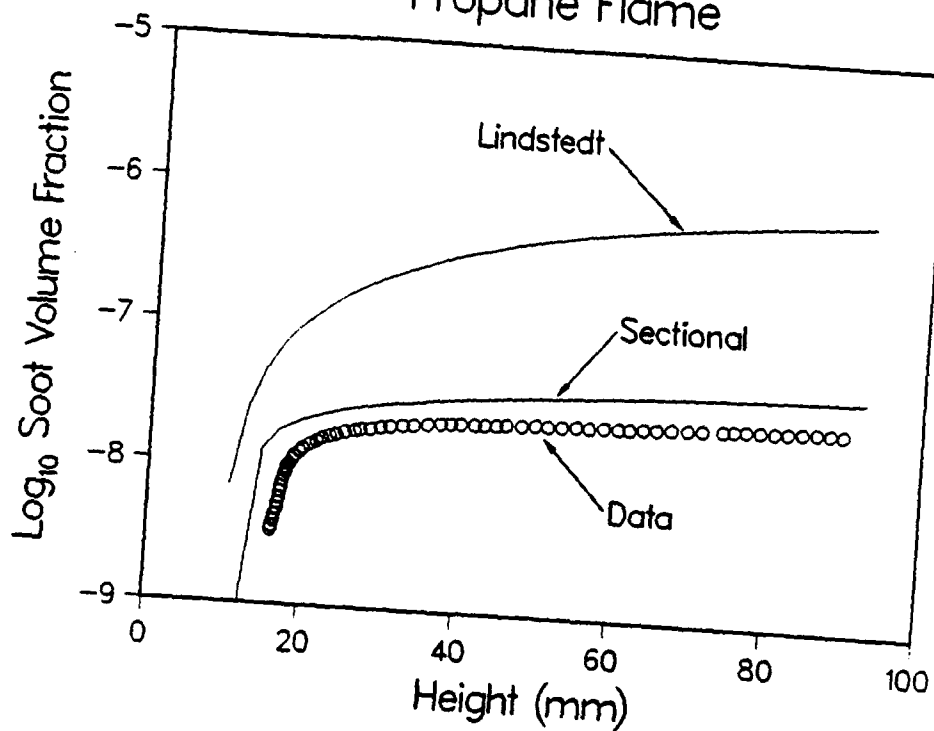
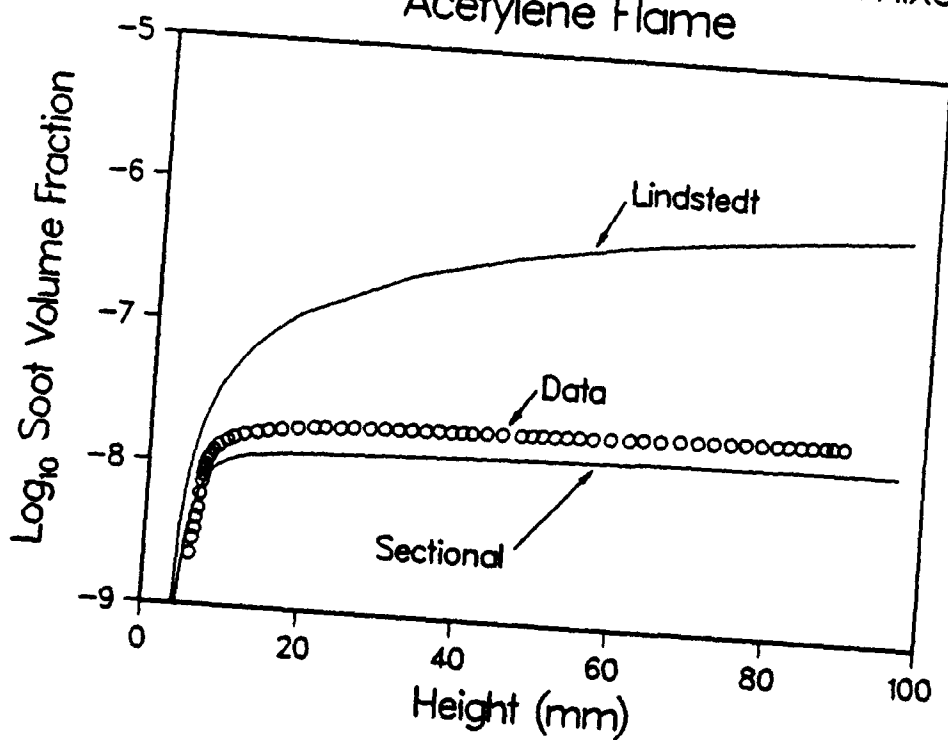


Fig. 16 Soot Predictions for Premixed Acetylene Flame



III. LIST OF PUBLICATIONS

A paper entitled "Influence of Radiative Loss on Nitric Oxide Formation in Counterflow Diffusion Flames at High Pressure", by A. Vranos and Robert J. Hall, has been published in Combustion and Flame. A copy of this document, which was partially supported under this contract, is provided in Appendix B.

A paper entitled "The Radiative Source Term for Plane-Parallel Layers of Reacting Combustion Gases", by Robert J. Hall, has been published in the Journal of Quantitative Spectroscopy and Radiative Transfer. A copy of this document is provided in Appendix D.

A manuscript entitled "Radiative Dissipation in Gas-Soot Mixtures", by Robert J. Hall, has been submitted to the Journal of Quantitative Spectroscopy and Radiative Transfer. A copy of this document is provided in Appendix E.

A manuscript entitled "The Formation of Benzene From Methane in Shock Tubes and Diffusion Flames" by M. B. Colket and M. D. Smooke is in preparation.

A review article describing state-of-the-art modeling of soot formation processes is being prepared. It is co-authored by I. Kennedy and M. Colket.

IV. MEETING INTERACTIONS AND PRESENTATIONS

A paper entitled "Predictions of Soot Particle Growth Based on Aerosol Dynamics Simulations", by Robert J. Hall and Meredith B. Colket, was presented at the European Aerosol Conference, September 7-11, 1992, in Oxford, U. K. The extended abstracts were published in a special issue of the Journal of Aerosol Science, and this is presented in Appendix F.

Robert J. Hall presented a paper entitled "Radiative Transfer in Sooting Counterflow Flames" at the Central and Eastern States Combustion Institute Joint Technical Meeting, March 15-17, 1993, in New Orleans, LA. A copy of the extended abstract is provided in Appendix C.

A paper entitled "The Formation of Benzene From Methane" by M. B. Colket and M. D. Smooke was presented to the Joint Technical Meeting of the Central States and Eastern States Section of the Combustion Institute, March 15-17, 1993 in New Orleans. A copy of the extended abstract is provided in Appendix A.

Robert J. Hall made a presentation to NASA Lewis personnel on March 25, 1993 that included a description of the coupled soot growth/opposed jet code being developed under this contract. In a program that will be funded by NASA, the code will be used to generate sooting flamelet libraries for a laminar flamelet/mixture fraction pdf approach to turbulent radiation in the rich zone of the RBQQ combustor, under development in the high speed research program.

On June 2-4, 1993, M. Colket attended the 15th Combustion Research Conference held at Lake Harmony, Pennsylvania. M. Colket was invited to this DOE, Basic Energy Sciences Contractor's Meeting to be an observer and participant.

V. RECORD OF INVENTIONS

There were no inventions during this period.

REFERENCES

1. M. B. Colket and M. D. Smooke, "The Formation of Benzene from Methane", Presented to the Joint Technical Meeting of The Central and Eastern States Sections of the Combustion Institute, New Orleans, March 15-17, 1993.
2. D. X. Du, R. L. Axelbaum, and C. K. Law, Twenty-Second Symposium (International) on Combustion, The Combustion Institute, p. 387, 1988.
3. C. Zhang, A. Atreya, and K. Lee, Twenty-Fourth Symposium (International) on Combustion, The Combustion Institute, p. 1049, 1992.
4. A. Vranos and R.J. Hall, "Influence of Radiative Loss on Nitric Oxide Formation in Counterflow Diffusion Flames at High Pressure", *Combustion and Flame*, **93**, pp. 230-238, May, 1993. Also see R. J. Hall, "Radiative Transfer in Sooting Counterflow Flames", Presented to the Joint Technical Meeting of the Central and Eastern States Sections of the Combustion Institute, New Orleans, March 15-17, 1993.
5. R. J. Hall, "The Radiative Source Term for Plane-Parallel Layers of Reacting Combustion Gases", *JQSRT*, **49**, pp. 517-523, May, 1993.
6. R. J. Hall, "Radiative Dissipation in Planar Gas-Soot Mixtures", submitted to *JQSRT*, 1993.
7. R. J. Hall and M. B. Colket, "Predictions of Soot Particle Growth Based on Aerosol Dynamics Modeling", *J. Aerosol Sci.*, **23**, S129-S132, 1992.
8. M. Fairweather, W. P. Jones, and R. P. Lindstedt, *Comb. Flame*, **89**, 45 (1992).
9. S. J. Harris and A. M. Weiner, *CST*, **131**, 155, (1983).
10. H. Bockhorn, F. Fetting, and H. W. Wenz, *Ber. Bunsenges. Phys. Chem.*, **87**, 1067 (1983).
11. M. B. Colket, et. al, "The Determination of Rate-Limiting Steps During Soot Formation", Final Report for AFOSR Contract No. F49620-88-C-0051 for period February, 1988 to January, 1991.

Appendix A

The Formation of Benzene From Methane

The Formation of Benzene From Methane

by M. B. Colket
United Technologies Research Center
East Hartford, CT 06108

and

M. D. Smooke
Department of Mechanical Engineering
Yale University
New Haven, CT 06520

Presentation to the Joint Technical Meeting of the
Eastern States and Central States Sections of the Combustion Institute
March 15-17, 1993, New Orleans, LA

As part of an objective to model soot production in laminar diffusion flames, we have been analyzing the mechanisms for the formation of benzene during the oxidative pyrolysis of methane. This presentation describes some experimental work on the fuel-rich oxidation of methane in a single-pulse shock tube, detailed chemical kinetic modeling studies comparing the various routes to the formation of benzene, development of a simplified model of benzene formation and destruction and finally model prediction of benzene in opposed-jet laminar diffusion flames.

A single-pulse shock tube was used to oxidatively pyrolyze methane over the temperature range of 1200 to 2200K, total pressures of 10-12 atmospheres, equivalence ratios of 8 to 16 and initial methane levels of 0.6 to 4% in argon. Dwell times were approximately 500-600 microseconds. Gas samples were collected and analyzed using capillary gas chromatography for the hydrocarbons, hydrocarbon oxygenates, carbon oxides, oxygen, and hydrogen.

A chemical kinetic mechanism for fuel-rich methane oxidation was developed based on the acetylene pyrolysis mechanism with added reactions for methane pyrolysis and oxidation and including reactions involving C₅-hydrocarbons as well as six separate steps for the formation of benzene (or phenyl). These reactions are:

Reactions	A (cc/mole/sec)	F (kcal/mole)
$n\text{-C}_4\text{H}_5 + \text{C}_2\text{H}_2 \rightarrow \text{C}_6\text{H}_6 + \text{H}$	4.5×10^{12}	10.0
$\text{C}_2\text{H}_3 + \text{C}_4\text{H}_4 \rightarrow \text{C}_6\text{H}_6 + \text{H}$	4.0×10^{11}	0.0
$\text{C}_2\text{H}_2 + n\text{-C}_4\text{H}_3 \rightarrow \text{l-phenyl} + \text{H}$	5.2×10^{11}	0.0
$\text{C}_3\text{H}_3 + \text{C}_3\text{H}_3 \rightarrow \text{phenyl} + \text{H}$	5.0×10^{12}	0.0
$\text{CH}_3 + c\text{-C}_5\text{H}_5 \rightarrow \text{C}_6\text{H}_6 + 2\text{H}$	5.0×10^{12}	0.0
$\text{C}_2\text{H}_2 + c\text{-C}_5\text{H}_5 \rightarrow \text{C}_7\text{H}_7$	3.0×10^{11}	15.0

The last step, which forms the benzyl radical, could lead to the formation of toluene and hence benzene following substitution of the methyl radical. Evidence for the existence of the last two steps comes from recent pyrolysis studies on cyclopentadiene pyrolysis. The reader should be aware that despite the conclusion of the propargyl radical recombination step in this study, recent results by Kiefer (1992) place this particular step in question and instead support the overall process of propargyl addition to allene to explain the observed facile formation of benzene.

A comparison of some of the experimental data with predictions from the detailed chemical model (including effects of the quenching wave) are shown in Fig. 1. The comparisons aren't perfect, but at least are reasonable. A detailed reaction path analysis demonstrated that at 1800K near the peak in the benzene concentration, the dominant path for the formation of aromatics was propargyl recombination. The net rates of reactions for each of six aromatic-forming reactions is shown in Fig. 2. The figure shows the complexity in this reaction system. At 1800K, although C_3H_3 recombination is dominant, it is also clear that decomposition of phenyl (eventually) into acetylene and $n-C_4H_3$ is an important removal process. Presumably, at slightly lower temperatures and perhaps with different dominant reactive species, net formation of phenyl results from this reaction. Also of interest from Fig. 2 is the apparent relative importance of methyl radical addition to cyclopentadienyl radicals. Obviously the proposed reaction is not elementary and probably requires a reaction barrier. The suggested rate constant is consistent with an activation of only 5 kcal/mole. Consequently, this reaction can be considered speculative.

Assuming that propargyl recombination is in fact the dominant ring-forming reaction for the shock tube studies and further assuming that this conclusion can be extended to diffusion flame conditions (See subsequent paragraph for further discussion), then a simplified kinetic mechanism was constructed. This mechanism was selected to mate with an existing C₁ and C₂ mechanism for methane combustion already in use for diffusion flame modeling. This reduced set was selected to minimize additional reactions and species. This eighteen reaction set includes eight new species not present in the C₁-, C₂ reaction set, as seen in Table I. Using this reaction set, benzene profiles have been predicted in an opposed jet diffusion flame. Concentrations of a variety of species are shown in Fig. 3 for a flame with mild stretch. Peak benzene profiles are shown in Fig. 4 for a range of flame stretch conditions. As the strain rate begins to increase, benzene concentrations rapidly decrease, then there is a more gradual decrease in the peak benzene concentration at higher strain rates. Qualitatively, this result is consistent with the observations of Du, Axelbaum and Law, who found the soot extinction limit to be about a factor of ten less than that at extinction and the fluorescence limit to be only a factor of two and one-half below the extinction limit.

As stated earlier, the above predictions are based upon the premise that propargyl recombination is the dominant ring-formation mechanism. The modeling results indicate that benzene concentration peaks at temperatures near 1400K, significantly lower than the temperatures of the shock tube experiments where peak benzene concentrations were observed. The temperature difference and the possible 'dwell time' difference could lead to a difference in the dominant reaction pathway. Consequently, the conclusions reached in this analysis should be considered preliminary.

References

J. Kiefer, personal communication, 1992.

D. X. Du, R. L. Axelbaum, and C. K. Law, Twenty-Second Symposium (Int'l) on Combustion, The Combustion Institute, p. 387, 1988.

Acknowledgements

This work has been supported in part by the Air Force Office of Scientific Research under Contract No. F49620-91-C-0056.

TABLE I
Preliminary Sub-Mechanism for Formation and Destruction of Benzene
($k_{\text{forward}} = A \exp(-E/RT)$)

Reactions Considered	$\log_{10} A$ (cc-mole-sec)	E (kcal/mole)
1. $C_3H_4 + H \leftrightarrow C_2H_2 + CH_3$	13.60	2.4
2. $C_3H_4 + H \leftrightarrow C_3H_3 + H_2$	12.00	1.5
3. $CH_3 + C_3H_4 \leftrightarrow C_3H_3 + CH_4$	12.30	7.7
4. $C_3H_3 + C_3H_3 \leftrightarrow C_6H_5 + H$	12.70	0.0
5. $C_6H_6 + H \leftrightarrow C_6H_5 + H_2$	14.40	16.
6. $C_6H_6 \leftrightarrow C_6H_5 + H$	16.70	107.9
7. $C_6H_5 + CH_4 \leftrightarrow C_6H_6 + CH_3$	12.47	5.0
8. $C_6H_5 \leftrightarrow l\text{-}C_6H_5$	13.54	65.
9. $l\text{-}C_6H_5 \rightarrow 2C_2H_2 + C_2H$	14.00	36.
10. $C_6H_5 + O_2 \leftrightarrow c\text{-}C_5H_5 + CO + O$	12.32	7.5
11. $c\text{-}C_5H_6 \leftrightarrow H + c\text{-}C_5H_5$	15.30	81.
12. $H + c\text{-}C_5H_6 \leftrightarrow H_2 + c\text{-}C_5H_5$	12.47	8.0
13. $H + c\text{-}C_6H_6 \leftrightarrow C_2H_4 + C_3H_3$	12.70	18.
14. $CH_3 + c\text{-}C_5H_6 \leftrightarrow CH_4 + c\text{-}C_5H_5$	12.70	5.0
15. $c\text{-}C_5H_5 \leftrightarrow C_2H_2 + C_3H_3$	14.00	74.
16. $C_6H_6 + OH \leftrightarrow C_6H_5 + H_2O$	13.33	4.6
17. $C_6H_6 + O \leftrightarrow c\text{-}C_5H_5 + CO + H$	13.44	4.9
18. $c\text{-}C_5H_5 + O \leftrightarrow C_2H_3 + C_2H_2 + CO$	13.70	0
19. $C_6H_5 + OH \leftrightarrow c\text{-}C_5H_5 + CO + H$	13.00	0

FIG. 1 SPST METHANE OXIDATION ($\phi=8$)

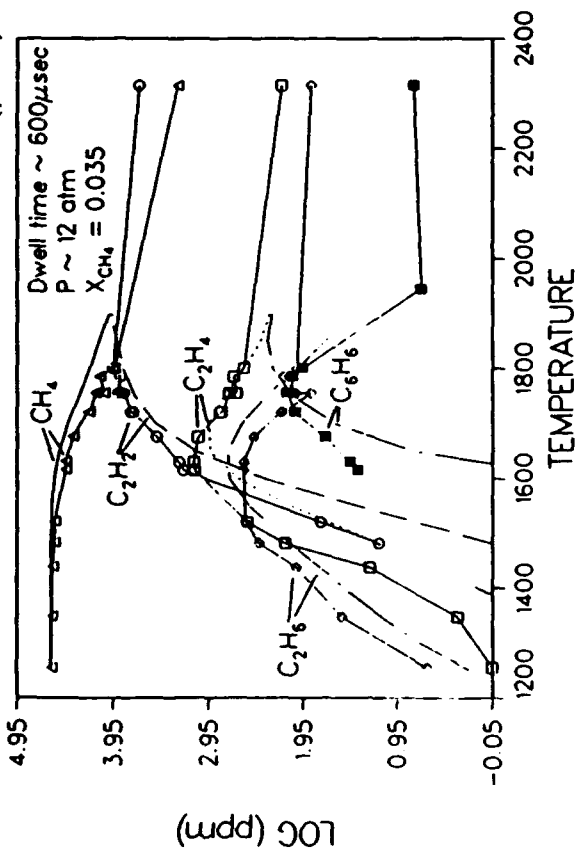


FIG. 3 CALCULATED SPECIES PROFILES IN AN OPPOSED-JET, METHANE-AIR FLAME

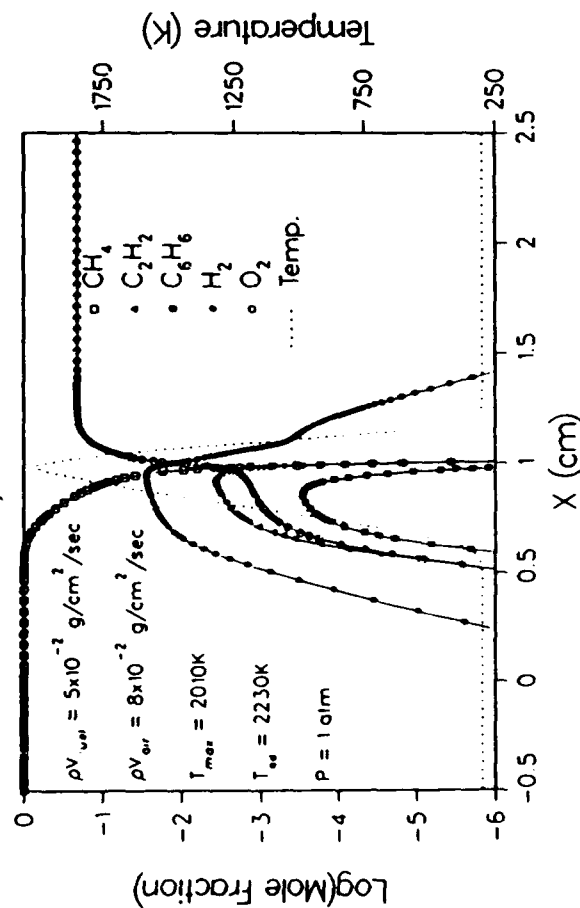


FIG. 2 NET RATES OF RING-FORMING REACTIONS 4.0% METHANE, 1.0% OXYGEN at 1800K

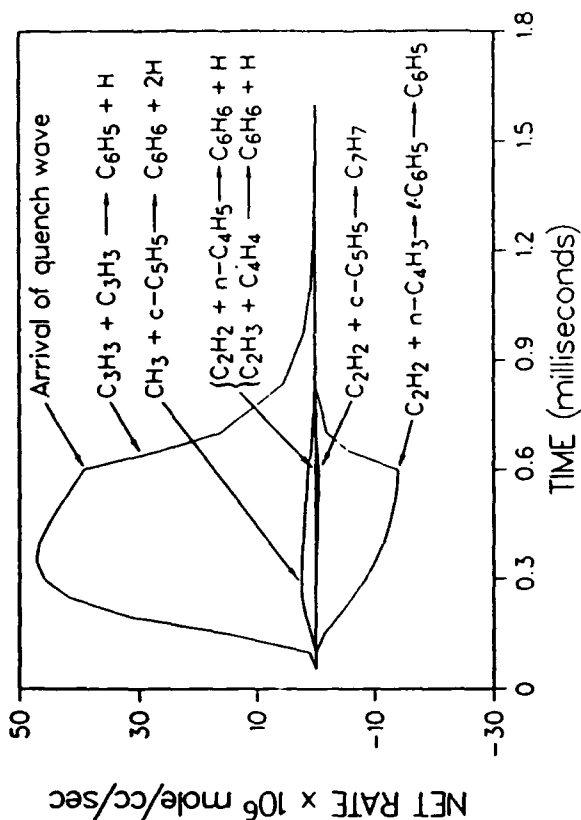
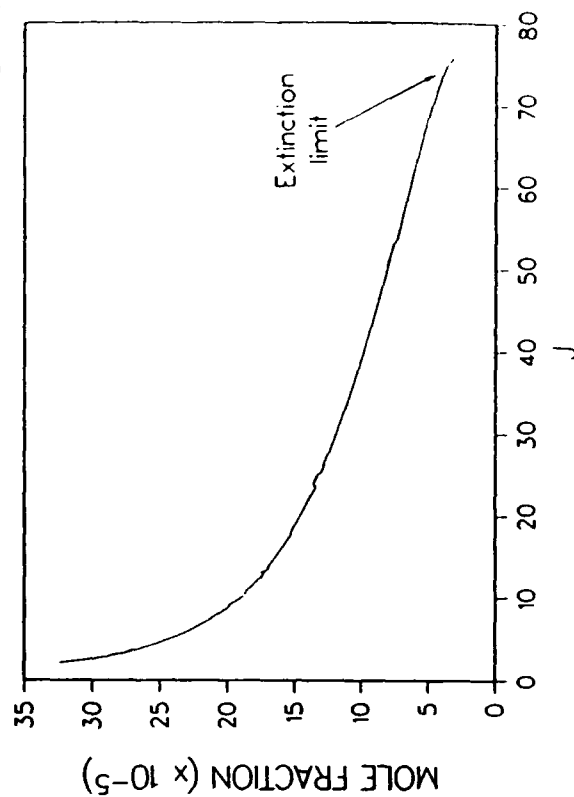


FIG. 4 PEAK BENZENE AS FUNCTION OF STRAIN LAMINAR OPPOSED JET DIFFUSION FLAME



Appendix B

Influence of Radiative Loss on Nitric Oxide Formation in Counterflow Diffusion Flames at High Pressure

Influence of Radiative Loss on Nitric Oxide Formation in Counterflow Diffusion Flames at High Pressure

A. VRANOS

AB Research Associates, South Windsor, CT

and

R. J. HALL

United Technologies Research Center, East Hartford, CT

A theoretical analysis is given of the effect of nonluminous thermal radiation on the properties of counterflow diffusion flames at high pressure. The self-consistent analysis includes an expression for gas band radiant dissipation in the energy equation of a counterflow flame solver. NO_x formation rates and other properties are studied as a function of strain rate for adiabatic, optically thin, and optical thickness-corrected flames. For adiabatic flames, NO_x concentration and flame temperature increase continuously with decreasing strain rate. For radiating flames, a temperature level off is exhibited due to the competing effects of heat loss and extent of reaction as strain rate (inverse residence time) decreases. For the very lowest strain rates, up to 5% of the flame enthalpy is converted to radiation, and optical thickness corrections start to become important. Certain factors that need to be taken into account in relating the isolated flamelet results to practical gas turbine combustors are also discussed.

INTRODUCTION

The objective of this study was to estimate the influence of nonluminous radiative heat loss on nitric oxide formation in high-pressure, counterflow diffusion flames. Previous studies of atmospheric counterflow diffusion flames have shown that radiative cooling can reduce NO_x concentrations appreciably [1-4]. In this report, an analysis of radiative heat loss in a high pressure (10.5 bar) counterflow flame is described. The resulting formulation is used as a basis for discussing the influence of radiative loss on nitric oxide formation in an aircraft gas turbine combustor. An order of magnitude estimate of combustor mean strain rate, computed from one-dimensional scalar decay rate measurements in a cross flow jet mixing configuration, is used to establish an appropriate range of strain rates for the counterflow calculation. The question whether gas band radia-

tive loss has a pronounced effect on NO levels for practical gas turbine operating conditions is shown to depend strongly on the distribution of low strain rate flamelets.

ANALYTICAL METHODS

Stretched Flame Model

The flow field is computed using a comprehensive code developed by Smooke et al. [5-7]. Detailed kinetics and transport effects are included in a quasi-one dimensional analysis of diffusive combustion, namely air and fuel fed oppositely to the reaction zone. The structure of the flame is obtained as a solution of a set of coupled nonlinear, two point, boundary value problems along the stagnation streamline. The strain rate enters the calculation as a boundary condition that specifies the velocity components along the edge of the boundary layer.

The kinetics data set, limited to C1 chemistry for methane fuel, consisted of 126 reactions and 30 species culled from a more comprehensive set of 213 reactions and 57 species developed by Glarborg et al. [8]. NO₂ chemistry was not considered. The reaction set and kinetic rate constants are present in Appendix A. The methane fuel temperature was selected to provide the same adiabatic flame temperature as jet fuel at the same operating conditions. Combustor pressure was 10.5 atm, typical of the cruise condition.

Theory of Radiative Power Loss from Counterflow Flames

The effect of gas band radiation on flame temperature and species concentrations was calculated in a self-consistent manner by incorporating a nonadiabatic radiative power loss term for a plane-parallel layer into the energy equation of the counterflow flame code [6, 7]. In the notation of Refs. 6 and 7 the energy equation becomes

$$\frac{d}{dy} \left(\lambda \frac{dT}{dy} \right) - c_p V \frac{dT}{dy} - \sum_{k=1}^K \rho Y_k V_{ky} c_{pk} \frac{dT}{dy} - \sum_{k=1}^K \dot{w}_k W_k h_k - \frac{dq_r}{dy} = 0, \quad (1)$$

where the term dq_r/dy is the divergence of the net radiative flux, q_r . The nomenclature for the rest of Eq. 1 is as given in the references; the other terms on the l.h.s. reading from left to right represent conduction, convection, diffusive transport, and energy release, respectively. The flux divergence or radiative source term was calculated in the manner given in Ref. 9, which used certain of the results given in Ref. 10. It is based on the use of wideband gas radiation models for H₂O, CO₂, and CO with provision for finite optical thickness effects in the high pressure broadening limit. Self-absorption of emitted radiation was calculated by taking hemispherical averages of the solution for the radiative flux, and integrating the result over the molecular absorption band-shapes. Although the optically thin approxima-

tion will usually be adequate, finite thickness effects can become important at low strain rate and high pressure, as will be seen. Previous theoretical analyses [1-4] have been limited to the optically thin case. The radiative source term is accordingly

$$\begin{aligned} \frac{dq_r}{dy} = & 4\pi \sum_{ij} \alpha_{ij} \rho_i I_{bij} - 2\pi \sum_{ij} \left(\frac{\alpha \rho}{\omega} (y) \right)_{ij} \\ & \times \left[\frac{\bar{\alpha} \bar{\rho}}{1 + \bar{\omega}/\omega} (\Gamma(1 + \bar{\omega}/\omega) \right. \\ & \times \gamma^*(1 + \bar{\omega}/\omega, \tau) + E_1(\tau) \Big]_{ij, y=y_f} \\ & \times \int dy' I_{bij} \end{aligned} \quad (2)$$

$$\int dy' I_{bij} = \int_{-\infty}^y dy' I_{bij} \quad (y > y_f),$$

$$= \int_y^{\infty} dy' I_{bij} \quad (y < y_f),$$

where the first and second terms on the r.h.s. represent emission and absorption, respectively; the summation ij is over all active bands of H₂O, CO₂, and CO; α_{ij} represents the integrated band intensity; ρ_i the mass density of the active molecule; I_{bij} the Planck function evaluated at the band center frequency; τ is the band center optical depth between the point of maximum flame temperature, y_f , and y ; and ω is the bandwidth parameter. Overbars in the nonlocal absorption term denote either path-averaged properties or properties based on path-averaged temperature taken between the point y and y_f . E_1 , Γ , and γ^* are the exponential integral, gamma function, and incomplete gamma function, respectively [11]. Band overlap contributions are ignored in this analysis. A quantity of interest that can be calculated from the converged solution is the fraction of the enthalpy that is converted to radiation. Given that the fourth term in Eq. 1 is the local rate of energy release, the frac-

tional radiative power loss is [12]

$$\frac{\int_{-x}^x \frac{dq_r}{dy} dy}{|\int_{-x}^x - \sum_k \dot{w}_k W_k h_k dy|} \quad (3)$$

The absorption term in Eq. 2 can represent a computational burden, and the overall economy of the program was maintained by omitting the radiative terms from the recalculation of the Jacobian matrix employed in the Newton's method solution of the nonlinear difference equation set [12]. Eq. 2 itself is an "analytic approximation" to an exact but time-consuming solution for the thickness term that has been suggested by the results of Ref. 10. In the general formulation of the radiative source term given in Ref. 9, it is possible to take into account nonvacuum boundary conditions (emission from black, hot boundaries), but this was omitted from the present calculations.

Combustor Mean Strain Rate

The preceding analysis is used to assess the influence of gas band radiation on nitric oxide formation in an aircraft gas turbine combustor. The combustor flame is viewed as an ensemble of flamelets convected by the mean flow, and the combustion process is assumed to be diffusion driven (no premixing) with air and fuel entering through separate boundaries. Relevant flamelet properties such as maximum flame temperature and NO concentration are described conveniently as a function of the strain rate boundary condition. For otherwise fixed boundary conditions, the flamelet strain rate and mean flamelet scalar dissipation rate are uniquely related. Thus, the flamelet model can be applied to a combustor flame if the mean combustor scalar dissipation is known. An order of magnitude estimate of the dissipation rate is obtained from recent measurements of unmixedness in a cylindrical model combustor with multijet cross flow injection [13]. Planar distributions of unmixedness are used to compute area-average unmixedness as a function of the streamwise coordinate. The

one-dimensional, streamwise rate of decay of jet fluid concentration is inferred from the mean velocity.

The following equations describe the volumetric mean scalar dissipation rate for normal injection from a row of holes in a single plane normal to the duct axis.

$$\begin{aligned} \bar{\chi}(X/D) = 0.52 \frac{\bar{Z}^3}{(1 - \bar{Z})} J^{-0.654} \bar{U}/D \\ \times \frac{1}{\left(\frac{X}{D} - \left(\frac{X}{D}\right)_0\right)} \\ \times \left[\left(\frac{X}{D}\right)^{-3.22} - \left(\frac{X}{D_0}\right)^{-3.22} \right], \quad (4) \end{aligned}$$

$$(X/D)_0 = 0.40 J^{-0.203},$$

where $\bar{\chi}$ is the volumetric mean scalar dissipation rate, \bar{Z} is the mass fraction of jet fluid based on the jet and approach stream mass flows, \bar{U} is the approach stream mean velocity, and J is the single jet momentum flux ratio.

It is seen that $\bar{\chi}$ depends on \bar{Z} , and so is, in fact, a function of the number of injection stages and the rate of air addition per stage. In this example, it is assumed that one half the dilution air is added at the primary zone exit and that this fluid is thoroughly mixed in one combustor height (or diameter). For typical values of $J = 23$ and $Z = 0.53$, $\bar{\chi} = 121 \text{ s}^{-1}$ corresponding to a mean strain rate of 330 s^{-1} .

This estimate of mean strain rate can be checked for correct order of magnitude using the fundamental relationship for viscous dissipation [14].

$$\epsilon_v = A(u')^3/\Lambda, \quad (5)$$

where A is a constant near unity (herein assumed to be unity), u' is the rms turbulence intensity for isotropic turbulence, and Λ is the integral scale of turbulence. Assuming typical values of $u' = 129 \text{ cm/s}$ and $\Lambda = 1.0 \text{ cm}$ for

the combustor primary zone, the resulting flamelet dissipation is $2.1 \times 10^6 \text{ cm}^2/\text{s}^3$. A mean dissipation within the flamelet is given by the expression

$$\epsilon_f = \frac{4}{3} \bar{\nu} \left(\frac{\partial v}{\partial y} \right)_f^2, \quad (6)$$

where $\bar{\nu}$ is the average flamelet kinematic viscosity. Substituting $v_0 = -2ay$, where a is the strain rate and v_0 is the normal velocity relative to the stagnation point, and letting $\epsilon_v = \epsilon_f$ yields $a = 474 \text{ s}^{-1}$.

RESULTS

The influence of radiative loss on temperature is seen in Fig. 1, where peak flamelet temperature is plotted as a function of strain rate for adiabatic, optically thin and thickness-corrected calculations. The effect of radiation

on temperature becomes more pronounced as strain rate decreases, where it can also be seen that thickness corrections have to be taken into account for the lowest strain rates ($20\text{--}30 \text{ s}^{-1}$). All curves converge at sufficiently high strain rate as a result of diminishing radiative loss. These results are mirrored in the dependence of peak nitric oxide concentration on strain rate, shown in Fig. 2. The sensitivity to temperature is in accordance with the fact that most of the nitric oxide is formed via the thermal (Zeldovich) mechanism. Differences between the optically thin and thickness-corrected model also become more apparent at low strain rate. The corresponding radiative loss, expressed as a fraction of the integrated energy release is presented in Fig. 3. Within the framework of the present analysis, it is not possible to make a definite statement that non-luminous radiation should have a significant influence on nitric oxide formation in a practi-

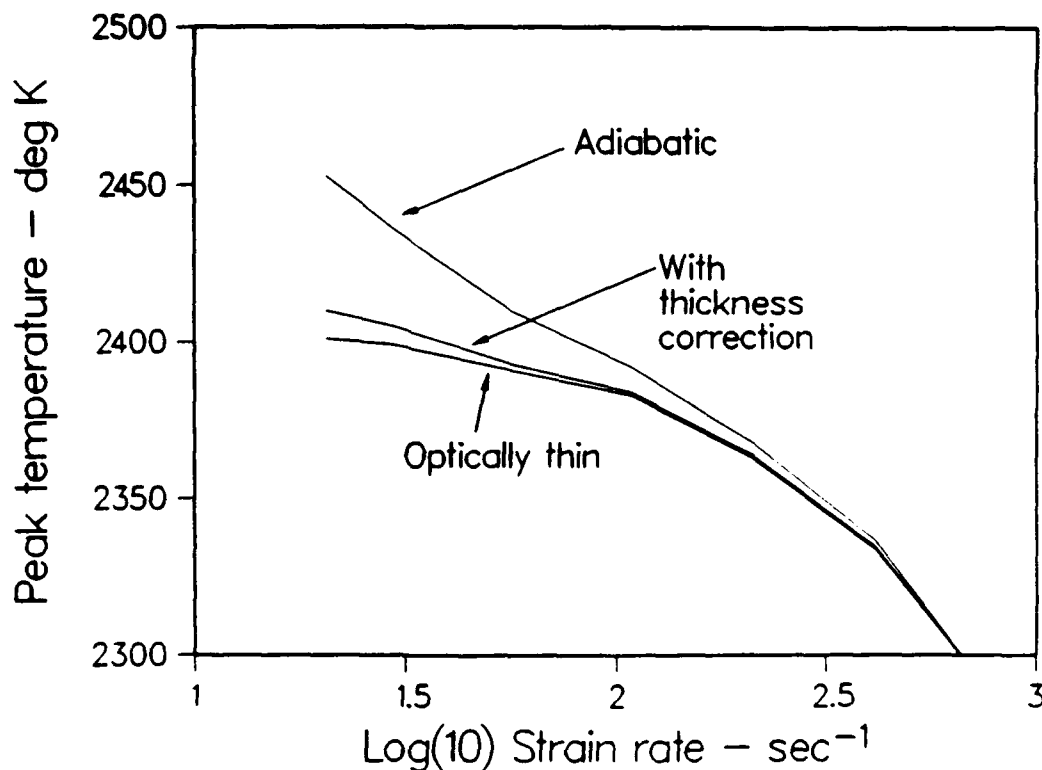


Fig. 1. Peak temperature in high-pressure counterflow flames versus strain rate with and without radiation. The range of strain rates is $20\text{--}800 \text{ s}^{-1}$.

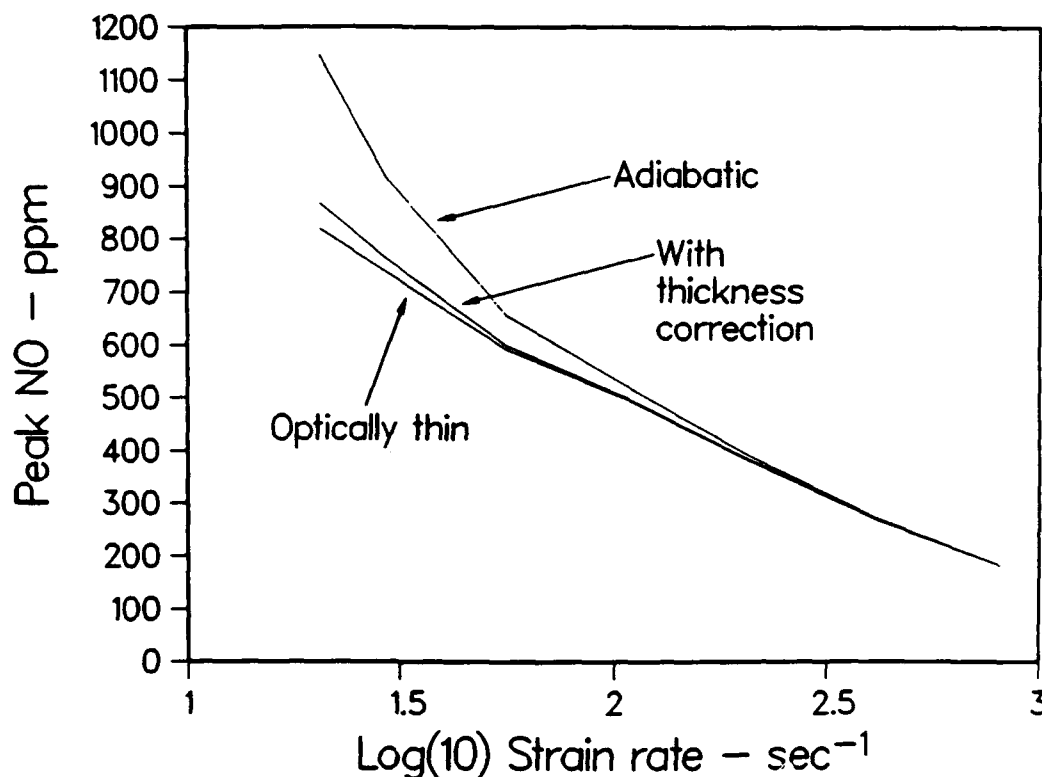


Fig. 2. Effect of radiation on peak NO concentrations in high-pressure counterflow flames.

cal application. However, if the scalar dissipation rate is log-normally distributed, the calculations suggest that significant contributions to the weighted sum of nitric oxide could be expected from flamelets whose scalar dissipation rates are below the mean value. For example, at 5% loss, the reduction in peak NO levels relative to the adiabatic solution is about 30%. Thus, it appears that detailed calculations of radiation in combustors are worth pursuing. In this regard, practical applications require consideration of the influence of neighboring flamelets on net emission from the turbulent flame. Radiative interactions between flamelets and overall optical thickness effects could cause gas cooling rates in practical contexts to be less than that calculated here. Radiative loss from soot and its effect on nitric oxide could be much more significant. The theoretical expression for the radiative loss (Eq. 2) can be extended readily to include particulate emission. There is a need, too, for a more comprehensive and systematic study of

the effects of pressure, peak temperature, and strain rate on radiative loss in opposed jet flames. This is beyond the scope of the present article, however, and will be addressed in a future publication.

CONCLUSIONS

A gas band radiation term has been included in the energy equation for counterflow diffusion flames, providing a self-consistent analysis of the effects of radiation on flame temperature and NO levels. For conditions representative of a gas turbine combustor, radiative corrections can become important for low strain rates, with up to 5% conversion of enthalpy to radiation, and reductions of approximately 30% in peak NO levels relative to the adiabatic solution. At high pressures and low flamelet strain rates, optical thickness corrections are required for high accuracy. The question whether gas band radiative loss has a pronounced effect on NO levels for practical gas

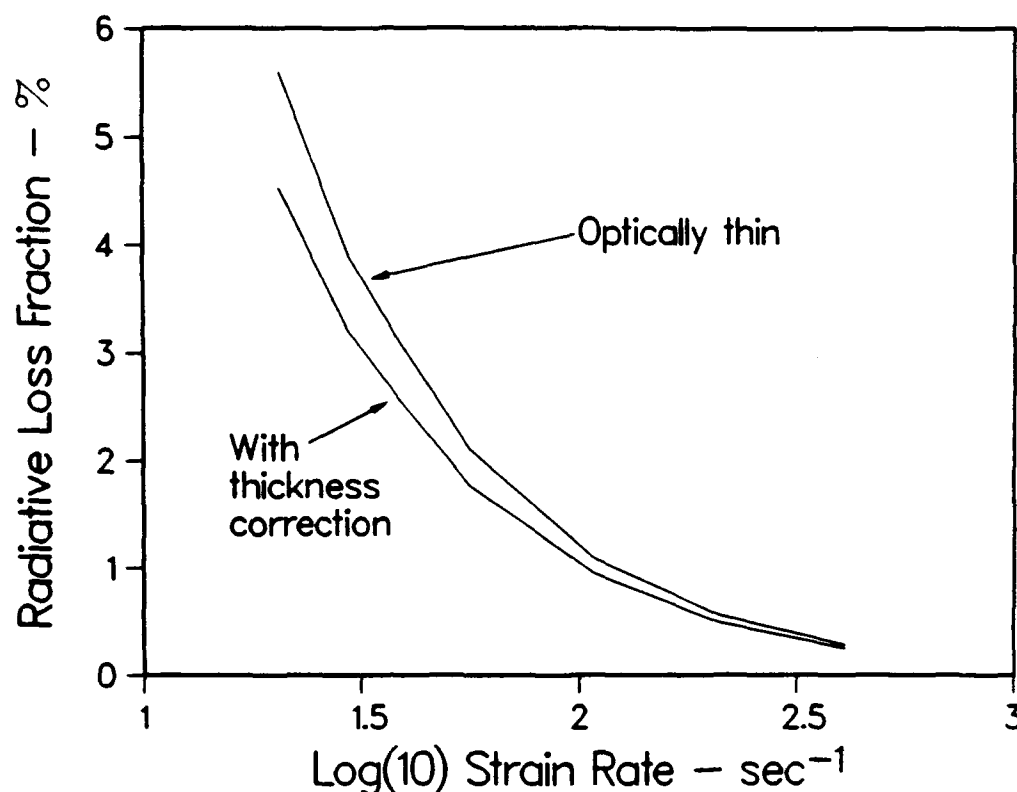


Fig. 3. Nonadiabatic radiative power loss in counterflow flames versus strain rate.

turbine operating conditions is shown to depend strongly on the distribution of low-strain-rate flamelets.

The authors would like to thank Prof. M. D. Smooke of Yale University for his advice on aspects of the counterflow diffusion flame program, Dr. M. B. Colket of UTRC for his assistance with the chemical mechanism, and Kathi Wicks for her assistance with the preparation of this manuscript. Portions of this research were carried out under the sponsorship of AFOSR Contract F49620-91-C-0056.

REFERENCES

1. Liu, Y., and Rogg, B., in *Heat Transfer in Radiating and Combusting Systems* (M. G. Carvalho, F. Lockwood, and J. Taine, Eds.), Springer-Verlag, 1990, p. 114.
2. Sohrab, S. H., Linan, A., and Williams, F. A., *Combust. Sci. Technol.* 27:143-154 (1982).
3. Chen, J. Y., and Kollmann, W., *Combust. Flame* 88:397-412 (1991).
4. Muller, U. C., Mans, F., and Peters, N., Poster presentation at Twenty-Third Symposium (International) on Combustion, Orleans, France, 1990.
5. Smooke, M. D., Miller, J. A., and Kee, R. J., *Combust. Sci. Technol.* 34:79-85 (1983).
6. Smooke, M. D., Puri, I. K., and Seshadri, K., *Twenty-First Symposium (International) on Combustion*, The Combustion Institute, Pittsburgh, 1986, pp. 1783-1792.
7. Giovangigli, V., and Smooke, M. D., Yale University Department of Mechanical Engineering Report ME-103-86, October 1986.
8. Glarborg, P., Miller, J. P., and Kee, R. J., *Combust. Flame* 65:177-202 (1986).
9. Hall, R. J., *JQSRT*, 1993 (in press).
10. Modak, A. T., Factory Mutual Research Technical Report 22355-1, 1974.
11. Abramowitz, M., and Stegun, I. A. (Eds.), *Handbook of Mathematical Functions*, Dover, 1970, Chap. 6.
12. Smooke, M. D., private communication, 1992.
13. Vranos, A., Liscinsky, D. S., and Truc, B., NASA TM 105180, 1991.
14. Tennekes, H., and Lumley, J. L., *A First Course in Turbulence*, MIT Press, 1972.

Received 16 July 1992; revised 17 November 1992

APPENDIX A

Reaction Mechanism Rate Coefficients in the Form $k_f = AT^B \exp(-E_0/RT)$. Units are moles, cubic centimeters, seconds, Kelvin, and calories / mole.

	Reaction	A	β	E
1.	$H + O_2 = O + OH$	5.10E16	-0.820	16510.
2.	$H_2 + O = H + OH$	1.80E10	1.0	8830.
3.	$H_2 + OH = H_2O + H$	1.20E09	1.3	3630.
4.	$OH + OH = H_2O + O$	6.0E08	1.3	0.
5.	$H + OH + M = H_2O + M (M = AR)$ $H_2O/20./^a$	7.50E23	-2.6	0.
6.	$O_2 + M = O + O + M$	1.90E11	0.5	95560.
7.	$H + H + M = H_2 + M (M = AR)$ $H_2O/0.0/H_2/0.0/CO_2/0.0/^b$	1.0E18	-1.0	0.
8.	$H + H + H_2 = H_2 + H_2$	9.20E16	-0.6	0.
9.	$H + H + H_2O = H_2 + H_2O$	6.00E19	-1.250	0.
10.	$H + H + CO_2 = H_2 + CO_2$	5.49E20	-2.0	0.
11.	$H_2 + O_2 = OH + OH$	1.70E13	0.0	47780.
12.	$H + O_2 + M = HO_2 + M (M = AR)$ $H_2O/21./CO_2/5./H_2/3.3/CO/2./O_2/0./N_2/0./^c$	2.10E18	-1.0	0.
13.	$H + O_2 + O_2 = HO_2 + O_2$	6.70E19	-1.420	0.
14.	$H + O_2 + N_2 = HO_2 + N_2$	6.70E19	-1.420	0.
15.	$HO_2 + H = H_2 + O_2$	2.50E13	0.	700.
16.	$HO_2 + H = OH + OH$	2.50E14	0.	1900.
17.	$HO_2 + O = OH + O_2$	4.80E13	0.	1000.
18.	$HO_2 + OH = H_2O + O_2$	5.00E13	0.	1000.
19.	$HO_2 + HO_2 = H_2O_2 + O_2$	2.00E12	0.	0.
20.	$H_2O_2 + M = OH + OH + M$	1.20E17	0.	45500.
21.	$H_2O_2 + H = HO_2 + H_2$	1.70E12	0.0	3750.
22.	$H_2O_2 + OH = H_2O + HO_2$	1.00E13	0.0	1800.
23.	$CO + O + M = CO_2 + M$	3.20E13	0.0	-4200.
24.	$CO + O_2 = CO_2 + O$	2.50E12	0.	47700.
25.	$CO + OH = CO_2 + H$	1.50E07	1.3	-760.
26.	$CO + HO_2 = CO_2 + OH$	5.80E13	0.	22930.
27.	$CH_4 + M = CH_3 + H + M (M = AR)$ $H_2O/5./^d$	1.00E17	0.	88000.
28.	$CH_4 + H = CH_3 + H_2$	2.20E04	3.0	8750.
29.	$CH_4 + O = CH_3 + OH$	1.20E07	2.080	7630.
30.	$CH_4 + OH = CH_3 + H_2O$	3.50E03	3.080	2000.
31.	$CH_4 + CH_2 = CH_3 + CH_3$	1.30E13	0.	9500.
32.	$CH_3 + M = CH_2 + H + M$	1.90E16	0.	91600.
33.	$CH_3 + H = CH_2 + H_2$	9.00E13	0.	15100.
34.	$CH_3 + O = CH_2O + H$	6.80E13	0.	0.
35.	$CH_3 + O = CH_2 + OH$	5.00E13	0.	12000.
36.	$CH_3 + OH = CH_2 + H_2O$	1.50E13	0.	5000.
37.	$CH_3 + OH = CH_2O + H_2$	1.00E12	0.	0.
38.	$CH_3 + O_2 = CH_2O + OH$	5.20E13	0.	34570.
39.	$CH_3 + O_2 = CH_3O + O$	7.00E12	0.	25650.
40.	$CH_3O + M = CH_2O + H + M$	1.00E14	0.	25000.
41.	$CH_3O + H = CH_2O + H_2$	2.00E13	0.0	0.
42.	$CH_3O + O = CH_2O + OH$	1.00E13	0.	0.
43.	$CH_3O + OH = CH_2O + H_2O$	1.00E13	0.	0.
44.	$CH_3O + O_2 = CH_2O + HO_2$	6.30E10	0.	26000.
45.	$CH_2O + M = HCO + H + M$	3.31E16	0.0	81000.
46.	$CH_2O + H = HCO + H_2$	2.20E08	1.770	10500.
47.	$CH_2O + O = HCO + OH$	1.80E13	0.0	3080.
48.	$CH_2O + OH = HCO + H_2O$	3.40E09	1.180	447.
49.	$HCO + M = CO + H + M$	1.60E14	0.	14700.

50.	$\text{HCO} + \text{H} = \text{CO} + \text{H}_2$	4.00E13	0.0	0.0
51.	$\text{HCO} + \text{O} = \text{CO} + \text{OH}$	3.00E13	0.0	0.0
52.	$\text{HCO} + \text{O} = \text{CO}_2 + \text{H}$	3.00E13	0.0	0.0
53.	$\text{HCO} + \text{OH} = \text{CO} + \text{H}_2\text{O}$	5.00E12	0.0	0.0
54.	$\text{HCO} + \text{O}_2 = \text{CO} + \text{HO}_2$	3.30E13	-0.4	0.0
55.	$\text{CH}_2 + \text{H} = \text{CH} + \text{H}_2$	7.30E17	-1.560	0.
56.	$\text{CH}_2 + \text{O} = \text{CO} + \text{H} + \text{H}$	3.00E13	0.0	0.
57.	$\text{CH}_2 + \text{O} = \text{CO} + \text{H}_2$	5.00E13	0.0	0.
58.	$\text{CH}_2 + \text{O} = \text{CH} + \text{OH}$	5.00E13	0.0	12000.
59.	$\text{CH}_2 + \text{OH} = \text{CH}_2\text{O} + \text{H}$	3.00E13	0.0	0.
60.	$\text{CH}_2 + \text{OH} = \text{CH} + \text{H}_2\text{O}$	4.50E13	0.0	3000.
61.	$\text{CH}_2 + \text{O}_2 = \text{CO}_2 + \text{H} + \text{H}$	1.60E12	0.0	1000.
62.	$\text{CH}_2 + \text{O}_2 = \text{CO}_2 + \text{H}_2$	6.90E11	0.0	500.
63.	$\text{CH}_2 + \text{O}_2 = \text{CO} + \text{H}_2\text{O}$	1.90E10	0.0	-1000.
64.	$\text{CH}_2 + \text{O}_2 = \text{CO} + \text{OH} + \text{H}$	8.60E10	0.0	-500.
65.	$\text{CH}_2 + \text{O}_2 = \text{HCO} + \text{OH}$	4.30E10	0.0	-500.
66.	$\text{CH}_2 + \text{O}_2 = \text{CH}_2\text{O} + \text{O}$	2.00E13	0.0	9000.
67.	$\text{CH}_2 + \text{CO}_2 = \text{CO} + \text{CH}_2\text{O}$	1.10E11	0.0	1000.
68.	$\text{CH} + \text{O} = \text{CO} + \text{H}$	5.70E13	0.0	0.
69.	$\text{CH} + \text{OH} = \text{HCO} + \text{H}$	3.00E13	0.0	0.
70.	$\text{CH} + \text{O}_2 = \text{HCO} + \text{O}$	3.30E13	0.0	0.
71.	$\text{CH} + \text{CO}_2 = \text{HCO} + \text{CO}$	3.40E12	0.0	690.
72.	$\text{NH}_3 + \text{M} = \text{NH}_2 + \text{H} + \text{M}$	1.40E16	0.0	90600.
73.	$\text{NH}_3 + \text{H} = \text{NH}_2 + \text{H}_2$	7.00E06	2.390	10171.
74.	$\text{NH}_3 + \text{O} = \text{NH}_2 + \text{OH}$	2.10E13	0.0	9000.
75.	$\text{NH}_3 + \text{OH} = \text{NH}_2 + \text{H}_2\text{O}$	2.04E06	2.04	566.
76.	$\text{NH}_2 + \text{H} = \text{NH} + \text{H}_2$	6.90E13	0.0	3650.
77.	$\text{NH}_2 + \text{O} = \text{NH} + \text{OH}$	6.80E12	0.0	0.0
78.	$\text{NH}_2 + \text{O} = \text{HNO} + \text{H}$	6.60E14	-0.5	0.
79.	$\text{NH}_2 + \text{OH} = \text{NH} + \text{H}_2\text{O}$	4.50E12	0.0	2200.
80.	$\text{NH}_2 + \text{N} = \text{N}_2 + \text{H} + \text{H}$	7.20E13	0.0	0.
81.	$\text{NH}_2 + \text{NO} = \text{N}_2 + \text{H} + \text{OH}$	8.80E15	-1.250	0.
82.	$\text{NH}_2 + \text{NO} = \text{N}_2 + \text{H}_2\text{O}$	3.80E15	-1.25	0.0
83.	$\text{NH} + \text{H} = \text{N} + \text{H}_2$	3.00E13	0.0	0.
84.	$\text{NH} + \text{O} = \text{NO} + \text{H}$	2.00E13	0.0	0.
85.	$\text{NH} + \text{OH} = \text{HNO} + \text{H}$	2.00E13	0.0	0.
86.	$\text{NH} + \text{OH} = \text{N} + \text{H}_2\text{O}$	5.00E11	0.5	2000.
87.	$\text{NH} + \text{O}_2 = \text{HNO} + \text{O}$	1.00E13	0.0	12000.
88.	$\text{NH} + \text{O}_2 = \text{NO} + \text{OH}$	1.4E11	0.0	2000.
89.	$\text{NH} + \text{NO} = \text{N}_2\text{O} + \text{H}$	4.30E14	-0.5	0.0
90.	$\text{NH} + \text{N} = \text{N}_2 + \text{H}$	3.00E13	0.0	0.
91.	$\text{N} + \text{O}_2 = \text{NO} + \text{O}$	6.40E09	1.0	6280.
92.	$\text{N} + \text{OH} = \text{NO} + \text{H}$	3.80E13	0.0	0.0
93.	$\text{N} + \text{NO} = \text{N}_2 + \text{O}$	3.30E12	0.3	0.
94.	$\text{N} + \text{CO}_2 = \text{NO} + \text{CO}$	1.90E11	0.0	3400.
95.	$\text{HNO} + \text{M} = \text{H} + \text{NO} + \text{M} (\text{M} = \text{Ar})$	1.50E16	0.0	48680.
96.	$\text{H}_2\text{O}/6 / \text{H}_2/2 / \text{O}_2/2 / \text{N}_2/2 /$			
96.	$\text{HNO} + \text{H} = \text{H}_2 + \text{NO}$	5.00E+12	0.0	0.0
97.	$\text{HNO} + \text{OH} = \text{NO} + \text{H}_2\text{O}$	3.6E13	0.0	0.0
98.	$\text{N}_2\text{O} + \text{M} = \text{N}_2 + \text{O} + \text{M}$	1.60E14	0.0	51600.
99.	$\text{N}_2\text{O} + \text{H} = \text{N}_2 + \text{OH}$	7.60E13	0.0	15200.
100.	$\text{N}_2\text{O} + \text{O} = \text{NO} + \text{NO}$	1.00E14	0.0	28200.
101.	$\text{N}_2\text{O} + \text{O} = \text{N}_2 + \text{O}_2$	1.00E14	0.0	28200.
102.	$\text{HCN} + \text{O} = \text{CN} + \text{OH}$	2.70E09	1.580	26600.
103.	$\text{HCN} + \text{O} = \text{NCO} + \text{H}$	1.40E04	2.64	4980.
104.	$\text{HCN} + \text{O} = \text{NH} + \text{CO}$	3.50E03	2.64	4980.
105.	$\text{HCN} + \text{OH} = \text{CN} + \text{H}_2\text{O}$	1.5E13	0.0	10929.
106.	$\text{CN} + \text{O} = \text{CO} + \text{N}$	1.80E13	0.0	0.
107.	$\text{CN} + \text{OH} = \text{NCO} + \text{H}$	6.00E13	0.0	0.0
108.	$\text{CN} + \text{H} = \text{HCN} + \text{H}$	3.00E05	2.45	2237.
109.	$\text{CN} + \text{O}_2 = \text{NCO} + \text{O}$	5.60E12	0.0	0.0

110.	$\text{CN} + \text{N}_2\text{O} = \text{NCO} + \text{N}_2$	1.00E13	0.0	0.
111.	$\text{NCO} + \text{M} = \text{N} + \text{CO} + \text{M}$	3.10E16	-0.5	48000.
112.	$\text{NCO} + \text{H} = \text{NH} + \text{CO}$	5.00E13	0.0	0.
113.	$\text{NCO} + \text{O} = \text{NO} + \text{CO}$	5.60E13	0.0	0.
114.	$\text{NCO} + \text{OH} = \text{NO} + \text{CO} + \text{H}$	1.00E13	0.0	0.
115.	$\text{NCO} + \text{N} = \text{N}_2 + \text{CO}$	2.00E13	0.0	0.
116.	$\text{NCO} + \text{NO} = \text{N}_2\text{O} + \text{CO}$	1.00E13	0.0	-390.
117.	$\text{CH} + \text{NO} = \text{HCN} + \text{O}$	1.10E14	0.0	0.
118.	$\text{CH} + \text{N}_2 = \text{HCN} + \text{N}$	1.90E11	0.0	13600.
119.	$\text{CH}_2 + \text{N}_2 = \text{HCN} + \text{NH}$	1.00E13	0.0	74000.
120.	$\text{CH} + \text{NH}_2 = \text{HCN} + \text{H} + \text{H}$	3.00E13	0.0	0.
121.	$\text{CH} + \text{NH} = \text{HCN} + \text{H}$	5.00E13	0.0	0.
122.	$\text{CH}_2 + \text{NH} = \text{HCN} + \text{H} + \text{H}$	3.00E13	0.0	0.
123.	$\text{CH} + \text{N} = \text{CN} + \text{H}$	1.30E13	0.0	0.
124.	$\text{CH}_2 + \text{N} = \text{HCN} + \text{H}$	5.00E13	0.0	0.
125.	$\text{CH}_3 + \text{N} = \text{HCN} + \text{H} + \text{H}$	5.00E13	0.0	0.
126.	$\text{CH}_4 + \text{N} = \text{NH} + \text{CH}_3$	1.00E13	0.0	24000.

^aThird-body efficiencies: $k_5(\text{H}_2\text{O}) = 20k_5(\text{Ar})$.

^bThird-body efficiencies: $k_7(\text{H}_2\text{O}) = k_7(\text{H}_2) = k_7(\text{CO}_2) = 0k_7(\text{Ar})$.

^cThird-body efficiencies: $k_{12}(\text{H}_2\text{O}) = 21k_{12}(\text{Ar})$, $k_{12}(\text{CO}_2) = 5k_{12}(\text{Ar})$, $k_{12}(\text{H}_2) = 3.3k_{12}(\text{Ar})$, $k_{12}(\text{CO}) = 2k_{12}(\text{Ar})$, $k_{12}(\text{O}_2) = 0k_{12}(\text{Ar})$, $k_{12}(\text{N}_2) = 0k_{12}(\text{Ar})$.

^dThird-body efficiencies: $k_{27}(\text{H}_2\text{O}) = 5k_{27}(\text{Ar})$.

^eThird-body efficiencies: $k_{95}(\text{H}_2\text{O}) = 6k_{95}(\text{Ar})$, $k_{95}(\text{H}_2) = k_{95}(\text{O}_2) = k_{95}(\text{N}_2) = 2k_{95}(\text{Ar})$.

Appendix C

Radiative Transfer in Sooting Counterflow Flames

Radiative Transfer in Sooting Counterflow Flames

by

Robert J. Hall
United Technologies Research Center
East Hartford, Conn.

It is well known that substantial fractions of flame energy can be converted to radiation (Ref. 1), and that the gas cooling resulting from this non-adiabatic loss can in turn affect flame chemistry, and lead to inaccuracies in prediction of pollutants like nitric oxide. These effects are expected to be most extreme in sooting flames. Quantitative assessment of these effects requires inclusion of an energy sink term in the flow energy equation. This sink term is given by the divergence of the net radiative flux, which is the difference of an emission term valid in the optically thin limit, and a self-absorption term that becomes important when optical thickness effects need to be accounted for. The expression for the emission term is generally trivial even when both soot and gas band radiation are present, and does not depend on flame geometry because only local properties are required. The self-absorption term is generally more difficult because a solution for the radiative flux is implicitly required. This term is complicated further when both soot and gas radiators are present because of absorption profile overlaps. In this paper, a complete solution for the radiative dissipation is given for the one-dimensional, plane-parallel or boundary layer flow problem. Both gas band and soot radiation are considered, and the resulting solution is valid for all degrees of optical thickness. The expression is given in semi-analytic form in terms of single quadratures normal to the flame structure. The theory will be illustrated by example calculations for a model, high pressure, sooting counterflow diffusion flame.

The main features of the theoretical analysis are as follows. The absorption terms are derived by taking hemispherical averages of frequency-dependent solutions of the equation of radiative transfer, and integrating them over the absorption bandshapes of both the molecules and the soot. The soot absorption coefficient is assumed to have the Rayleigh form, with scattering ignored. For nonuniform paths, the soot terms can be derived without approximation; for the gas band terms a form of the mean properties assumption is employed. The gas absorption profiles are assumed to have the wideband model form, and the transmissivities are appropriate to the high pressure-broadening limit. The absorptive part is expressible as four terms, which are too lengthy to reproduce here. Only the pure soot solution will thus be given here. Assuming that y represents the coordinate normal to the flame structure, the emission and absorption terms of the net radiative dissipation $Q = Q_{\text{EMISS}} - Q_{\text{ABS}}$ are expressible as:

$$Q_{\text{EMISS}} = 4\pi c_2^{-5} c_1 \cdot \int_0^\infty \frac{u^4}{e^u - 1} du \cdot c_s f_v(y) T^5(y) \quad (1)$$

where c_1 and c_2 are the Planck function constants, c_s is the constant in the Rayleigh soot absorption coefficient law $K_{\text{abs}}(\omega) = c_s \omega f_v$, f_v is the local soot volume fraction, T is the local temperature, and

$$Q_{\text{ABS}} = 2\pi c_s^2 c_1 f_v(y) \frac{5!}{(c_2)^6} \int_{-\infty}^{\infty} dy' f_v(y') T^6(y') \sum_{n=1}^{\infty} n^{-6} \quad (2)$$

$$\cdot \left[\ln \left(1 + \frac{P_n(y')}{Q_n(y')} \right) - \sum_{k=1}^5 \frac{1}{k} \left(\frac{P_n(y')}{P_n(y') + Q_n(y')} \right)^k \right]$$

where

$$P_n(y') = nc_2/T(y')$$

$$Q_n(y') = c_s \bar{f}_v |y - y'|$$

An implicit assumption has been that the dispersion of the soot index of refraction is small. Other terms give the rate of gas absorption of gas radiation, gas absorption of soot radiation, and soot absorption of gas radiation, and are expressible in terms of exponential integrals.

The generalized net radiative dissipation for both soot and gas molecules has been incorporated into a counterflow diffusion code solver, which includes detailed kinetics and transport effects (Ref. 2). The concentrations of the radiating species CO_2 , H_2O , and CO are derived in the counterflow solution, but the soot has been treated parametrically. Example calculations have been performed for a 10.5 atm, methane-air flame. The pressure approximates that of an aircraft gas turbine combustor at the cruise condition, and the fuel temperature has been adjusted to achieve a peak temperature approximating the adiabatic flame temperature of jet fuel (Ref. 3). The adiabatic (no radiation) temperature profile for this flame is shown in Figure 1, along with the assumed location

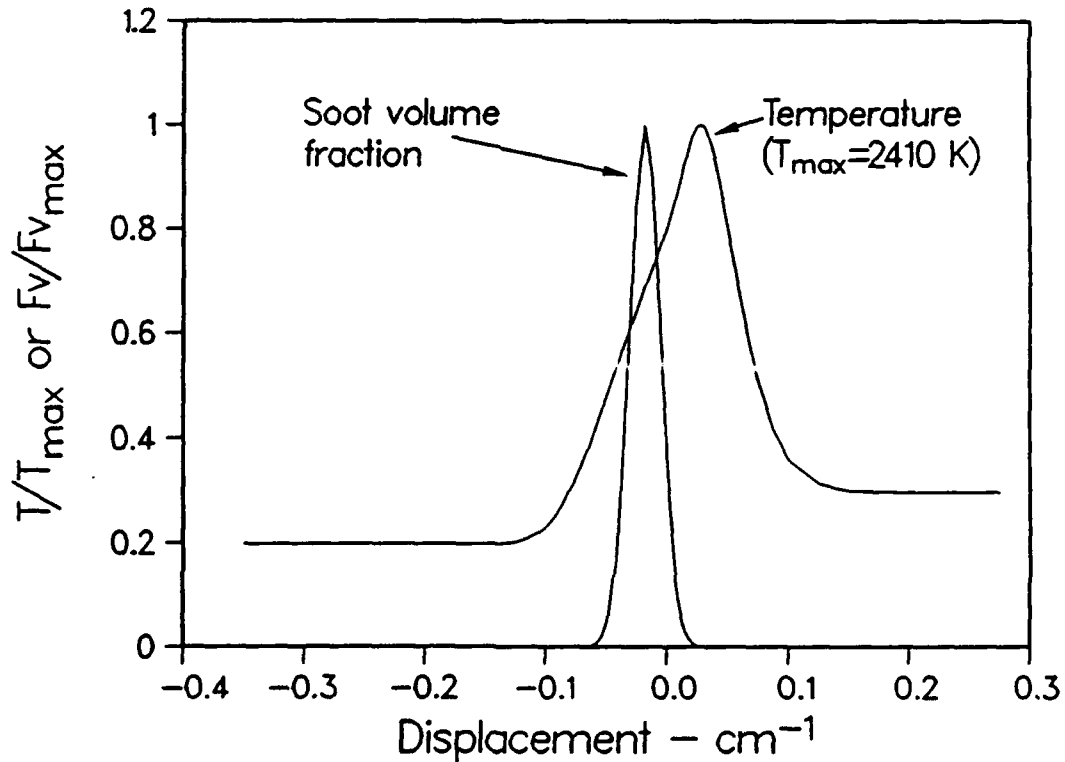


Figure 1. Temperature and soot profiles in model opposed jet flame.

of the soot profile. Since a soot growth model has not yet been included in the counterflow solver, the location, peak soot volume fraction, and width of the sooting zone are treated as parameters uncoupled from the flame solution. In the calculations to follow, the peak in the soot profile is assumed to occur at about 1650 K, with a bandwidth of 200 K, and the peak volume fraction is varied. The strain rate in these calculations is 56 sec^{-1} , a value which is felt to lie toward the lower end of the range of values of practical interest (Ref. 3); the strain rate enters the calculation as a boundary condition which specifies the velocity components along the edge of the boundary layer.

Figure 2 shows the fractional (%) conversion of flame energy to radiation as the peak soot volume fraction is varied. The lower asymptotic limit represents the contribution of gas band radiation alone. For peak soot volume fractions much in excess of 10^{-6} , the soot contributions become important, and for values approaching 10^{-4} , more than 10% of the flame energy is converted to radiation. A peak soot volume fraction of this magnitude might not be unreasonable at high pressure. Losses of this magnitude cool the gas sufficiently that marked effects are seen on the predicted nitric oxide profiles, as shown in Fig. 3. The kinetics data set is limited to C1 chemistry for methane fuel, and consists of 126 reactions and 30 species derived from a more comprehensive mechanism developed by Glarborg, et. al. (Ref. 4). Given the strong temperature dependences exhibited in Equations 1 and 2, the results will clearly have considerable sensitivity to the location of the soot line.

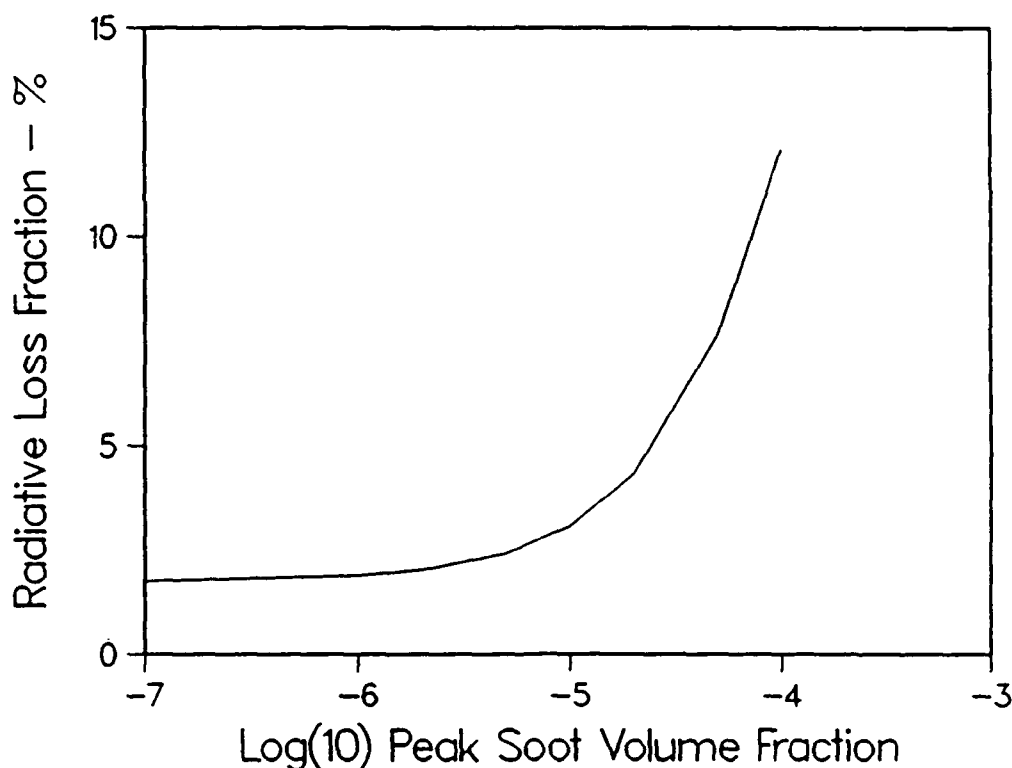


Figure 2. Variation of percentage conversion of flame energy to radiation with peak soot volume fraction.

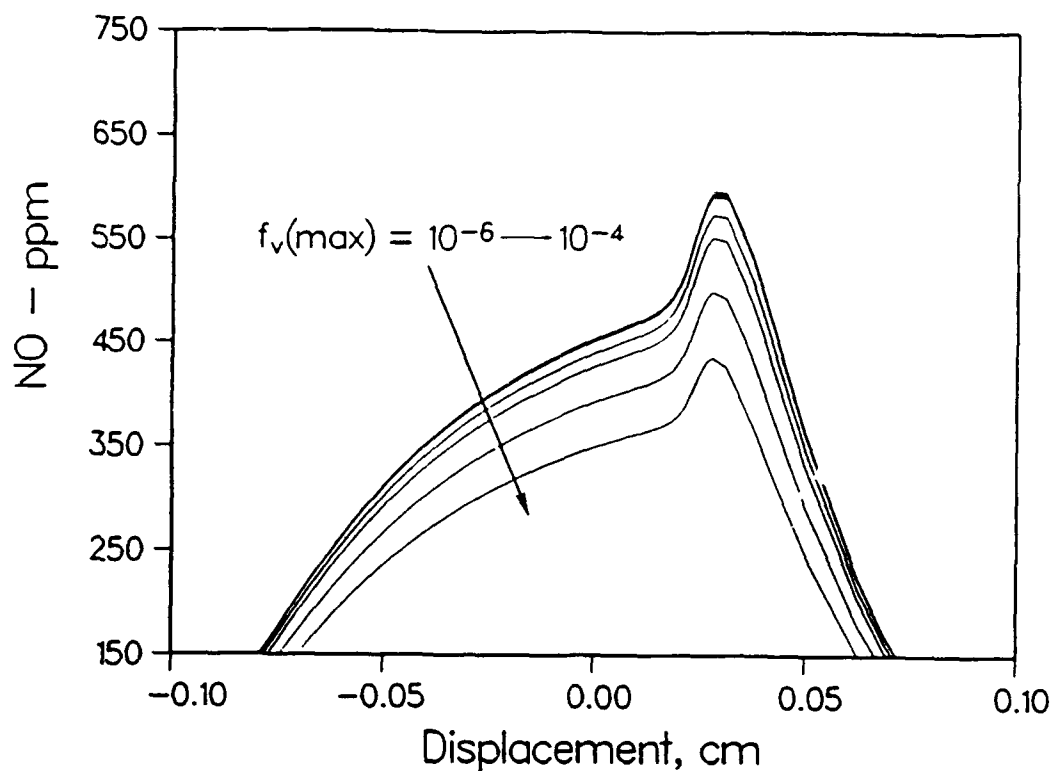


Figure 3. Effect of soot loading on nitric oxide profiles. The values of volume fraction are $1, 2, \& 5 \times 10^{-6}, 1, 2, \& 5 \times 10^{-5}, 10^{-4}$.

The full gas band and soot radiation expressions will be given in the paper. Other topics which will be discussed include the incorporation of realistic radiative wall boundary conditions, gas and soot radiative interchange, and absorption of soot radiation by the fuel.

References

1. D.K. Edwards and A. Balakrishnan, Comb. & Flame, 20, 401 (1973).
2. M.D. Smooke, J.A. Miller, and R.J. Kee, Comb. Sci. & Tech., 34, 79 (1983).
3. A. Vranos and R.J. Hall, "Influence of Radiative Loss on Nitric Oxide Formation in Counterflow Diffusion Flames at High Pressure", to appear in Comb. & Flame, 1993.
4. P. Glarborg, J.P. Miller, and R.J. Kee, Comb. & Flame, 65, 177 (1986).

Parts of this work were funded by AFOSR Contract F49620-91-C-0056

Appendix D

The Radiative Source Term for Plane-Parallel Layers of Reacting Combustion Gases

THE RADIATIVE SOURCE TERM FOR PLANE-PARALLEL LAYERS OF REACTING COMBUSTION GASES

ROBERT J. HALL

United Technologies Research Center, East Hartford, CT 06108, U.S.A.

(Received 3 June 1992; received for publication 11 November 1992)

Abstract—An expression is derived for the radiative source term governing the interaction of molecular gas band radiation and flow in nonhomogeneous, plane-parallel reacting flow problems. The divergence of the net radiative flux is formulated in terms of wide-band absorptance model parameters for combustion products, and is valid for all degrees of optical thickness. When optical thickness is finite, the net absorption is obtained by integrating the radiation field solution over the band lineshapes and taking hemispherical averages. Illustrative calculations for counterflow diffusion flames will be discussed.

INTRODUCTION

A recognized effect of radiation from flames is that substantial fractions of energy can be lost from the flame environment. In addition to radiative loading of enclosure walls, this energy loss leads to a temperature reduction and therefore changes in local gas density and flow velocity as well. In extreme cases, the reduction in flame velocity can lead to a substantial reduction in flame length. In addition, the temperature reduction affects flame chemistry due to the Arrhenius-exponential dependence on temperature. Errors in temperature could lead to substantial inaccuracies in calculating formation rates of nitric oxide, for example. While all of these effects can be expected to be most extreme in sooting flames, non-luminous gas band radiation can be important as well,¹ and the way in which one couples the radiation and flow calculations for quantitative assessment of these effects in plane-parallel or boundary layers of combustion gas products is the subject of this paper.

ANALYSIS

The coupling between radiation and flow occurs mathematically in the flow energy equation, and can be represented in all generality in the form

$$\frac{DH_0}{Dt} = -\frac{\partial q_i^R}{\partial x_i} \quad (1)$$

where DH_0/Dt is a generalized representation of the rate of change of total enthalpy (H_0) which can include convection, transport, and chemical enthalpy release, and $\partial q_i^R/\partial x_i$ is the divergence of the net radiative flux. From the equation of radiative transfer it is possible to show that

$$\frac{\partial q_i^R}{\partial x_i} = \int_0^\infty d\omega \int_{4\pi} d\Omega K_\omega(\omega) [I_b(\omega) - I(\Omega, \omega)]$$

$$I_b(\omega) = 1.1925 \times 10^{-5} \omega^3 / (\exp(1.438 \omega/T) - 1) \quad (\text{c.g.s.; } \omega \text{ in cm}^{-1}) \quad (2)$$

where K_ω is the local absorption coefficient, I_b is the local Planck body function, and I is the local radiative flux. The integrals over all frequencies and directions of radiation propagation (Ω) must be taken. In the optically thin limit, the second term can be neglected, and the isotropic source term is equivalent to

$$\left. \frac{\partial q_i^R}{\partial x_i} \right|_{\text{EMISS}} = 4\pi \int_0^\infty d\omega K_\omega(\omega) I_b(\omega). \quad (3)$$

Only frequency-integrated quantities are required, and thus wide-band models are used for the absorption bands of the species that are important in combustion product radiation (CO_2 , H_2O , and CO). In the wide-band formulation the local absorption coefficient for band j belonging to species i is represented by

$$K_a(\omega) = K_{aj}(\omega) = \frac{\alpha_{ij} \rho_i}{\Delta\omega_{ij}} \exp\left(\frac{-C_0 |\omega - \omega_{ij}^{(0)}|}{\Delta\omega_{ij}}\right) \quad (4)$$

where α_{ij} is the integrated band intensity [units: $\text{cm}^{-1}/(\text{g} \cdot \text{cm}^{-2})$], $\Delta\omega_{ij}$ is the band-width; ρ_i is the mass density of optically active chemical species i ; $\omega_{ij}^{(0)}$ is the band center; and $C_0 = 1$ or 2 depending on whether the band is one-sided or symmetric. With the assumption that I_b varies more slowly with frequency than the absorption bandshape, Eq.(3) can be simply expressed as:²

$$\left. \frac{\partial q_i^R}{\partial x_i} \right|_{\text{EMISS}} = 4\pi \sum_j \alpha_{ij} \rho_i I_{bj},$$

$$I_{bj} = I_b(\omega_{ij}^{(0)}, T), \quad (5)$$

and the summation is over all bands and species, and I_{bj} is the Planck function evaluated at the band center. Tabulations of the band model parameters for the important vibrational infrared (i.r.) and pure rotational transitions and the way in which one computes their temperature dependences are given in Refs. 3 and 4. We have nominally included in our model all 15 bands listed for H_2O , CO_2 , and CO . The optically thin or Planck limit expression given in Eq. (5) is convenient because it depends only on local parameters, and does not depend on having an optical field solution. The coupling between radiation and flow in counterflow diffusion flames has been examined in this emission-dominated limit in Refs. 5 and 6, and it has been found that radiation can severely depress peak temperatures and have a strong influence on NO_x production for low strain rates. However, very low strain rates correspond to thicker flames where optical thickness effects could become important, and the purpose of the rest of this paper is to derive an expression for the absorption term in Eq. (2) for plane parallel layers where all medium properties vary in one coordinate only, say y :

$$\left. \frac{\partial q_y^R}{\partial y} \right|_{\text{ABS}} = - \int_0^\infty d\omega \int_{4\pi} d\Omega K_a(\omega) I(\Omega, \omega). \quad (6)$$

The way in which this is done is to derive a solution for the frequency-dependent optical field, carry out the hemispherical average by interchanging orders of integration, and then perform the frequency integral in Eq. (6). The coordinate system employed is given in Fig. 1; a boundary layer problem in which medium properties vary only in the y -direction is assumed, and cold, black walls will also be assumed in the interests of simplicity. The effect of hot walls will be discussed later. It is convenient to carry out the calculation for a single band, and then sum over all bands/species at the end; a further approximation made here is to neglect band overlap effects which are usually relatively small. At a given depth y , the sum of the intensities with direction cosines μ and $-\mu$, respectively, can be formally represented by

$$I_{\mu}(\mu, \omega) + I_{\mu}(-\mu, \omega) = \int_{-\infty}^y I_b(y', \omega) \frac{d\tau_{\mu}}{d(y'/\mu)} \frac{dy'}{\mu} + \int_y^{\infty} I_b(y', \omega) \frac{-d\tau_{\mu}}{d(y'/\mu)} \frac{dy'}{\mu} \quad (7)$$

where τ_{μ} is the transmissivity given for wide-band models by

$$\tau_{\mu} = \exp\left(\frac{-R_{aj}(\omega) |y - y'|/\mu}{\sqrt{1 + \frac{R_{aj}(\omega) |y - y'|/\mu}{\beta_{ij} \rho_{e,i}}}}\right)$$

$$R_{aj}(\omega) = \frac{\bar{\alpha}_{ij} \bar{\rho}_i}{\Delta\bar{\omega}_{ij}} \exp\left(-C_0 \frac{|\omega - \omega_{ij}^{(0)}|}{\Delta\bar{\omega}_{ij}}\right) \quad (8)$$

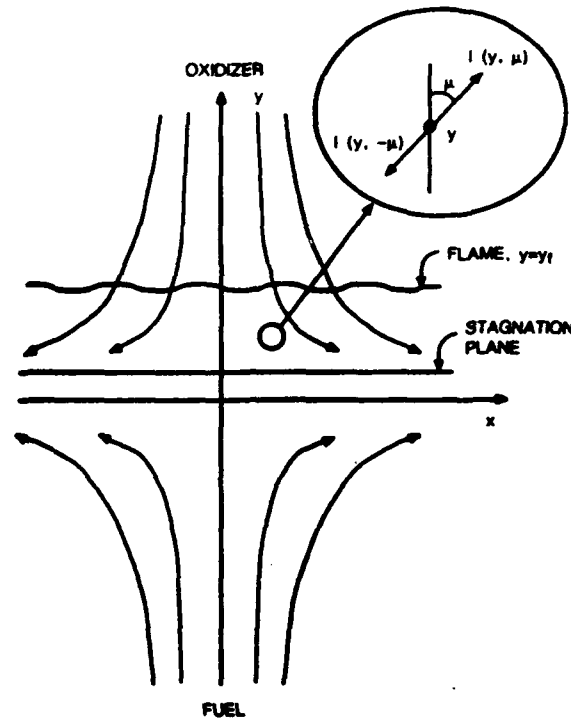


Fig. 1. Coordinate system for radiation analysis and opposed jet flame geometry.

where $\beta_{i,j}$ and $p_{e,i}$ are the equivalent line width parameter and equivalent broadening pressure for the band, respectively. The band model parameters are here represented by overbars to indicate that they are equivalent homogeneous path parameters whose method of calculation from mean properties will be discussed later. Modak⁷ has shown that it is a good approximation in flame calculations to assume the high broadening limit for which

$$\tau_y = \exp\left(-\bar{R}_{ay}(\omega) \frac{|y - y'|}{\mu}\right). \quad (9)$$

This approximation should be particularly good for the high-pressure, counterflow flame calculations to be given later. In this limit, Eq. (7) is

$$I(\mu, \omega) + I(-\mu, \omega) = \int_{-\infty}^{\infty} dy' I_b(y', \omega) \bar{R}_s(\omega) \exp(-\bar{R}_s(\omega) |y - y'|/\mu) dy'/\mu \quad (10)$$

where the ij subscripts have temporarily been suppressed in the interests of notational simplicity.

The orientation average in Eq. (6) is equivalent to the hemispherical average

$$\int_{4\pi} d\Omega [\text{Eq. (10)}] = 2\pi \int_0^1 d\mu [\text{Eq. (10)}]. \quad (11)$$

Performing this integration and making the transformation $z = \exp(-C_0|\omega - \omega^{(a)}|/\Delta\bar{\omega})$, for the frequency integration, Eq. (6) is equal to

$$-2\pi \frac{\alpha\rho}{\Delta\omega} \int_{-\infty}^{\infty} dy' I_b \bar{\alpha}\bar{\rho} \int_0^1 dz z^{(\Delta\bar{\omega}/\Delta\omega)} E_1\left(\frac{\bar{\alpha}\bar{\rho}}{\Delta\bar{\omega}} |y - y'|z\right) \quad (12)$$

where E_1 is the exponential integral and the slowly varying Planck function has been moved outside the z -integral. The z -integral is given by⁸

$$\left[\gamma(1 + \Delta\bar{\omega}/\Delta\omega, u)/u^{(1 + \Delta\bar{\omega}/\Delta\omega)} + E_1(u) \right] / \left(1 + \frac{\Delta\bar{\omega}}{\Delta\omega} \right) \quad (13)$$

where $u = \bar{\alpha}\bar{\rho}/\Delta\bar{\omega}|y - y'|$ is the band center optical depth and γ is the incomplete gamma function as given in Abramovitz and Stegun.⁹ It is more convenient to use the γ^* form given for which⁹

$$\gamma(1 + \Delta\bar{\omega}/\Delta\omega, u)/u^{(1 + \Delta\bar{\omega}/\Delta\omega)} = \Gamma(1 + \Delta\bar{\omega}/\Delta\omega)\gamma^*(1 + \Delta\bar{\omega}/\Delta\omega, u). \quad (14)$$

The function γ^* function can be efficiently calculated using the series representation of Ref. 9. Summing over all species and bands gives the final result for the net absorption of radiant energy by the medium

$$\left. \frac{\partial q_y^R}{\partial y} \right|_{\text{ABS}} = -2\pi \sum_{ij} \left(\frac{\alpha\rho}{\Delta\omega}(y) \right)_{ij} \int_{-\infty}^{\infty} dy' I_{by}(\bar{\alpha}\bar{\rho})_{ij} \times [\Gamma(1 + \Delta\bar{\omega}/\Delta\omega)\gamma^*(1 + \Delta\bar{\omega}/\Delta\omega, u) + E_1(u)]_{ij} (1 + \Delta\bar{\omega}/\Delta\omega)^{-1}_{ij} \quad (15)$$

where $u = u_{ij} = (\bar{\alpha}\bar{\rho}/\Delta\bar{\omega})_{ij}|y - y'|$.

The calculation of the equivalent homogeneous path band model parameters ($\bar{\alpha}$, $\bar{\rho}$, and $\Delta\bar{\omega}$) is based on the Curtis-Godson approximation as given by Felske and Tien.¹⁰ The temperature and species densities are simple path averages between point y and the point y' in the running integral; $\bar{\alpha} = \alpha(T)$, and $\Delta\bar{\omega} = \xi\Delta\omega(T)$, where ξ is a correction factor (Refs. 3 and 7) ranging from 1.0 to 1.44. The procedure for calculating ξ by bilinear interpolation based on the nominal, band-center optical depth u_{ij} and equivalent line width parameter $\beta(T)$ is given in Refs. 3 and 7. For the pure rotational band of H_2O the band model parameters of Ref. 11 are used; for this band, $\xi = 1$. The calculated results to follow were not particularly sensitive, however, to the inclusion of ξ .

An alternative form of Eq. (15) is derived by converting the integration over y' in Eq. (7) to an integration over τ . If one has medium properties on a grid of points denoted by the index l , Eq. (15) can be shown to be equivalent to

$$\left. \frac{\partial q_y^R}{\partial y} \right|_{\text{ABS}} = -2\pi \sum_{ij} \left(\frac{\alpha\rho}{\Delta\omega}(y) \right)_{ij} \sum_l \Delta\bar{\omega}_{ij}^{(l)} I_{by}^{(l)}(Y_{ij}(l_+ \rightarrow y) - Y_{ij}(l_- \rightarrow y)) - 2\pi \sum_{ij} \left(\frac{\alpha\rho}{\Delta\omega}(y) \right)_{ij} [\Delta\bar{\omega}_{ij}^{(1)} I_{by}(T_{w1})Y_{ij}(1 \rightarrow y) + \Delta\bar{\omega}_{ij}^{(2)} I_{by}(T_{w2})Y_{ij}(2 \rightarrow y)] \quad (16)$$

where

$$Y = \Gamma(\Delta\bar{\omega}/\Delta\omega)\gamma^*(\Delta\bar{\omega}/\Delta\omega, u) - \frac{u}{1 + \Delta\bar{\omega}/\Delta\omega} (E_1(u) + \Gamma(1 + \Delta\bar{\omega}/\Delta\omega)\gamma^*(1 + \Delta\bar{\omega}/\Delta\omega, u))$$

and it has been assumed that all path averages are taken from point y to the grid midpoints, and that $\Delta\omega$ and I_b are evaluated at the midpoints. The functions $Y_{ij}(l_+ \rightarrow y)$ and $Y_{ij}(l_- \rightarrow y)$ are based on which of the grid point pairs is closest to and farthest from y , respectively. The effect of absorption of hot, black wall radiation has been introduced in the terms involving the wall temperatures T_{w1} and T_{w2} ; it is understood that the path-averaged properties which go into $\Delta\bar{\omega}$ and Y in these terms are those along the paths from each wall to point y .

Equations (15) and (16) can be time-consuming to use because of the running integrals that must be evaluated for each point y . The "analytic" approximation of Modak⁷ provides increased efficiency and reasonable accuracy when the radiating species are concentrated in a high temperature reaction sheet as encountered in diffusion flames. Returning to Eq. (7), it is reasoned that most of the contribution to the integrals will come from regions near the maximum flame temperature because of the rapid variation of I_b with temperature. The transmissivity derivatives will be more slowly varying, and can be factored out, assigned their values at $y = y_t$, the point of maximum flame temperature. This gives, for cold, black walls:

$$\left. \frac{\partial q_y^R}{\partial y} \right|_{\text{ABS}} = -2\pi \sum_{ij} \left(\frac{\alpha\rho}{\Delta\omega}(y) \right)_{ij} \times \left[\frac{\bar{\alpha}\bar{\rho}}{1 + \Delta\bar{\omega}/\Delta\omega} (\Gamma(1 + \Delta\bar{\omega}/\Delta\omega)\gamma^*(1 + \Delta\bar{\omega}/\Delta\omega, u) + E_1(u)) \right]_{ij, y=y_t} \int dy' I_{by}, \quad (17)$$

where

$$\int dy' I_{bij} = \begin{cases} \int_{-\infty}^y dy' I_{bij} & \text{for } y > y_f, \\ \int_y^{\infty} dy' I_{bij} & \text{for } y < y_f, \end{cases}$$

and the property averages are calculated between y and y_f . Equation (17) gives results nearly equivalent to Eqs. (15) and (16) with much increased efficiency, subject to one restriction that will be discussed in the next section. Absorption of hot wall emission can be represented by the same terms as in Eq. (11). These experiments are not limited to slowly varying medium properties per se, but would presumably have the inherent limitations of the Curtis-Godson approximation in this regard.

SAMPLE CALCULATED RESULTS

Example calculations have been done for an opposed jet diffusion flame, as illustrated in Fig. 1. The configuration consists of two opposed fuel and oxidizer jets, and is known to lead to a one-dimensional structure normal to the surface of the stoichiometric mixture. In a small region near the stagnation streamline, temperature and species concentrations are nearly one-dimensional. Temperature and radiating species concentrations have been computed using a counterflow flame code developed by Smooke.¹² The calculations are described in more detail in Ref. 13, where they formed the basis for a flamelet approach to predicting NO_x concentrations in an aircraft gas turbine combustor. The pressure is 10.5 atm, and the fuel temperature has been chosen to give an adiabatic flame temperature approximating that of jet fuel. The temperature and radiating species profiles are shown in Figs. 2 and 3 for the base case used in these calculations. The latter corresponded to that flamelet in the calculations of Ref. 13 having the lowest value of strain rate. The strain rate, denoted by the symbol a , is the gradient of the velocity normal to the flame structure, and is a measure of the rate at which reaction products are pulled away in a direction parallel to the reaction sheet. In the base case shown in Figs. 2 and 3, it has the value 56.1 sec^{-1} . To investigate optical thickness effects, thicker flamelets corresponding to lower strain rates were synthetically generated by simply stretching the coordinates of the base case by various factors. At the low strain rates, the species profiles correspond nearly to equilibrium values, and it is felt that this approximate procedure will be adequate for illustrative purposes, rather than using the Ref. 12 code to get the exact solution. Characteristic dimension will scale with strain rate approximately as $a^{-1/2}$.¹⁴ No coupling between radiation and the flame solution is accounted for here; the energy equation in the counterflow solver omits the radiative source term.

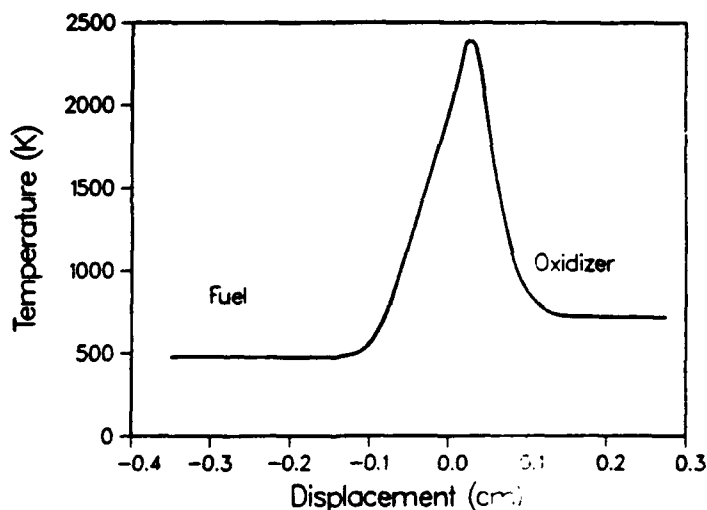


Fig. 2. Temperature distribution for base case. Strain rate is 56.1 sec^{-1} .

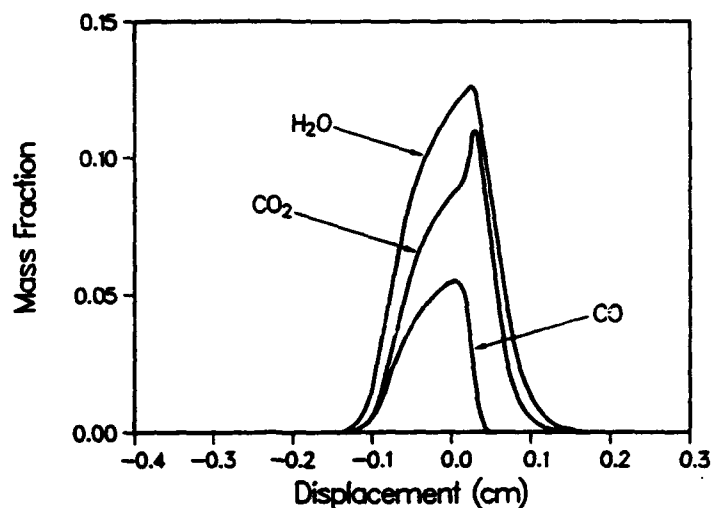


Fig. 3. Radiating species profiles of base opposed jet case.

Figure 4 shows the total divergence of the radiative flux as a function of position. The position is presented in normalized form to correspond to the coordinates of the base case. For the latter, both the optically thin and thickness-corrected solutions are given. Thickness corrections are seen to be starting to be important for this case. Two other thickness-corrected solutions are given for coordinate stretchings of 10 and 25 which correspond to strain rates of 0.56 and 0.09 sec^{-1} , respectively. It can be seen that thickness corrections are certainly important for strain rates somewhat lower than 56.1 sec^{-1} . It is in this range that significant temperature reductions relative to the adiabatic case are predicted with optically thin analysis.⁵ Optical thickness effects will cause the temperature reductions to vary somewhat less dramatically with decreasing strain rate. Note that there is a small net absorption in the relatively cold combustion product regions at the edges of the flame sheet. In a future publication the results of incorporating the analysis presented here into the counterflow flame solver and assessing the impact of radiative loss on NO_x levels will be addressed, and it will be shown that very precise predictions require thickness corrections for low strain rates.¹⁵ In these calculations the water pure rotational band was left out; it was found that with it the factorization analytic expression [Eq. (17)] lost accuracy. Equation (5) is also not accurate for this band. Differences of a few percent were found using the exact solution [Eq. (16)] with and without this band.

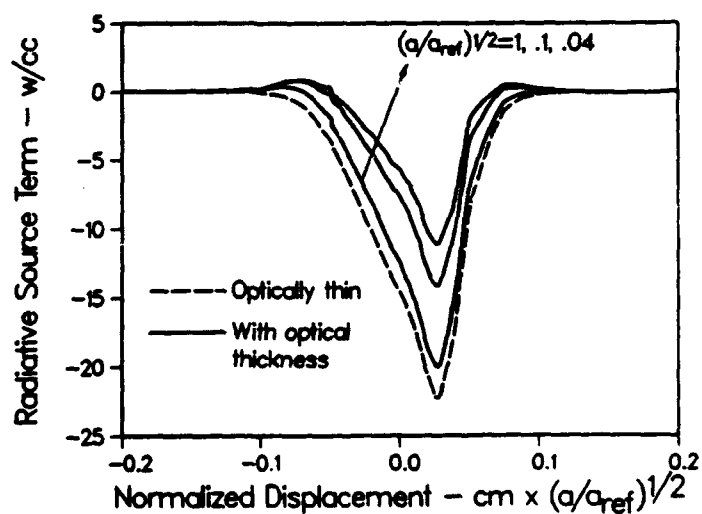


Fig. 4. Radiation source term (divergence of net radiative flux) as function of strain rate.

Acknowledgements—The author would like to thank J. De Ris for early conversations about wide-band models, to L. Chiapetta for providing him with a program to calculate the wide-band model parameters, and to A. Vranos for providing the counterflow solutions on which the radiation model was tested. This research was funded by AFOSR Contract F49620-91-C-0056.

REFERENCES

1. D. K. Edwards and A. Balakrishnan, *Combust. Flame* **20**, 401 (1973).
2. M. M. Abu-Romia and C. L. Tien, *J. Heat Transfer* **89**, 321 (1967).
3. D. K. Edwards and A. Balakrishnan, *Int. J. Heat Mass Transfer* **16**, 25 (1973).
4. D. K. Edwards, in *Handbook of Heat Transfer Fundamentals*, Chap. 14, Pt 4, W. M. Rosenhow, J. P. Hartnett, and E. N. Ganic eds., McGraw-Hill, New York, NY (1985).
5. Y. Liu and B. Rogg, "Modelling of Thermally Radiating Diffusion Flames with Detailed Chemistry and Transport", *Proceedings of the Eurotherm Seminar No. 17, Heat Transfer in Radiating and Combusting Systems*, pp. 114-127 (1990).
6. U. C. Muller, F. Maus, and N. Peters, "Influence of Radiative Heat Loss on Thermal NO-Production in Laminar CO-H₂-N₂-Diffusion Flames", poster presentation at *Twenty-first Symposium (International) on Combustion*, Orleans, France (1986).
7. A. T. Modak, "Nonluminous Radiation from Hydrocarbon-Air Diffusion Flames", Factory Mutual Research Technical Rep. 22355-1 (1974).
8. M. Geller, "Tables of Integrals Involving Powers, Exponentials, Logarithms, and the Exponential Integral", Cal. Tech. Jet Propulsion Lab. Rep. 32-469 (1963).
9. M. Abramowitz and I. A. Stegun eds., *Handbook of Mathematical Functions*, Chap. 6, Dover, New York, NY (1970).
10. J. D. Felske and C. L. Tien, *JQSRT* **14**, 35 (1974).
11. A. T. Modak, *JQSRT* **21**, 131 (1979).
12. M. D. Smooke, I. K. Puri, and K. Seshadri, "A Comparison Between Numerical Calculations and Experimental Measurements of the Structure of a Counterflow Diffusion Flame Burning Diluted Methane in Diluted Air", *Twenty-first Symposium (International) on Combustion*, The Combustion Institute, pp. 1783-1792 (1986).
13. A. Vranos, *Combust. Sci Technol.* **84**, 323 (1992).
14. R. Borghi, *Prog. Energy Combust. Sci.* **14**, 245 (1988).
15. A. Vranos and R. J. Hall, *Combust. Flame* in press (1993).

Appendix E

Radiative Dissipation in Planar Gas-Soot Mixtures

Radiative Dissipation in Planar Gas-Soot Mixtures

by

Robert J. Hall
United Technologies Research Center
East Hartford, Conn.

Abstract

The coupling of flame radiation and flow is a subject of renewed interest, with an acceptance of the fact that reacting flow models are not complete without radiation effects. The interest goes beyond the ability to predict heat transfer to enclosure walls. It is known, for example, that substantial fractions of flame energy can be converted to radiation (Ref. 1), and that the gas cooling resulting from this non-adiabatic loss can affect flame chemistry, leading to inaccuracies in prediction of pollutants like nitric oxide. Neglect of radiation in flame hydrodynamic simulations can also lead to large errors in flow velocity and flame length. These effects are expected to be most extreme in sooting flames, but both gas and soot radiation have to be included in the most general model. Quantitative assessment of these effects requires inclusion of an energy sink term in the flow energy equation. This sink term, the divergence of the net radiative flux, is the difference of an emission term valid in the optically thin limit, and a self-absorption term that becomes important when optical thickness effects need to be accounted for. The expression for the emission term is generally trivial even when both soot and gas band radiation are present, and does not depend on flame geometry because only local properties are required. The self-absorption term is more difficult because a solution for the radiative flux is implicitly required, and integrations over all frequencies and flux propagation directions are required. This term is complicated further when both soot and gas radiators are present because of absorption profile overlaps; the broadband soot absorption and emission profile will overlap those of the relatively narrowband molecular resonances. In this paper, a complete solution for the radiative dissipation is given for the one-dimensional, plane-parallel, or boundary layer flow problem. Both gas band and soot radiation are considered, and the resulting solution is valid for all degrees of optical thickness. The expression is given in semi-analytic form in terms of single quadratures normal to the flame structure. The theory will be illustrated by example calculations for a model, high pressure, sooting counterflow diffusion flame. Other applications might include fire radiation from smoke layers (Ref. 2), and two-dimensional, turbulent-jet diffusion flames in the boundary layer approximation (Ref. 3).

Analysis

The main features of the theoretical analysis are as follows. The absorption terms are derived by taking hemispherical averages of frequency-dependent solutions of the equation of radiative transfer, and integrating them over the absorption bandshapes of both the molecules and the soot. The soot absorption coefficient is assumed to have the Rayleigh form, with scattering ignored. For nonuniform paths, the soot terms can be derived without approximation; for the gas band terms a form of the mean properties assumption is employed. The gas absorption profiles are assumed to have the wideband model form, and the transmissivities are appropriate to the high pressure-broadening limit. More specifically,

1. It is assumed that the molecular absorption bandshapes are described by wideband models

for which (Ref.4) the absorption profile is given by

$$K_{ij}(\omega) = \frac{\alpha_{ij} \rho_i}{\Delta \omega_{ij}} \exp \left(\frac{-c_0 |\omega - \omega_{ij}^{(0)}|}{\Delta \omega_{ij}} \right) \quad (1)$$

where α_{ij} is the integrated band intensity of the j th resonance of radiating species i (H_2O , CO_2 , CO); ρ_i is its mass density; $\Delta \omega_{ij}$ is the bandwidth of the resonance, and $\omega_{ij}^{(0)}$ its band center frequency. $c_0 = 1$ or 2 depending on whether the band is symmetric or one-sided. It will further be assumed that the absorption profiles vary much more rapidly with frequency than other characteristic functions such as Planck function or soot absorption coefficient, so that

$$c_0 \Delta \omega_{ij}^{-1} \int_0^\infty d\omega \exp \left(\frac{-c_0 |\omega - \omega_{ij}^{(0)}|}{\Delta \omega_{ij}} \right) f(\omega) = f(\omega_{ij}^{(0)}) \quad (2)$$

The molecular transmissivity τ is taken to have the form appropriate to the high pressure-broadening limit for which the integrated absorbance $A_{ij} = \int d\omega (1 - \tau_{ij})$ has the form (Ref. 5)

$$\frac{A(a_{ij})}{\Delta \omega_{ij}} = E_1(a_{ij}) + \ln(a_{ij}) + \gamma \quad (3)$$

where

$$a_{ij} = \frac{\alpha_{ij} \rho_i}{\Delta \omega_{ij}} y$$

y being the optical path length, E_1 the exponential integral, and γ the Euler-Mascheroni constant. Its derivative with respect to y is thus

$$\frac{dA_{ij}}{dy} = \Delta \omega_{ij} (1 - e^{-a_{ij}})/y \quad (4)$$

The suitability of this approximation for combustion radiation calculations has been discussed in Ref. 5. It has been found to give good agreement in most cases with more elaborate calculations based on narrowband models even at one atmosphere. Many of the interesting applications will be for high pressure systems, and the approximation should be particularly good for these. For non-homogeneous optical paths, evaluation of the band parameters which appear in Eqs. 3 & 4, are based on simple, path-averaged temperature and density (Refs. 5, 6). Overlaps between molecular bands are ignored, but the overlaps between the relatively narrow molecular resonances and the broadband soot absorption-emission profile are included. It will further be assumed that the transmissivity at any frequency will be given by the product of the gas and soot transmissivities, e.g. $\tau(\omega) = \tau_s(\omega)\tau_{ij}(\omega)$

2. The soot absorption coefficient is taken to have the form appropriate to Rayleigh spheroids

$$K_{ns}(\omega) = c_s \omega f_v \quad (5)$$

where f_v is the particulate volume fraction, the frequency in units cm^{-1} , and the constant c_s taken to be independent of frequency. This is equivalent to neglecting the soot index of refraction. The

Rayleigh form of the absorption coefficient is suitable to first order for aggregate chains of spheroids as well (Ref. 7). Light scattering by soot is assumed to be small.

The generalized form of the radiative source term is given by the double integral over wavelength and direction

$$\int_0^\infty d\omega \int_{4\pi} d\bar{\Omega} K_a(\omega) [I_b(\omega) - I(\bar{\Omega}, \omega)] = Q_{\text{emiss}} - Q_{\text{abs}} \quad (6)$$

where I_b is the Planck function, $I(\bar{\Omega}, \omega)$ is the radiation intensity, and $K_a(\omega) = K_{\text{as}}(\omega) + \sum_{ij} K_{\text{aij}}(\omega)$. Consistent with the above assumptions, the first term in Eq. 6 (emission) can be simply expressed as (Refs. 8, 9)

$$4\pi \sum_{ij} \alpha_{ij} \rho_i I_{bij} + 4\pi c_2^{-5} c_1 \int_0^\infty \frac{u^4 du}{e^u - 1} c_s f_v T^5 \quad (7)$$

where the factorization assumption, Eq. (2), has been used for the molecular resonances ij , the soot index dispersion has been ignored as mentioned in the soot part, and c_1 and c_2 are constants in the Planck function

$$I_b(y, \omega) = c_1 \omega^3 / (\exp(\frac{c_2 \omega}{T(y)}) - 1) \quad (8)$$

Thus

$$\begin{aligned} I_{bij} &= c_1 (\omega_{ij}^{(0)})^3 (\exp(c_2 \omega_{ij}^{(0)} / T) - 1)^{-1} \\ &= c_1 (\omega_{ij}^{(0)})^3 \sum_{n=1}^{\infty} \exp(-nc_2 \omega_{ij}^{(0)} / T) \end{aligned} \quad (9)$$

In the absorptive analysis, one molecular resonance ij will be assumed to simplify the notation, and a sum over all ij performed at the end. The radiation field solution is required as a function of frequency and flux propagation direction to calculate the self-absorption part. Referring to Figure 1, the sum of the intensities with direction cosines μ and $-\mu$ with respect to the axis y normal to the flame structure can be formally represented as

$$I(\mu, \omega) + I(-\mu, \omega) = \int_{-\infty}^y I_b(y', \omega) \frac{dr}{d(y'/\mu)} \frac{dy'}{\mu} + \int_y^\infty I_b(y', \mu) \frac{-dr}{d(y'/\mu)} \frac{dy'}{\mu} \quad (10)$$

The absorption part will thus have terms proportional to $K_{\text{aij}} \tau_s \frac{dr_{ij}}{d(y'/\mu)}$, $K_{\text{aij}} \tau_{ij} \frac{dr}{d(y'/\mu)}$, $K_{\text{as}} \tau_s \frac{dr_{ij}}{d(y'/\mu)}$, and $K_{\text{as}} \tau_{ij} \frac{dr}{d(y'/\mu)}$. These represent, respectively, gas absorption of gas emission, gas absorption of soot emission, soot absorption of gas emission, and soot absorption of soot emission. Thus $Q_{\text{abs}} = Q_{\text{gs}} + Q_{\text{gs}} + Q_{\text{sg}} + Q_{\text{ss}}$. Since the gas and soot transmissivities have the form, respectively,

$$r_{ij}(\omega) = \exp(-\bar{K}_{a_{ij}}(\omega)|y - y'|/\mu) = \exp(-az/\mu) \quad (11)$$

$$r_s(\omega) = \exp(-c_s \omega \bar{f}_v(y; y') |y - y'|/\mu) = \exp(-b/\mu) \quad (12)$$

where

$$\begin{aligned} a &= a_{ij} = \frac{\bar{\alpha}_{ij} \bar{\rho}_i}{\Delta \bar{\omega}_{ij}} |y - y'| \\ z &= z_{ij} = \exp(-c_o |\omega - \omega_{ij}^{(0)}| / \Delta \bar{\omega}_{ij}) \\ b &= b_{ij} = c_s \omega_{ij}^{(0)} \bar{f}_v(y; y') |y - y'| \\ \bar{f}_v(y, y') &= |y - y'|^{-1} \left| \int_{y'}^y f_v(y'') dy'' \right| \end{aligned}$$

all of the terms contributing to Q_{abs} will be proportional to

$$\exp(-(az + b)/\mu) \quad (13)$$

The overbars in Eqs. 11, 12 denote path-averaged quantities as per Refs. 5, 6. The average over all directions of propagation is given by the hemispheric integrals

$$\int_{4\pi} d\bar{\Omega} |I(\omega, \bar{\Omega})| = 2\pi \int_0^1 d\mu [\text{Eq. 10}] \quad (14)$$

Thus, the exponential integral E_1 will be a factor in all terms from the relation

$$2\pi \int_0^1 \exp(-(az + b)/\mu) \frac{d\mu}{\mu} = 2\pi E_1(az + b) \quad (15)$$

The frequency integrations are generally carried out using $\int_0^\infty d\omega \rightarrow \frac{\Delta \omega}{c_o} \int_0^1 \frac{dz}{z}$.

Starting from the assumed forms for the absorption coefficients and transmissivities, and making use of the foregoing assumptions, the following expressions for the terms contributing to the absorption part are derived.

$$Q_{gs} = 2\pi \sum_{ij} \left(\frac{\alpha \rho}{\Delta \omega} \right)_{ij} \int_{-\infty}^{\infty} dy' I_{bij}(y') (\bar{\alpha \rho})_{ij} U\left(\frac{\Delta \omega}{\Delta \omega}, a, b\right) \quad (16)$$

$$Q_{gs} = 2\pi c_s \sum_{ij} \omega_{ij}^{(0)} \left(\frac{\alpha \rho}{\Delta \omega} \right)_{ij} \int_{-\infty}^{\infty} dy' f_v(y') \Delta \bar{\omega}_{ij}(y') I_{bij}(y') U\left(\frac{\Delta \omega}{\Delta \omega} - 1, a, b\right) \quad (17)$$

$$Q_{sg} = 2\pi c_s f_v(y) \sum_{ij} \omega_{ij}^{(0)} \int_{-\infty}^{\infty} dy' \Delta \bar{\omega}_{ij}(y') I_{bij}(y') |y - y'|^{-1} [E_2(b) - E_2(a + b)] \quad (18)$$

where $a=a_{ij}$ and $b=b_{ij}$ are as given in Eqs. 11, 12, E_2 is the exponential integral of second order, and

$$\begin{aligned} Q_{ss} &= 2\pi c_s^2 c_1 f_v(y) \int_{-\infty}^{\infty} dy' f_v(y') \int_0^{\infty} d\omega \omega^5 \sum_{n=1}^{\infty} e^{-nc_2\omega/T(y')} E_1(az(\omega) + c_s \omega \bar{f}_v |y - y'|) \\ &= 2\pi c_s^2 c_1 f_v(y) \frac{5!}{(c_2)^6} \int_{-\infty}^{\infty} dy' f_v(y') T^6(y') \sum_{n=1}^{\infty} n^{-6} \\ &\quad \cdot \left[\ln \left(1 + \frac{P_n(y')}{Q(y')} \right) - \sum_{k=1}^5 \frac{1}{k} \left(\frac{P_n(y')}{P_n(y') + Q(y')} \right)^k \right] \end{aligned} \quad (19)$$

$$\begin{aligned} &-2\pi c_s^2 c_1 f_v(y) \sum_{ij} (\omega_{ij}^{(0)})^5 \int_{-\infty}^{\infty} dy' f_v(y') \Delta \bar{\omega}_{ij}(y') \sum_{n'=1}^{\infty} e^{-n'c_2\omega_{ij}^{(0)}/T(y')} \\ &\quad \cdot (E_1(a + b) - E_1(b)) \end{aligned}$$

with

$$\begin{aligned} P_n(y') &= nc_2/T(y') \\ Q(y') &= c_s \bar{f}_v |y - y'| \end{aligned}$$

Q_{gg} and Q_{sg} both require the integral

$$U(p, a, b) = \int_0^1 dz z^p E_1(az + b) \quad (20)$$

Series expansions for this integral are given in the Appendix. The two terms for Q_{ss} , representing the pure soot absorption plus a correction for gas attenuation, respectively, are derived by setting

$$E_1(az + b) = E_1(b) + [E_1(az + b) - E_1(b)] \quad (21)$$

and assuming that

$$\int d\omega [E_1(az + b) - E_1(b)] \simeq \sum_{ij} \Delta \bar{\omega}_{ij} (E_1(a + b) - E_1(b)) \quad (22)$$

where again a and b are as in Eqs. 11, 12. Aside from the factorization assumption of Eq. 2, Eq. 22 is the only mathematical approximation made. It is possible to derive an exact series representation of this term for $b > a$ which confirms the validity of this approximation.

Thus all terms contributing to field absorption are expressed in semi-analytic form in terms of single integrals over the coordinate normal to the flame structure. These running integrals are, however a computational burden. The economy of the calculation is improved by restricting attention to the strongest molecular lines (H_2O 6.3 and 2.7 micron, CO_2 4.3 and 2.7 micron, CO 2.35 micron), which account for most of the radiation. Limiting the terms in the Planck function expansion Eq.(9) to $n=2$ is usually an adequate approximation at high temperature as well. This type of analysis does not lend itself to inclusion of non- black wall boundary conditions. For black walls, however, additional terms in the expression for the absorption can be calculated. As an example, for a single wall at temperature T_w , the following term is added to the absorption expression for the pure soot case

$$2\pi c_1 c_s f_v(y) 4! \sum_{n=1}^{\infty} \{ (P_{nw} + Q_w)^{-5} - 5Q_w/P_{nw}^6 \cdot [\ln(1 + P_{nw}/Q_w) - \sum_{k=1}^5 \frac{1}{k} (\frac{P_{nw}}{P_{nw} + Q_n})^k] \} \quad (23)$$

where

$$P_{nw} = nc_2/T_w$$

$$Q_w = c_s \bar{f}_v |y - y_w|$$

The net radiative flux to the wall is, for pure soot,

$$q_R = 2\pi c_s c_1 \int_{-\infty}^{y_w} dy' \int_0^{\infty} d\omega \omega^4 \sum_{n=1}^{\infty} e^{\frac{-nc_2^2}{T(y')^2}} E_2(c_s \omega \bar{f}_v |y' - y_w|) f_v(y')$$

$$= 2\pi c_s c_1 \int_{-\infty}^{y_w} dy' f_v(y') \sum_{n=1}^{\infty} \left\{ \frac{4!}{(P_n(y') + Q(y'))^5} - \frac{5! Q(y')}{P_n(y')^6} \cdot \left[\ln(1 + \frac{P_n(y')}{Q(y')}) - \sum_{k=1}^5 \frac{1}{k} \left(\frac{P_n(y')}{P_n(y') + Q(y')} \right)^k \right] \right\} \quad (24)$$

where

$$P_n(y') = nc_2/T(y')$$

$$Q(y') = c_s \bar{f}_v |y' - y_w|$$

Corrections to Eqs. 23 and 24 for attenuation by gas band absorption would be derived by proceeding as in Eqs. 21 and 22, but with E_1 replaced by E_2 .

The gas band contributions to net radiative wall flux may be expressed as

$$q_R = 2\pi \sum_{ij} \int_{-\infty}^{y_w} dy' I_{bij}(y') \bar{\Delta\omega}_{ij}(y') |y_w - y'|^{-1} [E_3(b) - E_3(a+b)] \quad (25)$$

Sample Calculated Results

Sample calculations have been performed for a model opposed jet diffusion flame as shown in Figure 1. The configuration consists of two opposed fuel and oxidizer jets, leading to a one-dimensional structure in a region near the stagnation streamline where application of this one-dimension radiation analysis is appropriate. Methane fuel has been assumed, and the flame properties were calculated using a widely used opposed jet solver (Ref.10). The flame was modified by adding the expression for the radiative source term derived here to the one-dimensional energy equation. The clean flame calculations are described in more detail in Ref. 11, where they formed the basis for a flamelet approach to predicting NO_x concentrations in an aircraft gas turbine combustor. The fuel temperature was adjusted to give a peak flame temperature approximating that of jet fuel, and the pressure of 10.5 atm is representative of such a combustor at the cruise condition. In order to assess the possible role of soot in the radiative transfer, a sooting region has been synthetically added to the clean flame solution as shown in Figures 1 & 2. Soot will tend to form on the fuel side of the flame, and will build up at the stagnation plane due to thermophoretic transport (Refs.12, 13). Calculation of the actual soot profile of course requires a soot kinetics and transport model, but this was not available for this study. Thus, a simple picture of the soot profile is assumed in which it has been assumed to be uniformly distributed between the stagnation plane and a point on the fuel side where nucleation might be expected to be intense. Following Ref. 14, we assume that nucleation will occur at an elemental carbon mixture fraction of .1, where the adiabatic temperature is about 1675 K. This results in the soot profile located shown in Figure 2; the effective radiation temperature of the soot is about 1550K, nearly 900 K lower than the peak gas temperature. The average soot volume fraction is then treated parametrically. The synthetic nature of this calculation must be emphasized; with methane fuel at this temperature the flame in reality would be expected to be relatively clean. The intent here is to gain some idea of the relative importance between soot and gas band radiation for reasonable ranges of the soot volume fraction. The soot is coupled to the flame solution only through temperature reduction resulting from the radiation; in reality the gas cooling due to radiation could affect the pyrolysis, nucleation, and surface growth processes that grow the soot. An accurate treatment of this problem requires that temperature-dependent soot growth processes be added to the chemical kinetics mechanism. The basic gas kinetics mechanism used here, where the effect of radiation on NO concentration is of interest, is a variation of that proposed by Glarborg, et. al., (Ref. 15). The 213 reactions and 57 species of that mechanism have been culled to 126 and 30, respectively. The data set is limited to C1 chemistry, and NO₂ kinetics have been ignored.

Opposed jet solutions are characterized by the strain rate (denoted here by the symbol a), which is a measure of the velocity gradient normal to the flame structure. It is an indication of how fast reaction products are pulled away in the direction parallel to the flame sheet. High values of strain rate correspond to short gas residence times, thinner flame structures, and somewhat lower peak temperatures, leading to reduced importance of radiation. Low values of strain rate are characterized by the opposite attributes, and it will consequently be these that are examined here. In particular, a base case value of 20 sec^{-1} is used for this study; the adiabatic temperature profile is that shown in Figure 2. For low values of strain rate chemical equilibrium radiating species profiles will be a reasonable approximation, and lower values of strain rate can be simulated by stretching the coordinates in proportion to $a^{-1/2}$. Figures 3 and 4 are based on fixing the adiabatic solution for $a = 20 \text{ sec}^{-1}$, stretching the coordinates in this way, and calculating the radiative dissipation according to Equations 7 and 16-19. Figure 3 shows how calculated absorption and emission vary with strain rate for a clean flame condition. It can be seen that optical thickness effects are important even for the $a = 20 \text{ sec}^{-1}$ case, where the characteristic flame thickness is

about 1-2 mm. Figure 4 shows the analogous results for a sooting flame where a soot volume fraction of $10^{(-5)}$ has been assumed. At this value of volume fraction, the soot contributions start to dominate the radiation process at this pressure.

Inclusion of Equations 7 and 16-19 as a power sink term in the energy equation of the opposed jet solver leads to the predicted variation of radiative loss fraction with soot volume fraction shown in Figure 5. As stated, soot radiation starts to dominate for volume fractions in excess of about $10^{(-5)}$, with predicted loss fractions rising to about 20% for the highest values of volume fraction that could be reasonably expected. Soot self-absorption becomes important at the highest volume fraction. Radiative loss fraction is here defined as the volume integrated net radiative power density divided by the volume integrated chemical enthalpy release rate. These curves are of course highly sensitive to the assumed thickness and effective radiation temperature of the soot zone. Calculations at other values of strain rate are qualitatively similar, with the overall radiative loss fraction decreasing with increasing strain rate.

The gas cooling effects resulting from the radiative loss are shown in Figure 6. The percentage decrease in flame temperature will generally be much less than the radiative loss percentage because the heat capacity is non-linear, and because reductions in temperature will be offset to some extent by recombination of radicals. In the case of soot radiation, the soot will be radiating from a lower temperature region, and the effect on the temperature there is shown in Figure 6 for the maximum value of volume fraction considered. Cooling of the flame zone will then occur by thermal conduction; the percentage reduction in peak flame temperature is far less than the 20% radiative loss fraction for this case. As stated, however, the temperature reductions in the soot zone are probably large enough to affect the soot growth processes, leading to a complicated coupling between radiation and growth.

The effect of these temperature reductions on the profiles of NO is shown in Figure 7. The profile resulting from the soot radiative losses can be contrasted with that resulting from assuming a local non-adiabatic loss that is everywhere 20% of the local enthalpy release rate. Because the main effect of the soot is to cool regions where the NO is not at its peak levels, soot radiation has a much smaller effect on NO reduction in these flames.

Appendix

The integral

$$U(p, a, b) = \int_0^1 dz z^p E_1(az + b) = \int_0^1 dz z^p \int_1^\infty dt \frac{e^{(-az+b)t}}{t} \quad (A1)$$

has the following series representations

$$\begin{aligned} \int_0^1 dz z^p E_1(az + b) &= E_1(a + b)/(p + 1) & (p > -1) \\ e^{-(a+b)} \sum_1^\infty \left(\frac{a}{a+b}\right)^n \frac{\alpha_{n-1}(a+b)}{(p+1)_{n+1}} & & (b > a) \\ \frac{e^{-b}\Gamma(p+1)\gamma^*(p+1, a)}{(p+1)} - \frac{e^{-(a+b)}}{(p+1)} \left(\frac{b}{b+a}\right) \sum_1^\infty \left(\frac{a}{a+b}\right)^n \frac{\alpha_n(a+b)}{(p+1)_{n+1}} & & (b < a) \end{aligned} \quad (A2)$$

where

$$\begin{aligned} (u)_{n+1} &= \Gamma(u + n + 1)/\Gamma(u) \\ \alpha_n(u) &= n!(1 + u + u^2/2! + \dots + u^n/n!) \end{aligned}$$

and Γ and γ^* are the gamma function and a form of the usual incomplete gamma function, γ , respectively.

The first series is derived by performing the z -integration in Eq. A1 first, yielding (Ref. 16)

$$\int_0^1 dz z^p e^{-azt} = A_1(p, at, 1) = \frac{\gamma(p+1, at)}{(at)^{p+1}} \quad (A3)$$

γ is now expanded in a power series (Ref. 17), and the t -integral is done term-by-term. The second series is derived by using Eq. A3 and integration by parts, followed by term-by-term integration over t .

Figure Captions

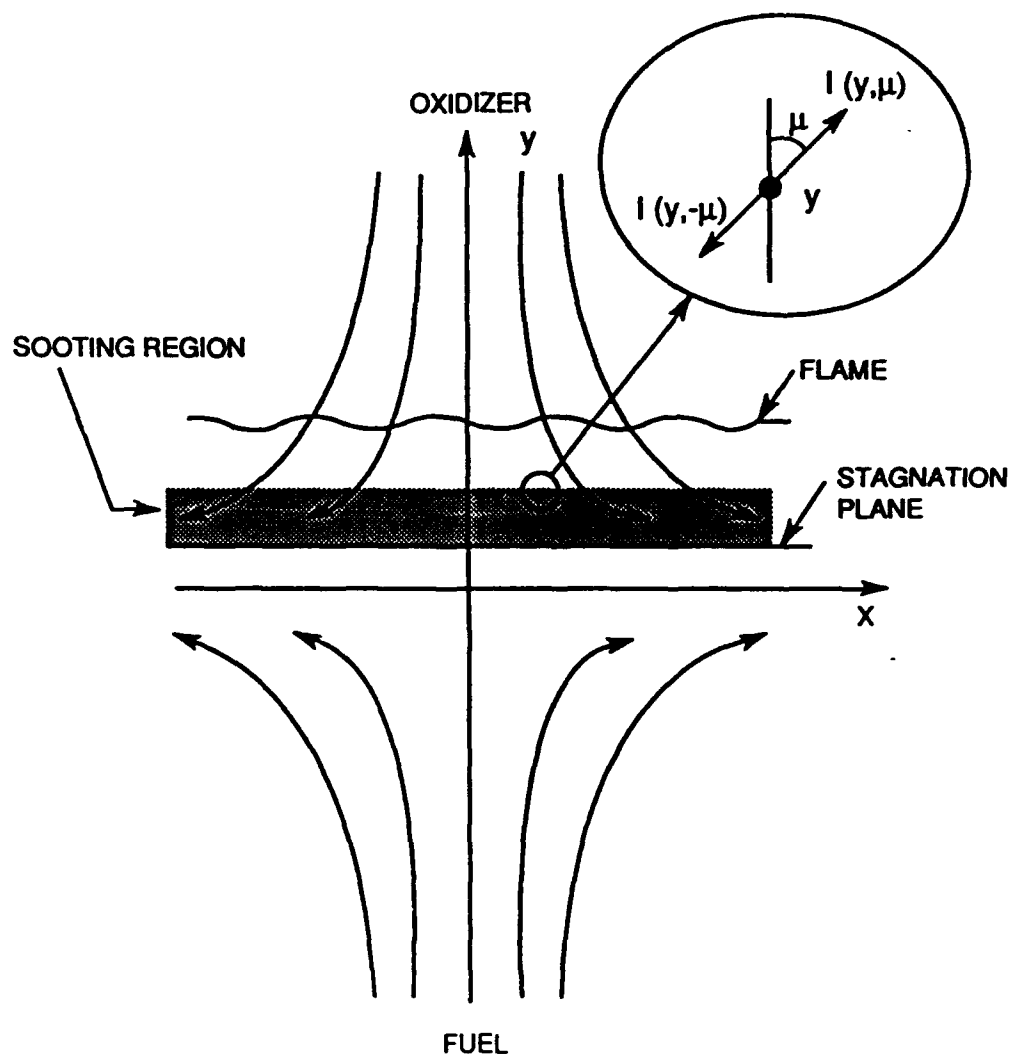
- Figure 1. Coordinate system for radiation analysis and opposed jet flame geometry.
- Figure 2. Adiabatic temperature profile in model opposed jet and assumed location of sooting region. Strain rate = 20 sec^{-1} .
- Figure 3. Variation of radiative dissipation profiles with strain rate for non-sooting case.
- Figure 4. Variation of radiative dissipation profiles with strain rate for soot loading of $10^{(-5)}$.
- Figure 5. Variation of predicted radiative loss fraction with soot loading for optically thin and thickness-corrected cases.
- Figure 6. Temperature profiles for adiabatic, gas band radiation, and gas band plus soot radiation.
- Figure 7. Predicted effect of radiative cooling on NO profiles.

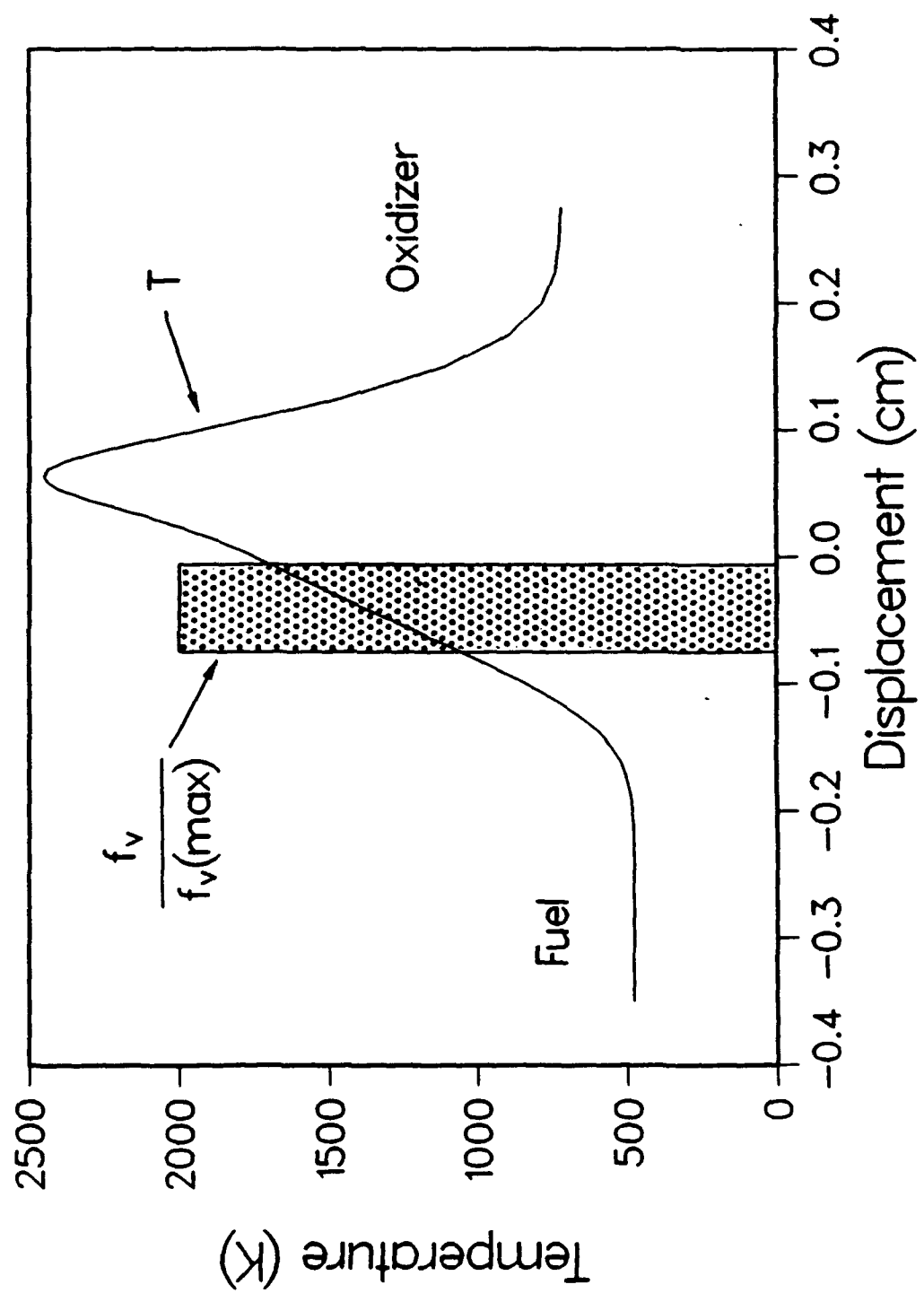
References

1. G. H. Markstein, "Relationship Between Smoke Point and Radiant Emission From Buoyant Turbulent and Laminar Diffusion Flames", in Twentieth Symposium (International) on Combustion, the Combustion Institute, pp. 1055-1061, 1984.
2. L. Orloff, A.T. Modak, and G.H. Markstein, "Radiation from Smoke Layers", Seventeenth Symposium (International) on Combustion, The Combustion Institute, pp. 1029-1038, 1978.
3. R.K. James and D.K. Edwards, "Effect of Molecular Gas Radiation on a Planar, Two-Dimensional, Turbulent-Jet-Diffusion Flame", J. Heat Trans., 99, 221 (1977).
4. D.K Edwards and A. Balakrishnan, "Thermal Radiation by Combustion Gases", Intl. J. Heat Mass Transfer, 16, 25 (1973).
5. A.T. Modak, "Nonluminous Radiation from Hydrocarbon-Air Diffusion Flames", Factory Mutual Research Technical Report 22355-1, 1974.
6. J.D. Felske and C.L. Tien, "Infrared Radiation from Non- Homogeneous Gas Mixtures Having Overlapping Bands", JQSRT, 14, 35 (1974).
7. M.V. Berry and I.C. Percival, "Optics of Fractal Clusters Such as Smoke", Opt. Acta, 33, 577 (1986).
8. R.J. Hall, "Computation of the Radiative Power Loss in a Sooting Diffusion Flame", 27, 809 (1988).
9. R.J. Hall, "The Radiative Source Term for Plane-Parallel Layers of Reacting Combustion Gases", to appear in JQSRT, 1993.
10. M.D. Smooke, I.K. Puri, and K. Seshadri, "A Comparison Between Numerical Calculations and Experimental Measurements of the Structure of a Counterflow Diffusion Flame Burning Diluted Methane in Diluted Air", Twenty- first Symposium (International) on Combustion, the Combustion Institute, pp. 1783-1792 (1986).
11. A. Vranos and R.J. Hall, "Influence of Radiative Loss on Nitric Oxide Formation in Counterflow Diffusion Flames at High Pressure", Comb. & Flame, 93, 230 (1993).
12. R.L. Axelbaum, W.L. Flower, and C.K. Law, Comb. Sci. & Tech., 61, 51 (1988).
13. C. Zhang, A. Atreya, and K. Lee, "Sooting Structure of Methane Counterflow Diffusion Flames with Preheated Reactants and Dilution by Products of Combustion", Twenty-fourth Symposium (International) on Combustion, the Combustion Institute, pp. 1049-1057 (1992).
14. I.M. Kennedy, W. Kollmann, and J.Y. Chen, Comb. & Flame, 81, 73 (1990).
15. P. Glarborg, J.P. Miller, and R.J. Kee, Comb. & Flame, 65, 177 (1986).

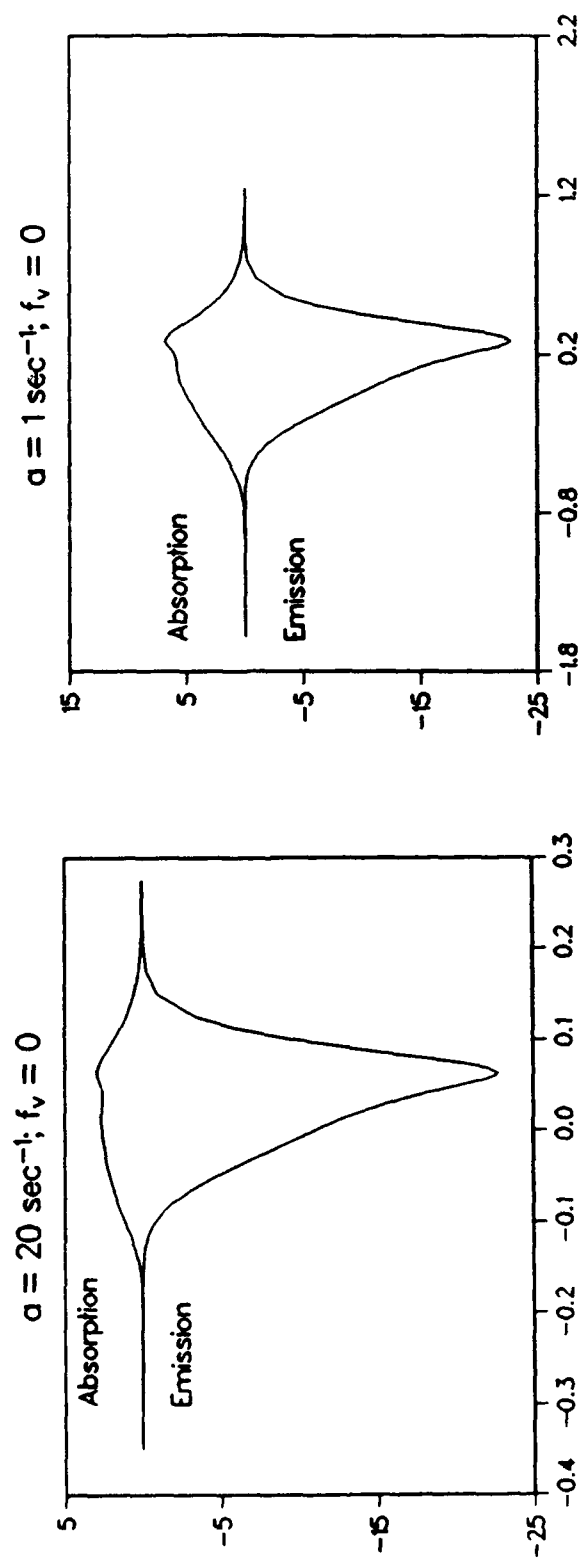
16. M. Geller, "Tables of Integrals Involving Powers, Exponentials, Logarithms, and the Exponential Integral", Cal. Tech. Jet Propulsion Lab. Report, 32-469 (1963).
17. M. Abramowitz & I. Stegun (eds.), "Handbook of Mathematical Functions", Chap. 6, Dover Publications, New York, 9th printing (1970).

Partially funded by AFOSR Contract F49620-91-C-0056



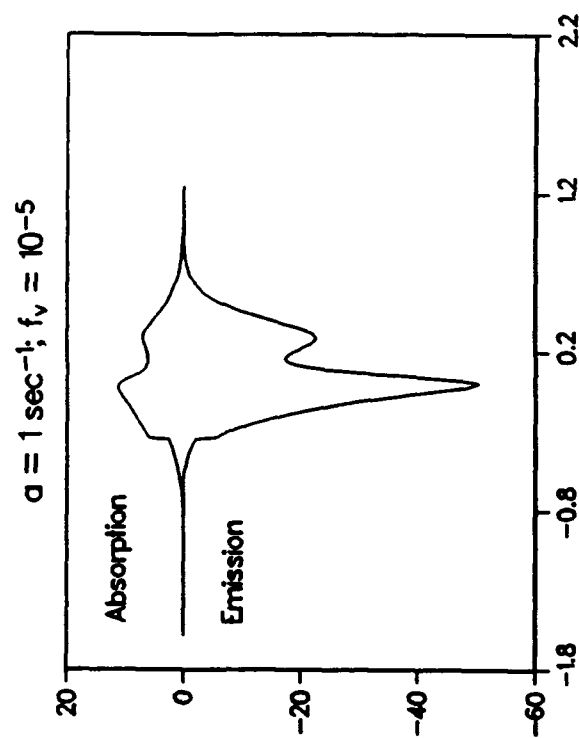
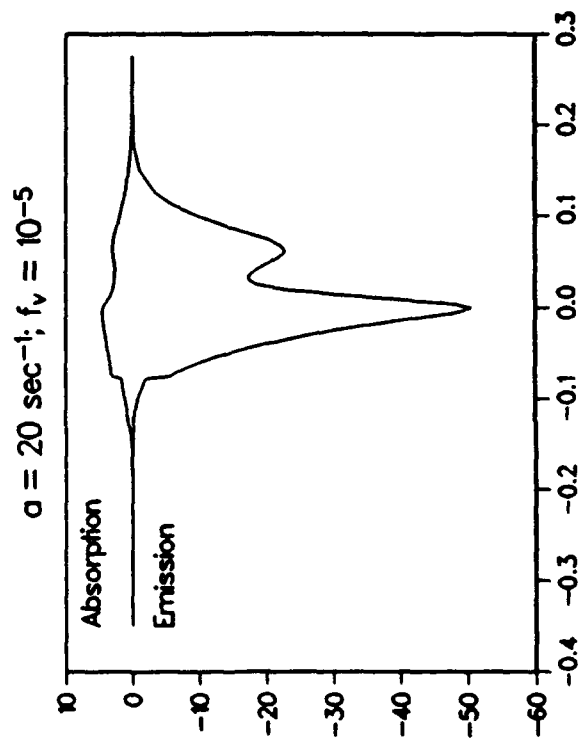


Radiative source term - w/cc

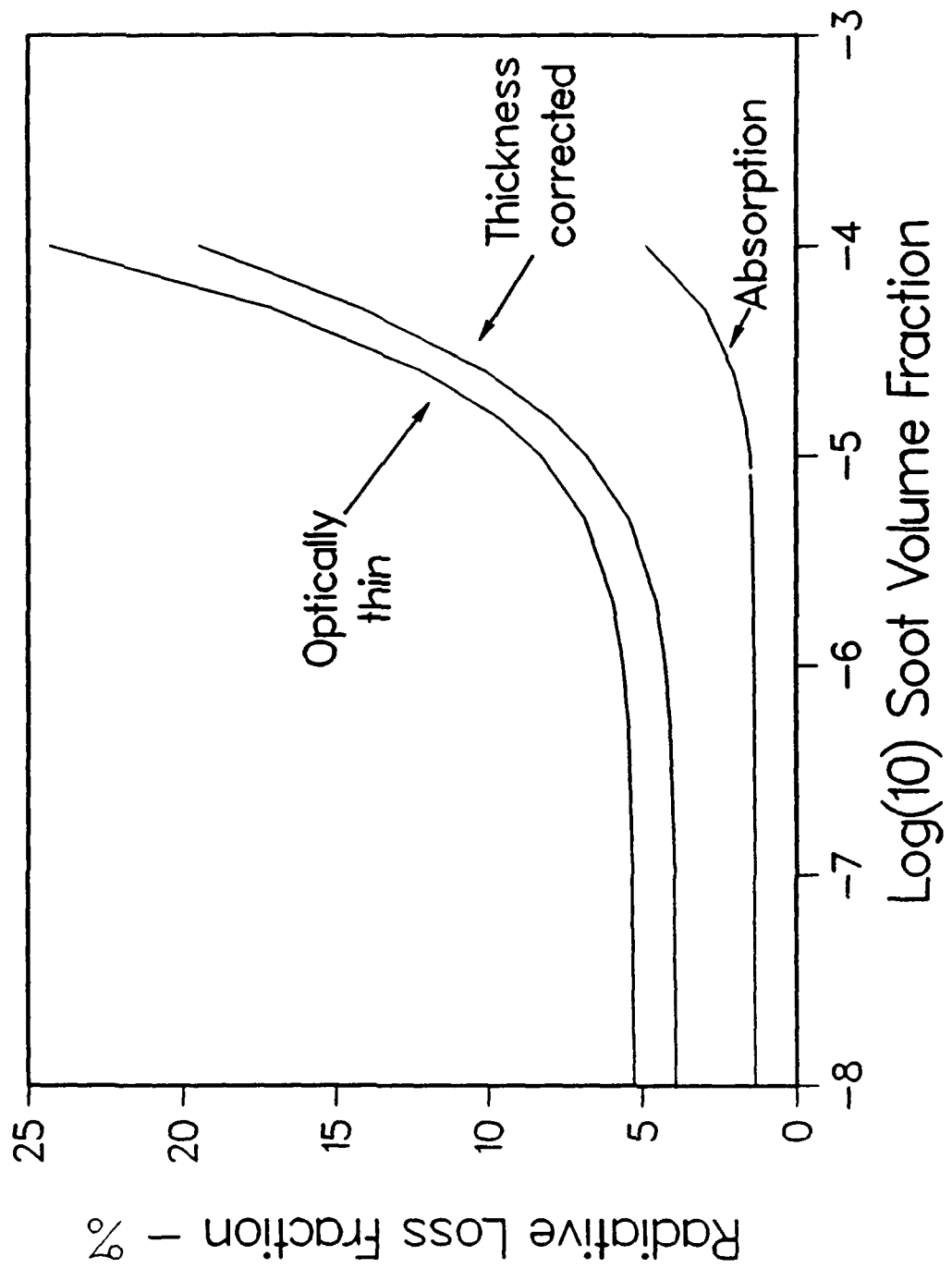


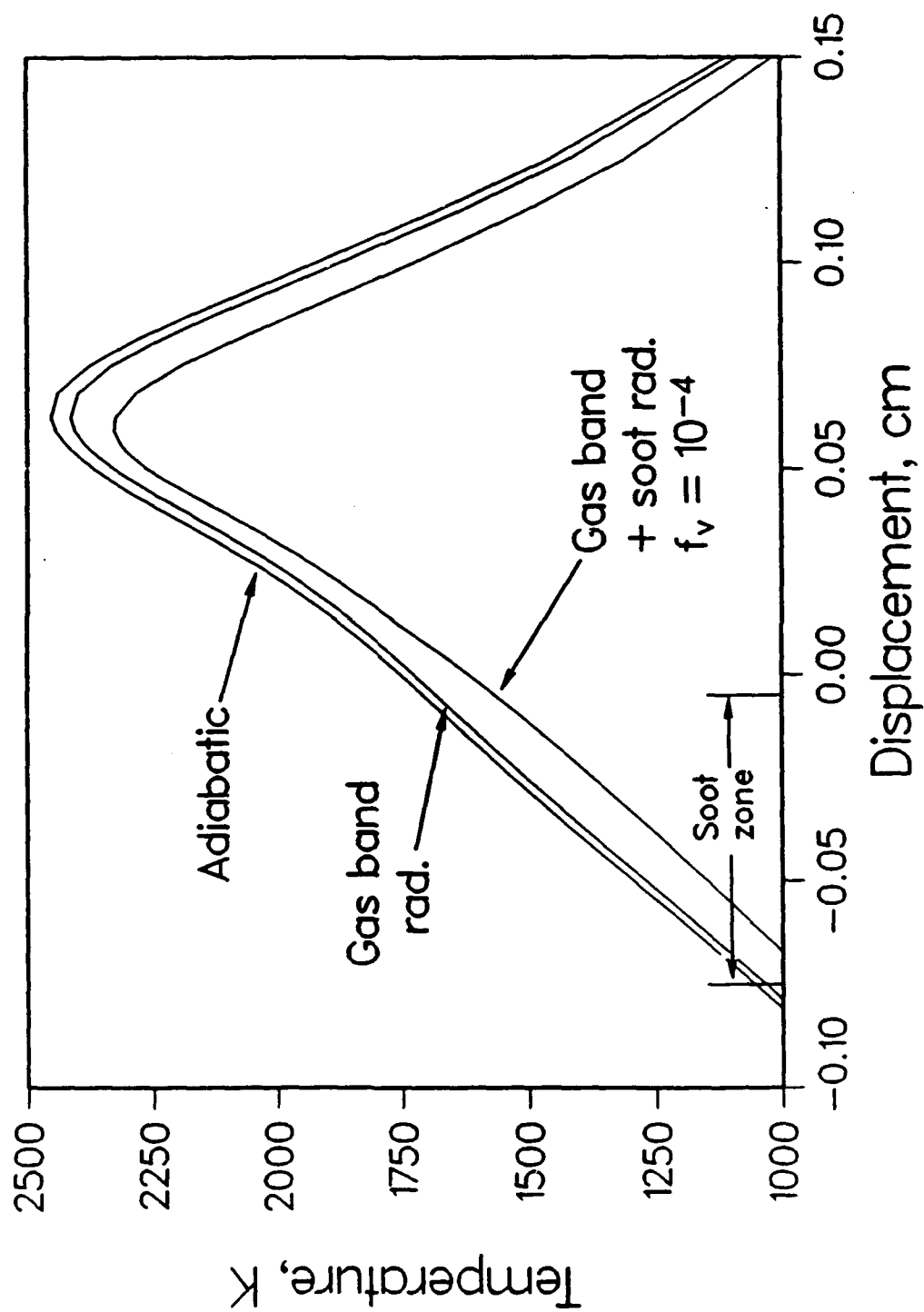
Displacement - cm

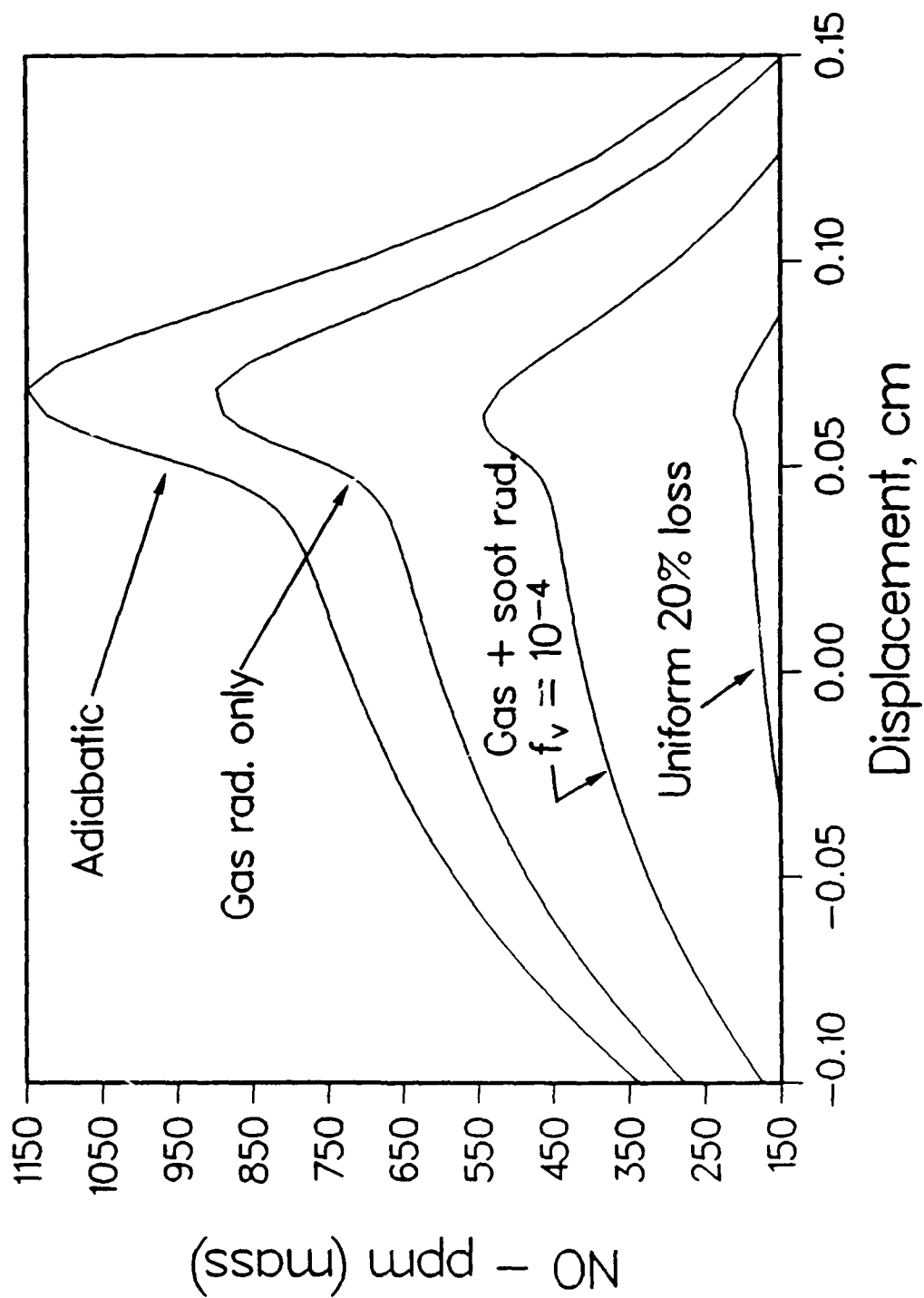
Radiative source term - w/cc



Displacement - cm







Appendix F

**Predictions of Soot Particle Growth
Based on Aerosol Dynamics Modeling**

PREDICTIONS OF SOOT PARTICLE GROWTH BASED ON AEROSOL DYNAMICS MODELLING

R.J. HALL and M.B. COLKET

United Technologies Research Center
East Hartford, CT USA

ABSTRACT

An analytical model of soot formation in laminar, premixed flames is presented which is based on coupling the output of flame chemical kinetics simulations with a sectional aerosol dynamics algorithm for spheroid growth. A simplified particle inception model is employed in which benzene plays an important role. Surface growth has been based on experimental measurements and ab initio calculations using various possible mechanisms for the surface chemistry. Detailed comparisons have been made with various flame data by using experimental temperature profiles and calculating profiles of species concentrations needed for the inception rate and surface growth/oxidation calculations.

MODELLING

Soot growth rates were calculated using a variety of procedures. Common to all mechanisms is the assumption that soot mass growth occurs primarily due to acetylene addition. As an example, a modification of the Frenklach and Wang (1990) mechanism was attempted in which reversibility in the acetylene addition was included to better explain high temperature growth data.

Table 1: Proposed Surface Growth Mechanism

	Reactions Considered	$\log_{10}(A_f)$	E_f	$\log_{10}(A_r)$	E_r
1.	$H + C(s) \rightleftharpoons \dot{C}(s) + H_2$	14.40	12	11.6	7.0
2.	$H + \dot{C}(s) \rightleftharpoons C(s)$	14.34	-	17.3	109.
3.	$\dot{C}(s) \rightarrow \text{products} + C_2H_2$	14.48	62	-	-
4.	$C_2H_2 + C(s) \rightleftharpoons C(s)CHCH$	12.30	4	13.7	38
5.	$C(s)CHCH \rightarrow C'(s) + H$	10.70	-	-	-

The resulting mechanism includes possible acetylene elimination from the soot radical (analogous to phenyl radical decomposition) and separates the acetylene addition process into a reversible formation of the radical adduct and a cyclization reaction. Assuming steady-state conditions for all intermediate species, the rate expression for soot mass growth is calculated to be

$$\frac{dm}{dt} = 2m_c \frac{(k_1[H] + k_{-2}[C_2H_2])k_4k_5\chi A}{(k_{-1}[H_2] + k_2[H] + k_3)k_{-4}k_5 + k_4k_5[C_2H_2]} = G'A = Gm^{2/3} \quad (1)$$

where the Arrhenius factors and activation energies for rate constants are listed in Table 1. In Equation 1, m_c is the mass of a carbon atom, χ is a surface density of $C_{\text{soot}}-H$ sites ($\approx 2.3 \times 10^{15} \text{ cm}^{-2}$ (Frenklach and Wang, 1990)), and A is the particle surface area. The rate of soot particle mass growth will be proportional to particle surface area because typical flame conditions correspond to the free-molecule regime.

Prediction of surface growth requires the local temperature and concentrations of species such as C_2H_2 , H-atoms, and the oxidants O_2 and OH. These, together with the important benzene concentration, were obtained from numerical simulations of the flames (Harris and Weiner, 1983; and Bockhorn, et al, 1983) for which soot data are available. A comparison of the specific surface growth rate predicted by Equation 1 with experimental data is shown in Figure 1.

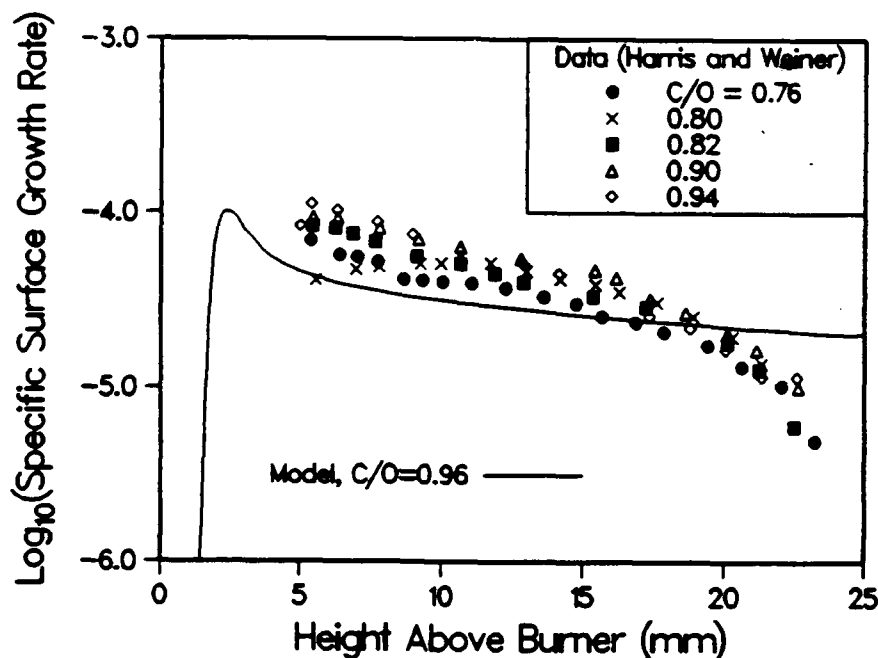


Fig. 1. Comparison of specific surface growth rate predicted from Table 1 mechanism with experimental data

It is assumed that small mass- or pre-inception spheroids grow from benzene through surface growth using the previously discussed particle growth models, with the same gas phase rate coefficients used in the derivation of the particle growth rates, G . In the free-molecule regime, the number density distribution function $n(m, t)$ for these spheroids will be given by the classical growth law

$$\frac{\partial n}{\partial t} + \frac{\partial}{\partial m}(G(t)m^{2/3}n) = \dot{n}(m, t) \quad (2)$$

where the r.h.s. is the rate of gas phase or chemical production. The solution to Equation 2 is readily obtained using the method of characteristics. At a mass threshold m_{inc} , these pre-inception spheroids are allowed to dimerize/coalesce. The inception rate is not a well-defined concept, but it can be considered to correspond to the particle current at this threshold mass, e.g.

$$S_i(t) = \left[m \cdot \frac{dm}{dt} \cdot n(m, t) \right]_{m=m_{inc}} \quad (3)$$

on a mass basis. If the chemical production term on the r.h.s. of Equation 2 is taken to be that of benzene and if it and the surface growth rate do not vary too rapidly with time, the solution to Equations 2 and 3 can be shown to be

$$S_i(t) \simeq \left(\frac{m_{inc}}{m_{benz}} \right) \frac{G(\tau)}{G(\tau')} S_{benz}(\tau') \quad \text{where } \tau = \int_0^t G(t') dt' \quad (4)$$

$$\tau' = \tau - 3(m_{inc}^{1/3} - m_{benz}^{1/3})$$

and m_{benz} and S_{benz} are the benzene molecule mass and mass source rate, respectively. The inception mass threshold is not currently known, and is treated as a parameter in these calculations. There is considerable sensitivity of the predictions to the value chosen because it influences the effect of coalescence on surface area, and thus the rate of suspended mass growth.

The growth of soot spheroids has been modeled as an aerosol dynamics problem, involving the division of the size range of interest (approximately 1 to 100 nm) into discrete intervals or classes, and then solving a master equation for the size class mass densities with terms representing inception, surface growth (or oxidation), and coagulation (coalescence). Because the flames simulated correspond to free-molecule surface growth and coalescence, the calculation of the sectional coefficients is much simplified. The dynamical equations for the sectional mass densities Q_ℓ are (Gelbard and Seinfeld, 1980; Gelbard, 1982)

$$\begin{aligned} \frac{dQ_\ell}{dt} = & \frac{1}{2} \sum_{i=1}^{\ell-1} \sum_{j=1}^{\ell-1} {}^1\bar{\beta}_{i,j,\ell} Q_i Q_j - Q_\ell \sum_{i=1}^{\ell-1} {}^2\bar{\beta}_{i,\ell} Q_i \\ & - \frac{1}{2} {}^3\bar{\beta}_{\ell,\ell} Q_\ell^2 - Q_\ell \sum_{i=\ell+1}^M {}^4\bar{\beta}_{i,\ell} Q_i \quad \begin{array}{ll} \ell_N = -1 & G(t) > 0 \\ = +1 & G(t) < 0 \end{array} \quad (5) \\ & + {}^1G_\ell Q_\ell - \frac{1}{\rho} \frac{d\rho}{dt} Q_\ell \\ & + {}^2G_{\ell+\ell_N} Q_{\ell+\ell_N} - {}^2G_\ell Q_\ell + \delta_{\ell 1} S_1(t) \end{aligned}$$

where the $\bar{\beta}$ represent sectional coagulation coefficients, ${}^1G_\ell$ are intra-sectional growth coefficients, and ${}^2G_\ell$ are inter-sectional growth coefficients. Implicit is the assumption of complete particle coalescence after collision, with no aggregate or chain formation. With the general functional form for the surface growth, Equation 1, the surface growth coefficients can be calculated analytically as

$${}^1G_\ell = 3(\ell \ln(m_\ell/m_{\ell-1}))^{-1} G(t) \left(\frac{1}{m_{\ell-1}^{1/3}} - \frac{1}{m_\ell^{1/3}} \right) \quad {}^2G_\ell = {}^1G_\ell \frac{\bar{m}_{\ell-\ell_N}}{\bar{m}_{\ell-\ell_N} - \bar{m}_\ell} \quad (6)$$

where the m_ℓ are sectional mass boundaries, and the \bar{m}_ℓ represent the average intra-sectional masses. Similarly, the coalescence coefficients need to be calculated only once to obtain the mass-dependencies, and then can be scaled as $\sqrt{T(t)}$.

With the solution for the Q_ℓ , a number of aerosol properties can be evaluated. The soot volume fraction, for example, will be given by $f_v = \frac{1}{\rho_s} \sum_\ell Q_\ell$ where ρ_s is the soot specific density, assumed to be that of solid carbon, 1.8 g/cc. The MAEROS formalism has an extraordinary ability to predict volume fraction (total soot mass) with a relatively small number of size classes. Usually 3-5 are enough to provide a converged solution, but useful results can sometimes be obtained with as few as two!

COMPARISONS TO EXPERIMENTAL DATA

To compare theory with the soot growth data (Harris and Weiner, 1983; and Bockhorn, et al, 1983), profiles of temperature, benzene and acetylene concentrations, and net surface growth rate are provided to the aerosol code as a function of time or height above the burner surface. The net surface growth rate consists of the mass addition rate for acetylene vapor deposition, minus oxidative terms due to oxygen molecules and OH radicals. The latter typically are dominant low in the flame.

For comparison with the Harris flames, CHEMKIN simulations (Kee, et al, 1985) were carried out for C/O ratios of 0.8, 0.92, and 0.96 since temperature profiles were available for these flames. Experimental volume fraction data were available at values of 0.8, 0.84, 0.90, and 0.94. The comparison of the Table 1 growth model with the data is shown in Figure 2. It can be seen that the stoichiometric dependence of the soot volume fraction is approximately satisfied. The model calculations tend to suffer from overshoot at early times, particularly in the C/O=0.8 case, probably because the inception rate resulting from the simplified model is too high.

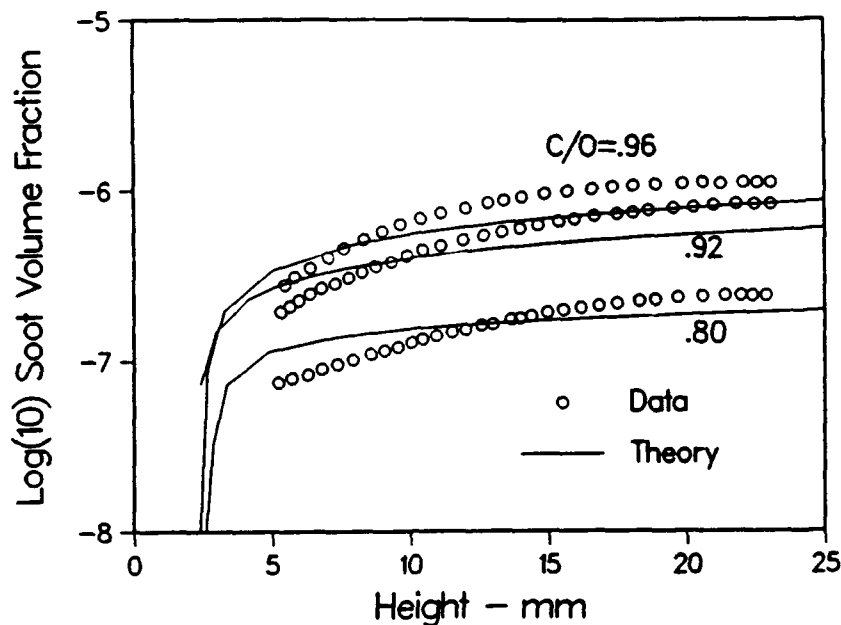


Fig. 2. Comparison of predicted soot volume fractions based on Table 1 surface growth mechanism with experimental data from Harris and Weiner, 1983.

Comparisons with the high temperature acetylene and propane flames of Bockhorn, et al (1983) are also discussed. It is shown that agreement with the data here is much improved by inclusion of an "ageing" of the $C_{soot} - H$ active sites according to

$$\frac{\chi}{\chi_0} = \exp \left(- \int_0^t k_{age}(T(t')) dt' \right) \quad (7)$$

ACKNOWLEDGEMENTS

This work has been sponsored in part by the Air Force Office of Scientific Research (AFSC), under Contracts No. F49620-88-C-0051 and F49620-85-C-0012.

REFERENCES

- Bockhorn, H., F. Fetting and H.W. Wenz (1983). *Ber. Bunsenges. Phys. Chem.*, **87**, 1067.
- Frenklach, M. and H. Wang (1990). *Twenty-third Symposium (International) on Combustion*, The Combustion Institute, p. 1559.
- Gelbard, F. (1982). *MAEROS User Manual*, NUREG/CR-1391, (SAND80-0822).
- Gelbard, F. and J.H. Seinfeld (1980). *J. Coll. Int. Sci.*, **78**, 485-501.
- Harris, S.J. and A.M. Weiner (1983). *Combust. Sci. Tech.*, **31**, 155-167.
- Kee, R.J., J.F. Gcar, M.D. Smooke, and J.A. Miller (1985). "A Fortran Program for Modeling Steady Laminar One-Dimensional Premixed Flames", Sandia Report, SAND85-8240.

REPORT DOCUMENTATION PAGE			Form Approved OMB No 0704-0188	
<small>Public reporting burden for this collection of information is estimated to average 1 hour per response, including the time for reviewing instructions, searching existing data sources, gathering and maintaining the data needed, and completing and reviewing the collection of information. Send comments regarding this burden estimate or any other aspect of this collection of information, including suggestions for reducing this burden to Washington Headquarters Services, Directorate for Information Operations and Reports, 1215 Jefferson Davis Highway, Suite 1204, Arlington, VA 22202-4302, and to the Office of Management and Budget, Paperwork Reduction Project (0704-0188), Washington, DC 20503.</small>				
1. AGENCY USE ONLY (Leave blank)	2. REPORT DATE 14-July-1993	3. REPORT TYPE AND DATES COVERED Annual Tech. Rpt. 1 Jun 92 - 31 May 93		
4. TITLE AND SUBTITLE Mechanistic Models of Soot Formation		5. FUNDING NUMBERS PE - 61102F PR - 2308 SA - BS C - F49620-91-C-0056		
6. AUTHOR(S) Meredith B. Colket, III, Robert J. Hall and Mitch D. Smooke				
7. PERFORMING ORGANIZATION NAME(S) AND ADDRESS(ES) United Technologies Research Center 411 Silver Lane East Hartford, CT 06108		8. PERFORMING ORGANIZATION REPORT NUMBER UTRC93-28		
9. SPONSORING, MONITORING AGENCY NAME(S) AND ADDRESS(ES) AFOSR/NA 110 Duncan Avenue, Suite B115 Bolling AFB DC 20332-0001		10. SPONSORING/MONITORING AGENCY REPORT NUMBER		
11. SUPPLEMENTARY NOTES				
12a. DISTRIBUTION AVAILABILITY STATEMENT Approved for public release; distribution is unlimited		12b. DISTRIBUTION CODE		
13. ABSTRACT (Maximum 200 words) The overall objectives of this work are to (1) refine and update an existing soot formation model and (2) incorporate this soot model into a code describing a laminar, opposed jet diffusion flame. To help advance the understanding of chemical limitations of PAH formation in the soot model, phenylacetylene has been pyrolyzed in a single-pulse shock tube. The formation of PAH's from aromatic-aromatic reactions have been observed and evidence has been obtained for isomerization (equilibration) among polyaromatic species. Thermodynamics of high molecular weight PAH's have been calculated. Benzene production and radiation phenomena have been modeled and where possible these calculations have been compared to experimental results. A sectional aerosol model has been added to the diffusion flame code as well as related subroutines on soot formation, growth, and oxidation and the debugging of the code is nearly complete. Comparisons of the sectional model and a global soot formation model have been made for premixed flames.				
14. SUBJECT TERMS Soot Formation Modeling, Band Radiation, Phenylacetylene Pyrolysis, Formation Mechanisms and Thermodynamics of Polycyclic Hydrocarbons, Soot Formation in Diffusion Flames			15. NUMBER OF PAGES 74	
16. PRICE CODE				
17. SECURITY CLASSIFICATION OF REPORT Unclassified	18. SECURITY CLASSIFICATION OF THIS PAGE Unclassified	19. SECURITY CLASSIFICATION OF ABSTRACT Unclassified	20. LIMITATION OF ABSTRACT Unlimited	